SELF-SUPPORTED ANODES BASED ON CARBON AND TRANSITION METAL SULFIDES FOR SODIUM-ION BATTERIES

WANG HAISHENG

SCHOOL OF MATERIALS SCIENCE AND ENGINEERING

2020

SELF-SUPPORTED ANODES BASED ON CARBON AND TRANSITION METAL SULFIDES FOR SODIUM-ION BATTERIES

WANG HAISHENG

SCHOOL OF MATERIALS SCIENCE AND ENGINEERING

A thesis submitted to the Nanyang Technological University
in partial fulfilment of the requirement for the degree of
Doctor of Philosophy

2020

Statement of Originality

I hereby certify that the work embodied in this thesis is the result of original research, is free of plagiarised materials, and has not been submitted for a higher degree to any other University or Institution.

[Input Date Here]	[Input Signature Here]
. . . . 2020-08-07	. . . . . Wang Haisheng . . . . .
Date	Wang Haisheng

Supervisor Declaration Statement

I have reviewed the content and presentation style of this thesis and declare it is free of plagiarism and of sufficient grammatical clarity to be examined. To the best of my knowledge, the research and writing are those of the candidate except as acknowledged in the Author Attribution Statement. I confirm that the investigations were conducted in accord with the ethics policies and integrity standards of Nanyang Technological University and that the research data are presented honestly and without prejudice.

[Input Date Here]

. . . . 2020-08-07 . . . .
Date

[Input Supervisor Signature Here]

. . . .
Prof. Shen Ze Xiang

Authorship Attribution Statement

This thesis contains material from 2 papers published in the following peer-reviewed journals in which I am listed as the co-first author and first author.

Chapter 4 is published as X.L. Ye, H.S. Wang, Z.F. Chen, M. Li, T. Wang, C. Wu, J.X. Zhang, and Z.X. Shen. Maximized Pseudo-graphitic Content in Self-supported Hollow Interconnected Carbon Foam Boosting Ultrastable Na-Ion Storage. *Electrochimica Acta*, **2021**, 371, 137776.

The contributions of the co-authors are as follows:

- Prof. Shen Ze Xiang provided the initial project direction and revised the manuscript drafts.
- I and Ye Xinli prepared the manuscript drafts.
- I instructed Ye Xinli to conduct most of the material synthesis, material characterization, coin cell assembly, and electrochemical measurements. I and Ye Xinli also analyzed the data.

Chapter 5 is published as H.S. Wang, J.L. Liu, H.H. Wang, X.Y. Cai, X.L. Ye, L.L. Zhang, Z. Chen, and Z.X. Shen. Cobalt Sulfide Nanoflakes Grown on Graphite Foam for Na-Ion Batteries with Ultrahigh Initial Coulombic Efficiency. *Journal of Materials Chemistry A*, **2020**, 8, 14900-14907. DOI: 10.1039/D0TA04312E.

The contributions of the co-authors are as follows:

- Prof. Shen Ze Xiang provided the initial project direction and revised the manuscript drafts.
- I prepared the manuscript drafts. The manuscript was also revised by Dr. Chen Zhen, and Dr. Liu Jilei.
- I conducted most of the material synthesis, material characterization, coin cell assembly, and electrochemical measurements. I also analyzed the data.
- Dr. Wang Huanhuan and Mr. Ye Xinli assisted in the material synthesis.

- Dr. Cai Xiaoyi assisted in the collection of the transmission electron microscopy (TEM) images.
- Dr. Zhang Lili assisted in the collection of the X-ray photoelectron spectroscopy (XPS) data.

[Input Date Here] [Input Signature Here]

. . . . 2020-08-07 . . . . Wang Haisheng . . . . .

Date Wang Haisheng

Abstract

This thesis aims to develop self-supported anode materials based on hard carbon and cobalt sulfides for sodium-ion batteries (SIBs), which are regarded as promising low-cost alternatives to the prevailing lithium-ion batteries. As hard carbons are considered as the most promising first-generation Na-storage anodes, chapter 4 aims to design Na-storage hard carbon with both long cycling stability and a large reversible capacity. In order to achieve higher energy density and ensure the possibility for assembling full cells, chapter 5 aims to develop Na-storage cobalt sulfides with a high initial Coulombic efficiency (ICE). To move further toward practical applications, chapter 6 aims to design Na-storage cobalt sulfides with enhanced cycling stability, a high reversible capacity, and a high ICE.

In chapter 4, the hollow interconnected carbon foam (HICF) is developed by one-step pyrolysis of a commercial and low-cost melamine sponge. The integration of interconnected network structure and hollow feature can not only enable strong mechanical stability and extra inner space to effectively accommodate the structural deformation from Na^+ insertion/extraction, but also achieve fast sodium-ion and electron transport. As a self-supported anode for SIBs, HICF-1 delivers a large reversible capacity (305.7 mAh g^{-1} at 100 mA g^{-1}) with a high initial Coulombic efficiency of 80.2%, an ultralong cycle life (86.4% capacity retention after 1000 cycles at 1000 mA g^{-1}), as well as superior rate performance (170.1 mAh g^{-1} at 1000 mA g^{-1}). In addition, the excellent Na-storage performance is also contributed by the maximum content (63.24%) of pseudo-graphitic phase (d_{002}-spacing between 0.36 and 0.40 nm) in HICF-1 realized by tuning pyrolysis holding time, because the pseudo-graphitic phase could store more sodium ions and maintain more stable microstructure owing to its appropriate *d*-spacing than highly disordered phase (d_{002}-spacing above 0.40 nm). Furthermore, kinetic analysis based on cyclic voltammetry (CV) and galvanostatic intermittent titration technique (GITT) verifies the adsorption-intercalation mechanism, in which highly disordered carbon phase absorbs Na ions fast in the sloping region and then Na ions intercalate into the pseudo-graphitic phase in the plateau region. This work provides a very promising anode candidate for the future commercialization of low-cost SIBs.

In chapter 5, the CoS_x NF@GF composite has been developed by growing CoS_x (Co_9S_8/CoS) nanoflakes on the highly conductive and flexible substrate of graphite foam (GF) through a one-pot solvothermal route. As a freestanding anode for SIBs, to the best of our knowledge, CoS_x NF@GF in diglyme-based electrolyte achieves the highest ICE of 99.4% among the previously reported cobalt sulfide-based Na-ion anodes. Through a systematic investigation of several factors that can potentially influence the ICE, such a high ICE could be ascribed to the following three aspects, including i) the negligible side reactions between diglyme-based electrolyte and Co_9S_8/CoS, owing to much higher Fermi level of diglyme reduction than anode potential μ_A of Co_9S_8/CoS, blocking transfer of electrons from anode to electrolyte, ii) the highly reversible conversion reaction of Co_9S_8/CoS, and iii) the rather low initial capacity loss of substrate GF. Furthermore, CoS_x NF@GF in diglyme-based electrolyte achieves excellent cycling and rate performance, primarily resulting from alleviated volume expansion and facilitated ionic and electronic kinetics ensured by ultrathin nanoflakes vertically aligned with GF, as well as negligible side reactions at the interface of electrode/electrolyte. The revealed underlying rules serve as general guidelines in the development of sodium-ion anodes to achieve superb ICE.

In chapter 6, by taking the structural advantages of both cobalt-based metal organic frameworks (Co-MOFs) and self-supported GF, Co-MOFs nanosheets are first grown on the GF substrate. After the processes of carbonization and sulfurization, carbon nanosheet arrays embedding Co_9S_8 nanoparticles are anchored on GF substrate (Co_9S_8-C NS@GF). The confinement of Co_9S_8 nanoparticles within carbon nanosheet combined with the excellent conductivity and flexibility of GF network could not only effectively alleviate the mechanical stress from conversion reactions to boost cycling stability, but also ensure fast transport of electrons and Na ions to achieve a high reversible capacity. As a self-supported anode for SIBs, the Co_9S_8-C NS@GF exhibits a high reversible capacity of 401 mAh g^{-1} at 0.5 A g^{-1} with a high ICE of 93.2% and a large capacity retention of 85.4% over 300 cycles. Interestingly, the superior Na-storage performance also benefits from the optimization of both the thickness and degree of graphitization of carbon nanosheets tuned by the pyrolysis temperature.

Lay Summary

In recent years, the development of electric vehicles powered by the renewable and green lithium-ion batteries (LIBs) has increasingly grown in popularity to replace the traditional internal combustion engine vehicles, as a result of the depletion of fossil fuels and severe environmental issues. However, the large-scale demand of LIBs will definitely intensify the price of rare lithium resources, which motivates the development of new battery techniques with both low cost and high performance. Sodium-ion batteries (SIBs) as a novel energy storage system are attracting more and more attentions and regarded as a very promising candidate for LIBs, due to much more abundance and lower cost of Na resources in the Earth's crust than those of Li resources, as well as the same working mechanism (the rocking-chair model) of SIBs as that of LIBs. However, it is still challenging nowadays to discover desirable electrode materials for Na-ion storage.

Hard carbons are considered as the most promising commercialized Na-storage anodes, owing to the suitable reversible capacity (150-350 mAh g^{-1}), low potential plateau (~0 V vs. Na^+/Na), inexpensiveness, and high abundance. However, it is still a great challenge to design hard carbon anodes with both long cycling stability and a large reversible capacity. To address this challenge, the hollow interconnected carbon foam (HICF) is developed by one-step pyrolysis of a commercial and low-cost melamine sponge in chapter 4. Owing to the integration of interconnected network structure and hollow feature, HICF delivers a high reversible capacity of 305.7 mAh g^{-1} at a current density of 100 mA g^{-1} and an ultralong cycle life with 86.4% capacity retention over 1000 cycles at 1000 mA g^{-1}. This work provides a very promising anode candidate for the future commercialization of low-cost SIBs.

In order to achieve higher energy density of SIBs, cobalt sulfides have drawn increasing attention owing to their higher specific capacities than those of hard carbon. Nevertheless, most of previously reported cobalt sulfide-based anode materials suffered from low initial Coulombic efficiency (ICE). When assembling full cells, the sufficiently high ICE of anode materials is essential for obtaining superior cell performance, because higher ICE can ensure less irreversible loss of Na ions from the cathodes and result in higher reversible capacities in full cells. Chapter 5 demonstrates a Na-ion anode with an extremely high ICE of 99.4%, based on cobalt sulfide (Co_9S_8/CoS) nanoflakes grown on graphite foam (GF) in diglyme-based electrolyte. Furthermore, the three underlying reasons for such a high ICE have been uncovered, including i) the negligible side reactions between diglyme-based electrolyte and Co_9S_8/CoS, ii) the highly reversible conversion reaction of Co_9S_8/CoS, and iii) the rather low initial capacity loss of substrate GF. The underlying rules revealed in this study serve as general guidelines in the development of sodium-ion anodes to achieve superb ICE.

To move further toward practical applications, chapter 6 aims to design Na-storage cobalt sulfides with enhanced cycling stability, a high reversible capacity, and a high ICE. By integrating the structural advantages of both metal organic frameworks (MOFs) and self-supported GF, carbon nanosheet arrays embedding Co_9S_8 nanoparticles are anchored on GF substrate, which is prepared by carbonization and sulfurization of the precursor of Co-MOFs nanosheets grown on GF. The Na-ion anode exhibits a high reversible capacity of 401 mAh g^{-1} at 0.5 A g^{-1} with a high ICE of 93.2% and a large capacity retention of 85.4% over 300 cycles.

Acknowledgements

First of all, I gratefully acknowledge Ministry of Education (MOE) of Singapore for providing me NTU Research Scholarship during my Ph.D. study, without which this Ph.D. dissertation would not have been possible.

My greatest thanks are conveyed to my supervisor Prof. Shen Ze Xiang for offering me the valuable opportunity to study in his research group and kindly guiding me in scientific research. Prof. Shen have taught me how to think critically, boldly and deeply, how to enjoy discussion and learn quickly from discussions with others, how to solve difficult and important scientific issues, and how to make the research work more valuable and meaningful. Prof. Shen promotes me to become a much better myself now. I think the great transformation of thinking modes is my biggest harvest during the Ph.D. period and will benefit my whole lifetime.

I would like to express my sincere appreciation to my TAC members, Prof. Dong Zhili and Prof. Yan Qingyu, for providing me valuable suggestion on my Ph.D. work during annual TAC meeting. I am also grateful to all MSE administrative and technical staffs, especially Mr. Wang Bochuan, Ms. Serika Cara Navarro, Ms. Serena Tan Siew Koon, Ms. Jacqueline Loh Shuh Hoon, Mr. Phon Kin Sheng, and Ms. Leong Chow Fong, for giving me great support on the graduate study and research.

My gratitude goes to my group members for their kind help with my scientific research and life, including Dr. Chen Zhen, Dr. Wang Huanhuan, Dr. Liu Jilei, Dr. Chao Dongliang, Dr. Lai Linfei, Dr. Cai Xiaoyi, Dr. Yan Jiaxu, Dr. Jiang Liyong, Dr. Xia Juan, Dr. Yin Tingting, Mr. Qian Cheng, Mr. Ye Xinli, Ms. Chen Zhengyan, Mr. Wang Hui, and Ms. Jiang Haifeng.

Last but not the least, I would like to thank my parents Zhang Huizhen and Wang Xianmin sincerely for their love and support.

Table of Contents

Table Captions

Figure Captions

Figure 3.12 Three types of scattering.

Figure 3.13 (a) The evolution of applied potential with time, (b) current response to applied potential in a CV measurement.

Figure 3.14 The profiles of potential versus faradic capacity.

Figure 3.15 (a) The evolution of constant applied current with time, (b) potential response to capacity in a GCD measurement.

Figure 3.16 (a) Cycling stability and (b) rate capability assessed by the GCD technique.

Figure 3.17 (a) The Nyquist plot (in red) and the corresponding equivalent electrical circuit (in blue), (b) the deviation of EIS data.

Figure 4.1 SEM images of (a) melamine sponge precursor (Inset: a photograph of melamine sponge), (b) HICF-1 (Inset: a photograph of HICF-1) and (c, d) the hollow interconnected structures of HICF-1.

Figure 4.2 (a) XRD patterns, (b) fitting results of the (002) diffraction peaks, (c) Raman spectra, (d) Nitrogen adsorption-desorption isothermal curves and (e) the corresponding pore size distributions of the three HICF samples ; (f) HRTEM image of HICF-1.

Figure 4.3 (a) XPS survey spectrum and the corresponding high-resolution XPS analysis of (b) C 1s, (c) O 1s, and (d) N 1s of HICF-1.

Figure 4.4 (a) CV curves of HICF-1 at the scan rate of 0.1 mV s^{-1} between 0.01 and 2.9 V; (b) Galvanostatic charge/discharge profiles of HICF-1 at 100 mA g^{-1}; (c) CV curves of HICF-1 at different scan rates from 0.2 to 2.0 mV s^{-1}; The correlation of current with different scan rates for (d) Peak 1 and (e) Peak 2 of HICF-1; (f) The schematic diagram of sodium-storage mechanism in the HICFs.

diglyme-based electrolyte. (f) Discharge/charge profiles of pure GF in diglyme-based electrolyte at 0.5 A g^{-1}.

Figure 5.6 (a) XRD pattern and (b) SEM image of CoS_x Film@GF. (c) Discharge/charge profiles of CoS_x Film@GF in diglyme-based electrolyte at 0.5 A g^{-1}. (d) Discharge/charge profiles of CoS_x NF@GF in diglyme-based electrolyte at 0.1 A g^{-1} in a potential range of 0.01-2.9V. (e, f) HRTEM images of CoS_x NF@GF electrodes after five cycles in diglyme-based electrolyte.

Figure 5.7 (a) CV curves of CoS_x NF@GF in diglyme-based electrolyte at a scan rate of 0.1 mV s^{-1}. (b) Cycling performance of the three combinations including CoS_x NF@GF in diglyme-based electrolyte, CoS_x Film@GF in diglyme-based electrolyte, and CoS_x NF@GF in EC/DEC-based electrolyte at 0.5 A g^{-1}. (c) Rate performance of the above three combinations at different current densities from 0.2 to 2 A g^{-1}. (d-f) EIS of the above three combinations at fully charged state after different cycles (1st, 50th, 100th).

Figure 5.8 (a) CV curves of pure GF in diglyme-based electrolyte at a scan rate of 0.1 mV s^{-1}. (b) Cycling performance of GF in diglyme-based and EC/DEC-based electrolytes at 0.5 A g^{-1}.

Figure 6.1 (a) SEM image of Co-MOFs NS@GF. (b, c) XRD patterns of Co-C NS@GF carbonized at 870 °C, 800 °C and 900 °C. (d-f) SEM images of Co-C NS@GF carbonized at 800 °C, 870 °C and 900 °C.

Figure 6.2 (a-c) HRTEM images of Co-C NS@GF carbonized at 800 °C, 870 °C and 900 °C. (d) Raman spectra of Co-C NS-800, 870 and 900.

Figure 6.3 (a, b) XRD patterns of Co_9S_8-C NS@GF-870, 800, 900. (c-e) SEM images of Co_9S_8-C NS@GF-800, 870, 900.

Abbreviations

Co-MOFs	Cobalt-based Metal Organic Frameworks
CNTs	Carbon Nanotubes
CV	Cyclic Voltammetry
DEC	Diethyl Carbonate
EC	Ethylene Carbonate
EDS	Energy-Dispersive X-ray Spectroscopy
EIS	Electrochemical Impedance Spectroscopy
FEC	Fluoroethylene Carbonate
GCD	Galvanostatic Charge-Discharge
GF	Graphite Foam
GITT	Galvanostatic Intermittent Titration Technique
HICF	Hollow Interconnected Carbon Foam
HRTEM	High-Resolution Transmission Electron Microscopy
ICE	Initial Coulombic Efficiency
LIBs	Lithium-Ion Batteries
MOFs	Metal Organic Frameworks
PC	Propylene Carbonate
PIBs	Potassium-Ion Batteries
rGO	Reduced Graphene Oxide
SEI	Solid Electrolyte Interphase
SEM	Scanning Electron Microscopy
SIBs	Sodium-Ion Batteries
TEM	Transmission Electron Microscopy
t-GICs	Ternary Graphite Intercalation Compounds
XPS	X-ray Photoelectron Spectroscopy
XRD	X-ray Diffraction

Chapter 1

Introduction

Chapter 1 starts with the problem statement as a rationale for the research, then outlines the corresponding objectives and scope, followed by the dissertation overview and originality.

1.1 Hypothesis/Problem Statement

Lithium-ion batteries (LIBs) as rechargeable electric energy storage devices were firstly commercialized in 1991 by Sony Corporation and nowadays have popularly penetrated into people’s everyday life, especially in the portable electronic market (such as mobile phones, laptops), owing to the high energy density and light weight of LIBs.[1] In recent years, the development of electric vehicles powered by the renewable and green LIBs has increasingly grown in popularity to replace the traditional internal combustion engine vehicles, as a result of the depletion of fossil fuels and severe environmental issues.[2] However, the large-scale demand of LIBs will definitely intensify the price of rare lithium resources, which motivates the development of new battery techniques with both low cost and high performance.[3, 4]

Sodium-ion batteries (SIBs) as a novel energy storage system are attracting more and more attention and regarded as a very promising candidate for LIBs, due to much more abundance and lower cost of Na resources in the Earth's crust, compared to those of Li resources.[5] Moreover, Na element belongs to the same group as Li element in the periodic table and is just located below Li, which endow them many similar chemical properties.[6] As expected, SIBs work in the same mechanism (the rocking-chair model) as LIBs and fortunately the SIBs technique is rapidly blossoming based on the valuable 30-year experiences of LIBs. However, it is still challenging nowadays to discover desirable electrode materials for Na-ion storage.[7, 8]

To address this challenge, various materials have been investigated as sodium-ion anodes, as shown in Figure 1.1,[9] mainly including three types: insertion-type materials (for example, hard carbon, graphite, graphene, and titanium oxides), conversion-type materials (for example, transition metal sulfides and oxides) and alloying-type materials (such as tin and phosphorous).[10] Compared with other anode choices, hard carbons are considered as the most promising commercialized Na-storage anodes, owing to the suitable reversible capacity (150-350 mAh g^{-1}), low potential plateau (~0 V vs. Na^+/Na), inexpensiveness, and high abundance.[11] However, it is still a great challenge to design highly stable hard carbon anodes coupled with a large reversible capacity to effectively alleviate the structural deformation, resulting from repeated intercalation/deintercalation of sodium ions with much larger radius (1.02 Å) than that of lithium ions (0.76 Å).

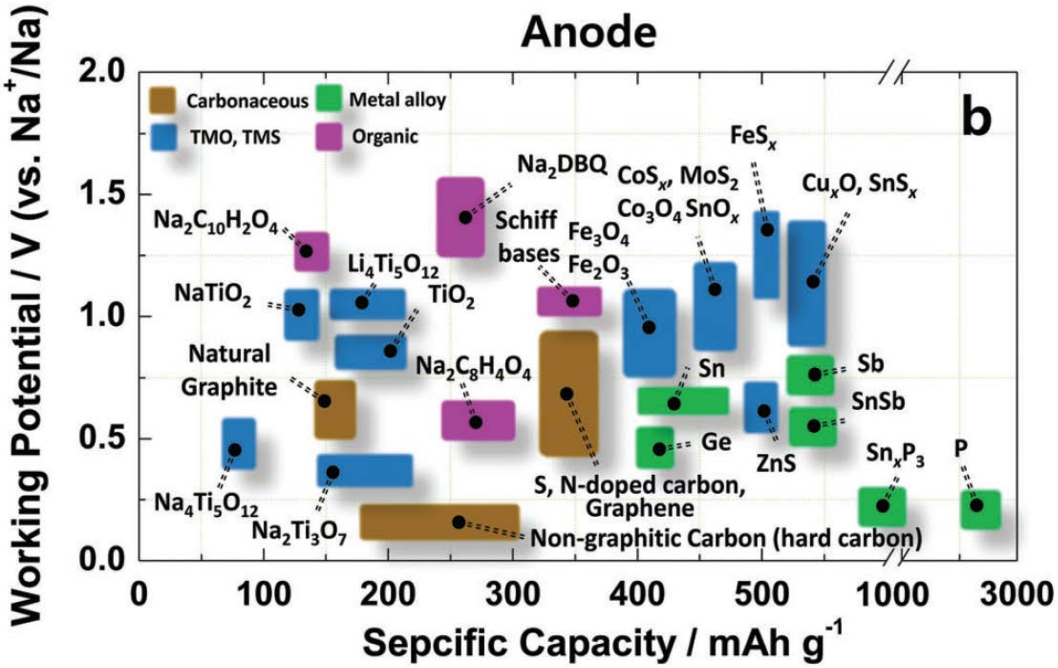

Figure 1.1 Anode materials for SIBs.[9]

In order to achieve higher energy density, the conversion-type materials (for example, transition metal sulfides and oxides) have drawn increasing attention owing to their higher specific capacities than those of insertion-type, and smaller volume changes (200-300%) during electrochemical reactions than those (400-500%) of alloying-type.[12] Compared to transition metal oxides, transition metal sulfides have greater advantage, because metal-sulfur bonds in transition metal sulfides are weaker than corresponding metal-oxygen bonds in transition metal oxides, which is favorable for conversion reaction. Among various transition metal sulfides (such as cobalt sulfides, nickel sulfides, copper sulfides, zinc sulfides, and molybdenum sulfides), cobalt sulfides (i.e., Co_9S_8, CoS, Co_3S_4, and CoS_2) have larger theoretical capacities due to the smaller atomic number of Co and have been widely investigated as Na-ion storage anodes.[13, 14] However, cobalt sulfides usually suffer from poor electrical conductivity, sluggish kinetics and large volume variations during the conversion reaction due to larger Na ions (radius of 1.02 Å) than Li ions (radius of 0.76 Å), restricting the achievement of high capacity and stable cycling.

In addition, due to carbonate-based electrolytes with side reactions between electrolytes and cobalt sulfides, CoS_2 with irreversible conversion reaction, or employed carbon like reduced graphene oxide (rGO), hard carbon with high initial capacity loss, most of previously reported cobalt sulfide-based anode materials also suffered from low initial Coulombic efficiency (ICE), which is less a problem in the case of half cells which usually supply sufficient Na ions from thick metallic Na. However, when assembling full cells, sufficiently high ICE of electrode materials is essential for obtaining high cell performance, because higher ICE can ensure lower irreversible loss of Na ions from the cathodes and lead to higher reversible capacities in full cells. However, until now, no effective strategies have been proposed to settle the issue of low ICE for cobalt sulfide-based electrodes.

1.2 Objectives and Scope

Recently, three-dimensional interpenetrating carbon architectures as self-supported electrodes have attracted great interest in different electrochemical systems.[15, 16] Owing to its structural integrity, the carbon network not only can tolerate the repeated structural deformation induced by electrochemical reactions, but also provide interconnected channels to accelerate ion/electron transport, which should be especially crucial for the large and sluggish Na ions. As the self-supported electrode, the carbon network can directly act as an electrode and avoid the cumbersome slurry-casting electrode fabrication method, which needs polymer binders, conductive additives, solvents, and metal current collectors.

Additionally, hollow structures were demonstrated to greatly boost the cycling stability of conversion-type and alloying-type negative materials with severe volume changes during the electrochemical reactions through providing extra inner cavity to alleviate the induced strains.[17, 18] The hollow structure can also shorten the ionic diffusion distance to achieve a larger reversible capacity, compared with the solid one at the same current rate. Therefore, the advantageous combination of self-supported carbon network with hollow structure is very promising to achieve the hard carbon anodes with both long cycling stability and large reversible capacity for SIBs.

Chapter 4 of this thesis tests the hypothesis that free-standing hollow interconnected carbon foam prepared via one-step pyrolysis of a commercial and low-cost melamine sponge will achieve long cycling stability with a large reversible capacity as anode materials for SIBs.

In recent years, ether-based electrolytes (such as monoglyme, diglyme and tetraglyme) have received great interest in SIBs. Compared with commonly used carbonate-based electrolytes, ether-based electrolytes usually result in better Na-storage performance, owing to the suppressed side reactions between electrolytes and electrodes.[19] In addition, the sulfur-poor Co_9S_8 and CoS phases, as the thermodynamically stable phase, have been demonstrated by ex situ X-ray diffraction (XRD) to exhibit highly reversible conversion reactions.[20] Furthermore, the Na ions in combination with the solvent diglyme can co-intercalate into the graphite layers with low irreversible capacity loss, high capacity retention, and small overpotential upon cycling by forming ternary graphite intercalation compounds (t-GICs), which was first discovered in 2014.[21] Thus, the advantageous combination of Co_9S_8 or CoS phases, graphitic carbon, and diglyme-based electrolyte is very promising to achieve the cobalt sulfide Na-storage anodes with a high ICE.

Chapter 5 of this thesis tests the hypothesis that when freestanding cobalt sulfide (Co_9S_8/CoS) nanoflakes grown on the substrate of graphite foam (GF) are coupled with diglyme-based electrolyte, the Na-storage anode will deliver a high ICE.

One effective strategy to overcome the poor electrical conductivity and large volume variations of cobalt sulfides is to confine nanoscale cobalt sulfides into a carbon matrix. The introduction of nanostructure design into cobalt sulfide can not only shorten the diffusion distance of Na ions to enlarge the capacity, but also effectively tolerate the strains from large volume changes to enhance cycling stability. More importantly, adopting a carbon matrix to encapsulate these nanostructured cobalt sulfides can further increase the conductivity and withstand the mechanical stress from conversion reactions to enhance the capacity and cycling performance. Commonly, organic precursors (such as glucose and polydopamine) are employed to cover the surface of active materials and then carbonized to form carbon coatings. Nevertheless, external organic precursors usually could not ensure uniform coating and strong coupling of carbon with cobalt sulfides. In this regard, cobalt-based metal organic frameworks (Co-MOFs) are an ideal template precursor to construct cobalt sulfide nanoparticles embedded in carbon host, because the uniform distribution of cobalt ions and organic ligands in Co-MOFs could result in cobalt sulfide nanoparticles completely confined into the carbon matrix with strong combination after the processes of carbonization and sulfurization.[13, 14]

On the other hand, constructing nanoarrays of active materials (such as SnS, VO_2, and SnO) on three-dimensional interpenetrating network of GF has been demonstrated as an effective electrode configuration for SIBs to enhance electrical conductivity and endure mechanical stress through structural integrity, high conductivity and excellent flexibility of self-supported GF.[22-24]

Chapter 6 of this thesis tests the hypothesis that by integrating the advantages of Co-MOFs and self-supported GF, carbon nanosheet arrays embedding Co_9S_8 *nanoparticles anchored on GF substrate, which was prepared by carbonization and sulfurization of the precursor of Co-MOFs nanosheets grown on GF, will obtain enhanced cycling stability and a high reversible capacity, when evaluated as anodes for SIBs.*

1.3 Dissertation Overview

Chapter 1 starts with the problem statement as a rationale for the research, then outlines the corresponding objectives and scope, followed by the dissertation overview and originality.

Chapter 2 reviews the development and working principles of sodium-ion batteries, then summarizes different types of cathode and anode materials along with their features and

Na-storage mechanisms. Hard carbon is specifically summarized in terms of its advantages, synthesis method, Na-storage performance and mechanisms. Furthermore, four major strategies to address the issues of Na-storage cobalt sulfides are reviewed.

Chapter 3 describes the detailed information for material synthesis and coin cell assembly. In addition, the basic working principles of material characterization and electrochemical measurements are summarized.

Chapter 4 reports a self-supported hollow interconnected carbon foam prepared by one-step pyrolysis of a commercial and low-cost melamine sponge. The Na-storage anode delivers a large reversible capacity and an ultralong cycle life, which benefits from the integration of interconnected network and hollow feature, as well as maximized content of pseudo-graphitic phase realized by tuning pyrolysis time.

Chapter 5 demonstrates a Na-ion anode with an ultrahigh ICE, based on cobalt sulfide (Co_9S_8/CoS) nanoflakes grown on GF in diglyme-based electrolyte. The achievement of such a high ICE can be ascribed to the following three aspects: i) negligible side reactions between diglyme-based electrolyte and Co_9S_8/CoS, ii) highly reversible conversion reaction of Co_9S_8/CoS, and iii) rather low initial capacity loss of substrate GF.

Chapter 6 presents carbon nanosheet arrays embedding Co_9S_8 nanoparticles anchored on GF. Owing to structural advantages of both MOFs and self-supported GF, the Na-ion anode exhibits excellent cycling stability together with a high reversible capacity. The superior Na-storage performance also benefits from the optimization of thickness and graphitization degree of carbon nanosheets tuned by pyrolysis temperature.

Chapter 7 draws together the threads of this thesis and also provides some strategies for future work.

1.4 Findings and Outcomes/Originality

This dissertation resulted in several novel outcomes by:

1. Achieving an ultralong cycle life with 86.4% capacity retention over 1000 cycles based on self-supported hollow interconnected carbon foam as anodes for SIBs.

2. Uncovering the impact of content of pseudo-graphitic phase on reversible capacity and cycling performance.

3. Demonstrating a Na-ion anode with an extremely high ICE of 99.4%, based on cobalt sulfide (Co_9S_8/CoS) nanoflakes grown on GF in diglyme-based electrolyte.

4. Revealing the root causes for such a high ICE through the following three aspects: i) negligible side reactions between diglyme-based electrolyte and Co_9S_8/CoS, owing to much higher Fermi level of diglyme reduction than anode potential μ_A of Co_9S_8/CoS, which can block electron transfer from anode to electrolyte, ii) highly reversible conversion reaction of Co_9S_8/CoS, and iii) rather low initial capacity loss of GF.

5. Realizing a high reversible capacity of 401 mAh g^{-1} at 0.5 A g^{-1} and a large capacity retention of 85.4% over 300 cycles, based on carbon nanosheet arrays embedding Co_9S_8 nanoparticles anchored on GF as Na-storage anodes.

6. Correlating the Na-storage performance with the thickness and graphitization degree of carbon nanosheets.

References

[1] Z. Chen, G. T. Kim, D. Bresser, T. Diemant, J. Asenbauer, S. Jeong, M. Copley, R. J. Behm, J. Lin, Z. X. Shen, S. Passerini, *Adv. Energy Mater.* **2018**, 8, 1801573.

[2] H. Gao, T. F. Zhou, Y. Zheng, Q. Zhang, Y. Q. Liu, J. Chen, H. K. Liu, Z. P. Guo, *Adv. Funct. Mater.* **2017**, 27, 1702634.

[3] H. L. Pan, Y. S. Hu, L. Q. Chen, *Energy Environ. Sci.* **2013**, 6, 2338-2360.

[4] H. H. Wang, H. S. Wang, S. Chen, B. W. Zhang, G. Yang, P. Gao, J. L. Liu, X. F. Fan, Y. Z. Huang, J. Y. Lin, Z. X. Shen, *ACS Appl. Energ. Mater.* **2019**, 2, 7942-7951.

[5] G. Q. Zou, H. S. Hou, P. Ge, Z. D. Huang, G. G. Zhao, D. L. Yin, X. B. Ji, *Small* **2018**, 14, 1702648.

[6] J. L. Liu, Z. Chen, S. Chen, B. W. Zhang, J. Wang, H. H. Wang, B. B. Tian, M. H. Chen, X. F. Fan, Y. Z. Huang, T. C. Sum, J. Y. Lin, Z. X. Shen, *ACS Nano* **2017**, 11, 6911-6920.

[7] N. Yabuuchi, K. Kubota, M. Dahbi, S. Komaba, *Chem. Rev.* **2014**, 114, 11636-11682.

[8] S. W. Kim, D. H. Seo, X. H. Ma, G. Ceder, K. Kang, *Adv. Energy Mater.* **2012**, 2, 710-721.

[9] J. Y. Hwang, S. T. Myung, Y. K. Sun, *Chem. Soc. Rev.* **2017**, 46, 3529-3614.

[10] K. Chayambuka, G. Mulder, D. L. Danilov, P. H. L. Notten, *Adv. Energy Mater.* **2018**, 8, 1800079.

[11] D. Saurel, B. Orayech, B. W. Xiao, D. Carriazo, X. L. Li, T. Rojo, *Adv. Energy Mater.* **2018**, 8, 1703268.

[12] P. Ge, C. Y. Zhang, H. S. Hou, B. K. Wu, L. Zhou, S. J. Li, T. J. Wu, J. G. Hu, L. Q. Mai, X. B. Ji, *Nano Energy* **2018**, 48, 617-629.

[13] Y. Ma, Y. J. Ma, D. Bresser, Y. C. Ji, D. Geiger, U. Kaiser, C. Streb, A. Varzi, S. Passerini, *ACS Nano* **2018**, 12, 7220-7231.

[14] Z. L. Chen, R. B. Wu, M. Liu, H. Wang, H. B. Xu, Y. H. Guo, Y. Song, F. Fang, X. B. Yu, D. L. Sun, *Adv. Funct. Mater.* **2017**, 27, 1702046.

[15] X. B. Wang, Y. J. Zhang, C. Y. Zhi, X. Wang, D. M. Tang, Y. B. Xu, Q. H. Weng, X. F. Jiang, M. Mitome, D. Golberg, Y. Bando, *Nat. Commun.* **2013**, 4, 2905.

[16] G. Li, J. H. Sun, W. P. Hou, S. D. Jiang, Y. Huang, J. X. Geng, *Nat. Commun.* **2016**, 7, 10601.

[17] R. W. Mo, D. Rooney, K. N. Sun, H. Y. Yang, *Nat. Commun.* **2017**, 8, 13949.

[18] C. F. Dong, J. W. Liang, Y. Y. He, C. C. Li, X. X. Chen, L. J. Guo, F. Tian, Y. T. Qian, L. Q. Xu, *ACS Nano* **2018**, 12, 8277-8287.

[19] J. Zhang, D. W. Wang, W. Lv, L. Qin, S. Z. Niu, S. W. Zhang, T. F. Cao, F. Y. Kang,

Q. H. Yang, *Adv. Energy Mater.* **2018**, 8, 1801361.

[20] Q. B. Guo, Y. F. Ma, T. T. Chen, Q. Y. Xia, M. Yang, H. Xia, Y. Yu, *ACS Nano* **2017**, 11, 12658-12667.

[21] B. Jache, P. Adelhelm, *Angew. Chem.-Int. Edit.* **2014**, 53, 10169-10173.

[22] D. L. Chao, C. R. Zhu, P. H. Yang, X. H. Xia, J. L. Liu, J. Wang, X. F. Fan, S. V. Savilov, J. Y. Lin, H. J. Fan, Z. X. Shen, *Nat. Commun.* **2016**, 7, 12122.

[23] M. H. Chen, D. L. Chao, J. L. Liu, J. X. Yan, B. W. Zhang, Y. Z. Huang, J. Y. Lin, Z. X. Shen, *Adv. Funct. Mater.* **2017**, 27, 1606232.

[24] D. L. Chao, C. R. Zhu, X. H. Xia, J. L. Liu, X. Zhang, J. Wang, P. Liang, J. Y. Lin, H. Zhang, Z. X. Shen, H. J. Fan, *Nano Lett.* **2015**, 15, 565-573.

Chapter 2

Literature Review

Chapter 2 starts with the development and working principles of sodium-ion batteries, then summarizes different types of cathode and anode materials along with their features and Na-storage mechanisms. Hard carbon is specifically summarized in terms of its advantages, synthesis method, Na-storage performance and mechanisms. Furthermore, various strategies to address the issues of Na-storage cobalt sulfides are reviewed, mainly including structure design, carbon modification, electrolyte optimization, and cut-off potential control.

2.1 Sodium-Ion Batteries

A typical configuration of SIBs is illustrated in Figure 2.1.[1] SIBs are constructed with three major components, including positive electrode (cathode), negative electrode (anode), and electrolyte (between cathode and anode). In the charge process, sodium ions are extracted from the positive electrode, then go through the electrolyte, and finally enter the negative electrode inside the battery. At the same time, electrons move from the positive electrode to the negative electrode along the external circuit. Therefore, electrical energy is stored in the form of electrochemical energy within the battery. In the discharge process, the sodium ions and electrons both move in the opposite direction, thus converting the stored electrochemical energy into electrical energy.

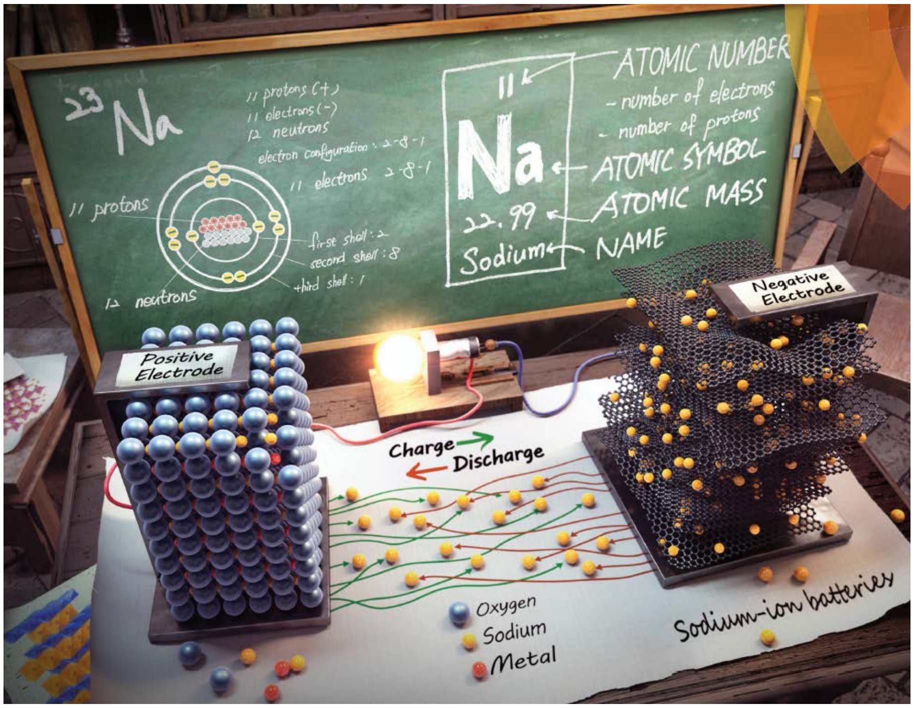

Figure 2.1 Schematic of SIBs.[1]

2.1.1 Cathode Materials

To achieve the high energy density of SIBs, desirable cathode materials should exhibit high working potential and large reversible capacity. Until now, a wide variety of materials have been investigated as cathode materials for SIBs, mainly including four types: layered transition metal oxides (O3 type and P2 type), polyanionic compounds, organic compounds, and Prussian blue analogues, shown in Figure 2.2, along with their working potential and specific capacity.[1] Among them, layered transition metal oxides and polyanionic compounds have received the greatest attention, similar to LIBs.[2] The Na-ion storage mechanism of both types of cathodes is based on intercalation reactions, which are accompanied with minimal structural change and thus ensure high reversibility of electrochemical reactions. In addition, layered transition metal oxides usually deliver larger reversible capacity but lower working potential, compared with polyanionic compounds, displayed in Figure 2.2.

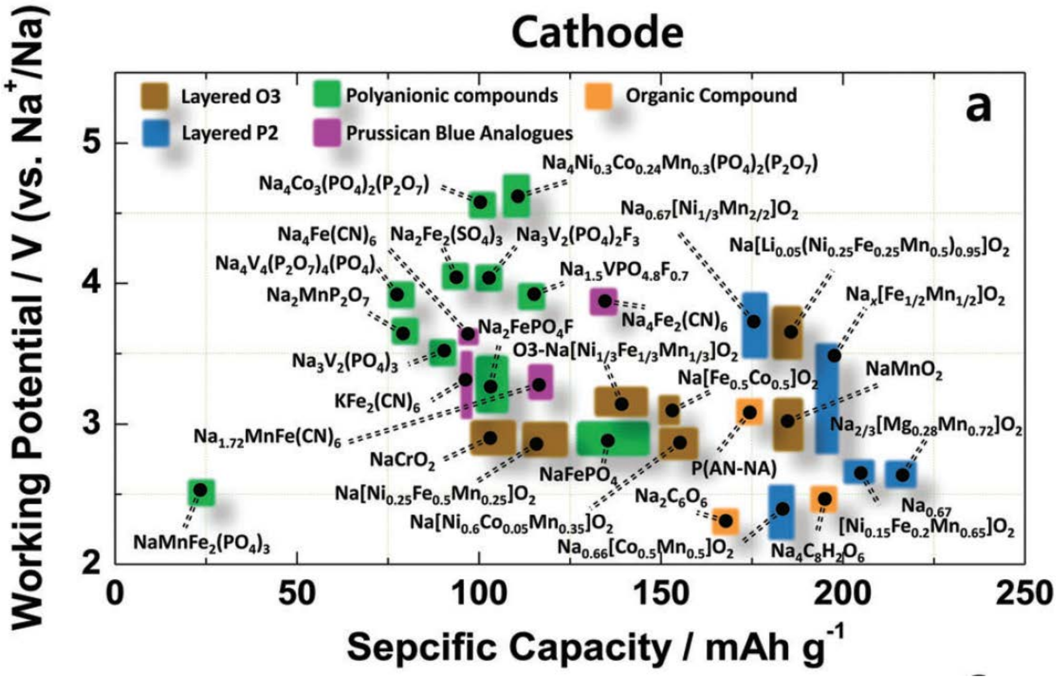

Figure 2.2 Cathode materials for SIBs.[1]

2.1.2 Anode Materials

To achieve the high energy density of SIBs, desirable anode materials should exhibit low working potential and large reversible capacity. According to the Na-ion storage mechanisms, various anode materials can be classified into three major types: intercalation-type anodes, alloying-type anodes, and conversion-type anodes,[3, 4] which is similar to LIBs, illustrated in Figure 2.3.[2, 5] This illustration was designed for LIBs, but also suitable for SIBs.

The intercalation reaction refers to the interlayer insertion of guest ions (Na^+ or Li^+) into the void positions of host matrix.[6-8] During the intercalation/deintercalation process, the structure of host matrix maintains its integrity, accompanied with negligible volume changes, which is favorable for high reversibility of electrochemical reactions. The alloying reaction is that Na ions access the host lattice and then they form alloy through solid solution reaction with no phase changes.[9] During the alloying/dealloying step, the host lattice is usually accompanied with certain structural change and huge volume changes, which can lead to electrode pulverization, loss of electrical contact, and finally poor cycling performance. The conversion reaction is that Na ions access and react with the host matrix to form new compounds, which results in large structural change and volume change.[10]

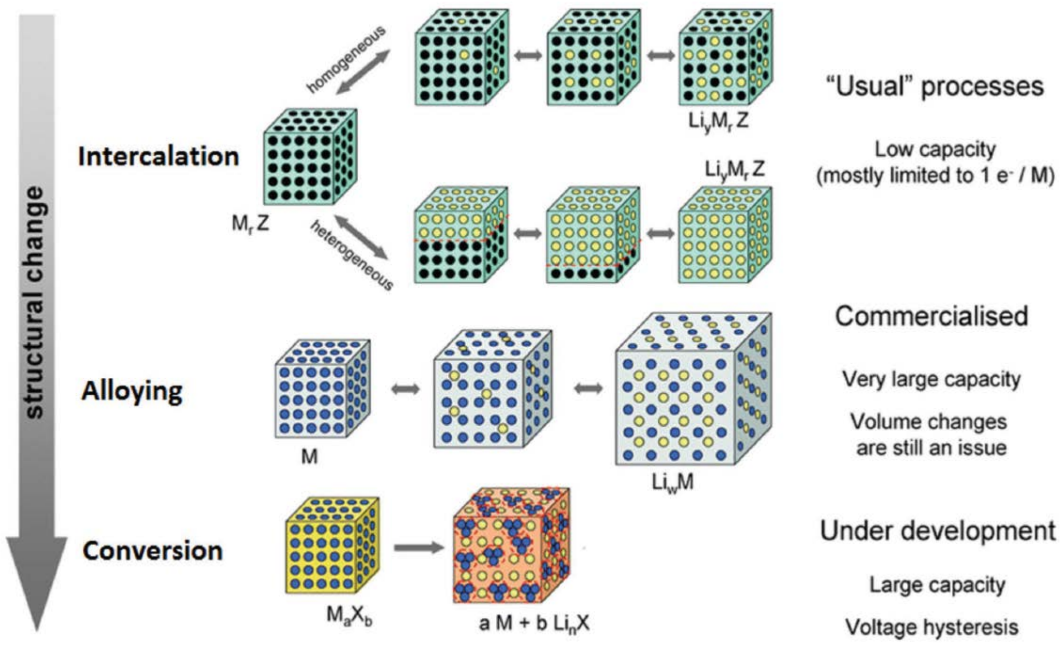

Figure 2.3 Schematic illustration of different Li-ion storage mechanisms of anode materials for LIBs. Void is represented by black circles, metal is represented by blue circles,

and lithium is represented by yellow circles. Similar classifications are adopted in SIBs.[2]

A variety of Na-ion storage anode materials are displayed in Figure 2.4, together with their working potential and specific capacity.[1] The intercalation-type anodes include carbon (for example, graphite, hard carbon, and graphene) and titanium oxides, which deliver relatively low capacity.[11-14] The alloying-type anodes are composed of elements in group 14 (such as Ge and Sn) or group 15 (such as P, Sb, Bi), which commonly show high specific capacity and low operating potential.[15-19] The conversion-type anodes consist of transition metal sulfides, oxides and phosphides, which usually exhibit large theoretical specific capacity, but voltage hysteresis typically occurs in the charge-discharge process, leading to low energy efficiency.[10, 20, 21]

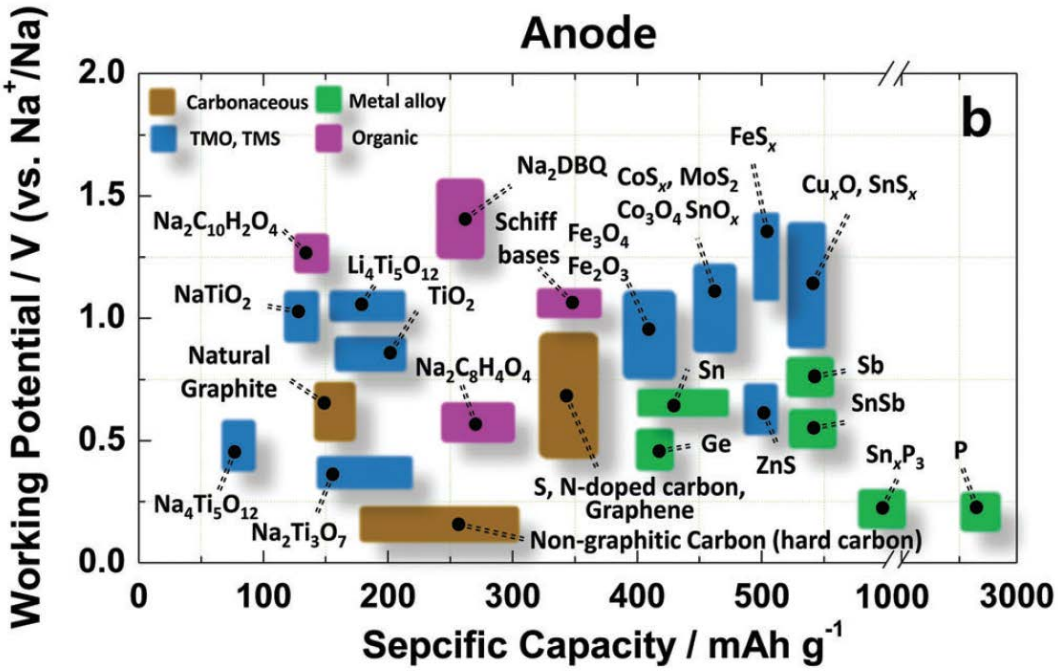

Figure 2.4 Anode materials for SIBs.[1]

2.2 Hard Carbon as Na-Storage Anodes

2.2.1 Hard Carbon versus Graphite, Soft Carbon, and Graphene

sp^2 carbons typically consist of four types: graphite, soft carbon, hard carbon and reduced graphene oxide (rGO). Figure 2.5a, b show the typical X-ray diffraction (XRD) patterns and corresponding structures of the above four sp^2 carbons.[22] Graphite possesses crystalline layered structure, corresponding to the very sharp (002) diffraction peak. From soft carbon to hard carbon, the (002) diffraction peak become broader and moves to the lower diffraction angle, because the carbon structure becomes more disordered, accompanied by larger interlayer distance. As for rGO, single-layered and few-layered structures co-exist. In the discharge-charge profiles of the four sp^2 carbons as anodes for SIBs (Figure 2.5c), the specific capacities of graphite and soft carbon are very low,[23] while hard carbon possesses moderate specific capacity and low operating potential. Although rGO delivers much larger capacity than hard carbon, the high operating potential and obvious voltage hysteresis of rGO limit its application.[24] Therefore, hard carbon has been considered as the most promising first-generation anode for SIBs.[25]

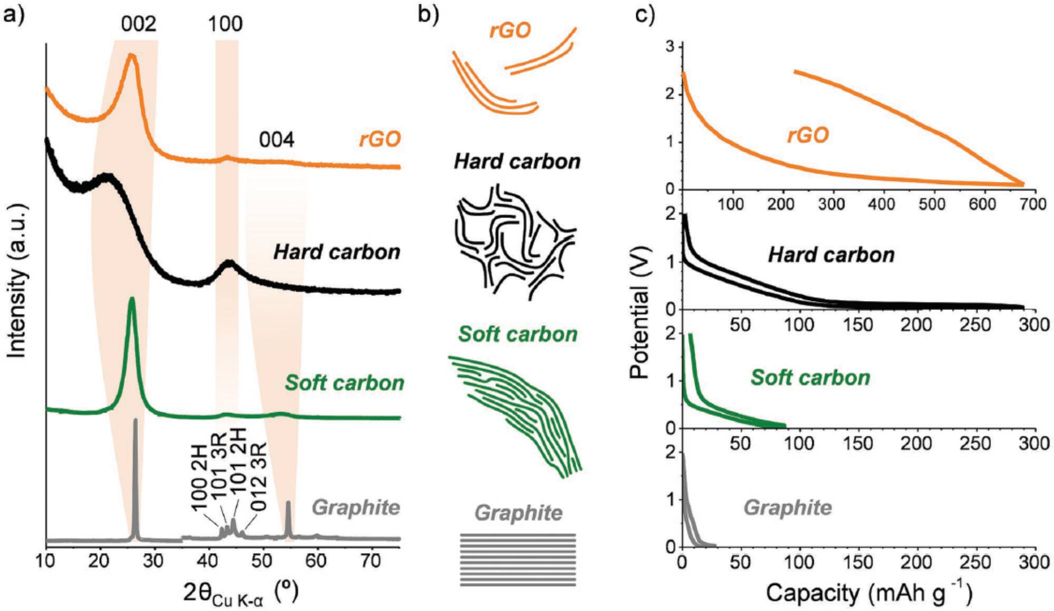

Figure 2.5 (a) XRD patterns, (b) structural graphics, (c) typical discharge-charge profiles in sodium half cell of graphite, soft carbon, hard carbon and rGO.[22]

2.2.2 Synthesis of Hard Carbon

Hard carbon materials are commonly carbonized from various organic precursors under inert atmosphere (such as N_2 or Ar gas) at a high temperature. The typical pyrolysis process is illustrated in Figure 2.6.[22] Large amounts of volatile species originating from hydrogen atoms and heteroatoms escape from the organic precursors between 250 and 500 °C, leading to main mass loss and increasing carbon content. The precursors are considered to be mostly carbonized above 700 °C, but some hydrogen atoms and heteroatoms still exist in the residue. Higher temperature in the range of 1000-1500 °C can further increase the carbon content of the final material. The d_{002} of hard carbon is typically from 3.7 to 4.0 Å. In addition, the structure and microstructure of hard carbon highly depend on precursors and preparation conditions.

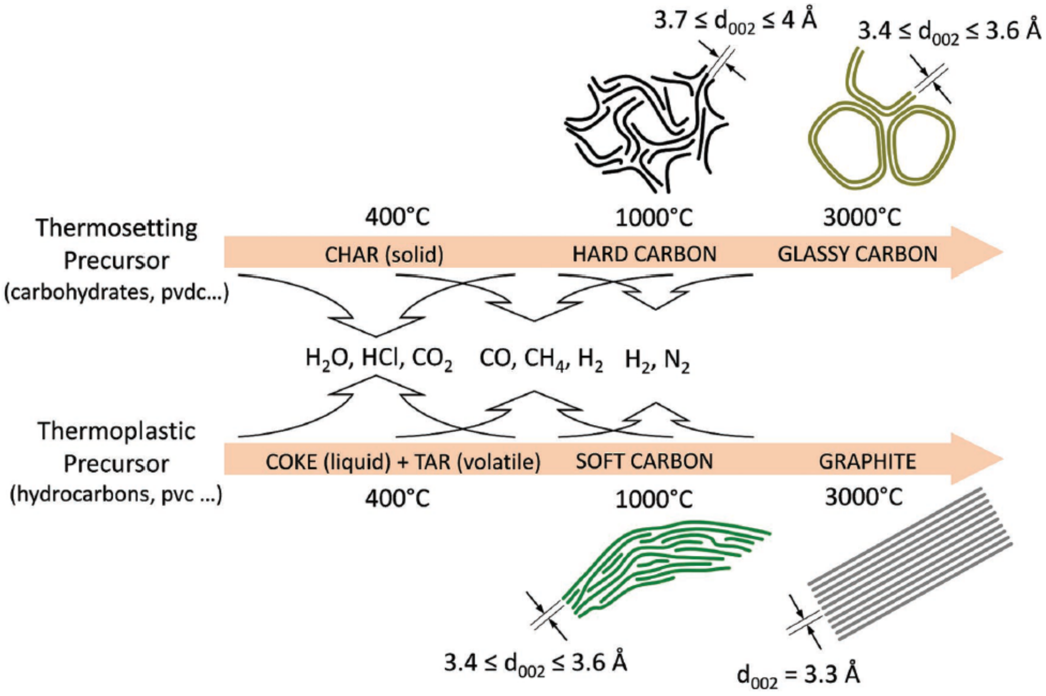

Figure 2.6 Schematic illustration of pyrolysis process of organic precursors.[22]

2.2.3 Na-Storage Performance of Hard Carbon

Owing to the advantages of both the large specific capacity of near 300 mAh g^{-1} and low average working potential of ~0.3 V, hard carbon is regarded as the most competitive carbon anode materials for SIBs versus the commercialized graphite anode in LIBs with the theoretical specific capacity of 372 mAh g^{-1} and working potential below 0.2 V. Until now, hard carbon prepared from a wide variety of organic precursors have been reported for sodium-ion storage. The commonly used organic precursors consist of three types: carbohydrates,[26] raw biomass,[27-29] and polymers.[30-32]

The hard carbon as Na-ion anodes can be traced back to 2000, using carbohydrates as the precursor.[33] Stevens and Dahn investigated the Na storage performance of a hard carbon derived from glucose at 1150 °C, which showed a specific capacity of 280 mAh g^{-1}, but no data of cycling performance. Since the interest for SIBs resurged in 2011, different hard carbons have been widely studied as anode materials for SIBs. In 2013, Ponrouch et al. reported a sucrose-derived hard carbon carbonized at 1100 °C for SIBs, which achieved a high capacity of 326 mAh g^{-1} at 37.2 mA g^{-1} and good cycling performance (more than 300 mAh g^{-1} retained over 120 cycles).[34] However, the initial Coulombic efficiency (ICE) was low (61%).

In 2012, Cao et al. reported a hollow hard carbon originating from polyaniline (a kind of polymer) at 1150 °C for SIBs, which displayed a reversible capacity of 251 mAh g^{-1} at 50 mA g^{-1}, 82.2% capacity retention after 400 cycles, but low ICE of 50.5%.[35] Additionally, peat moss (a kind of raw biomass) was carbonized at 1100 °C and studied as Na-storage anodes by Mitlin et al. in 2013.[36] The hard carbon from peat moss showed a stable capacity of 298 mAh g^{-1} at 50 mA g^{-1} and retained a capacity of 255 mAh g^{-1} after 210 cycles at 100 mA g^{-1}, displayed in Figure 2.7. However, the issue of low ICE (57%) still existed.

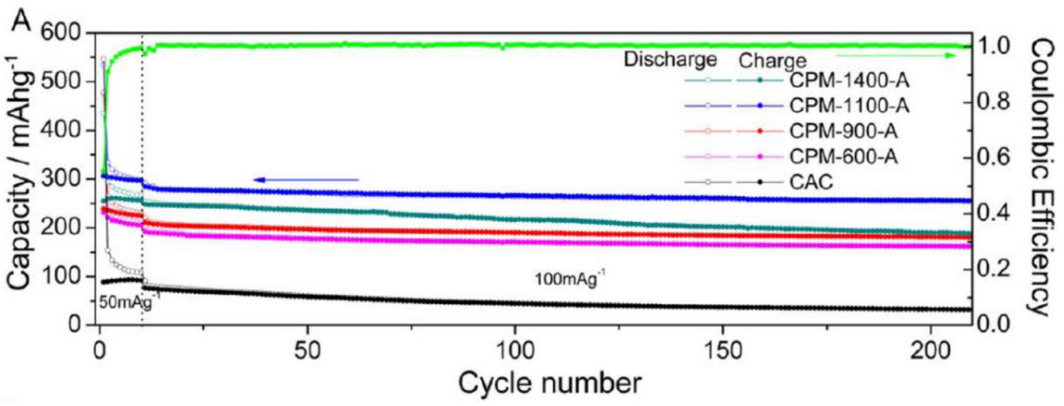

Figure 2.7 The cycling performance of carbonized peat moss (CPM).[36]

2.2.4 Na-Storage Mechanism of Hard Carbon

The "absorption-intercalation" model was first proposed by Cao et al. in 2012 as the Na-ion storage mechanism for hard carbon.[35] As shown in Figure 2.8,[26] the plateau region below 0.1 V results from the intercalation of Na ions between the hard carbon layers, which is similar to Li-ion intercalation between the graphite interlayers. Additionally, the sloping region above 0.1 V originates from Na-ion absorption on the surface of hard carbon.

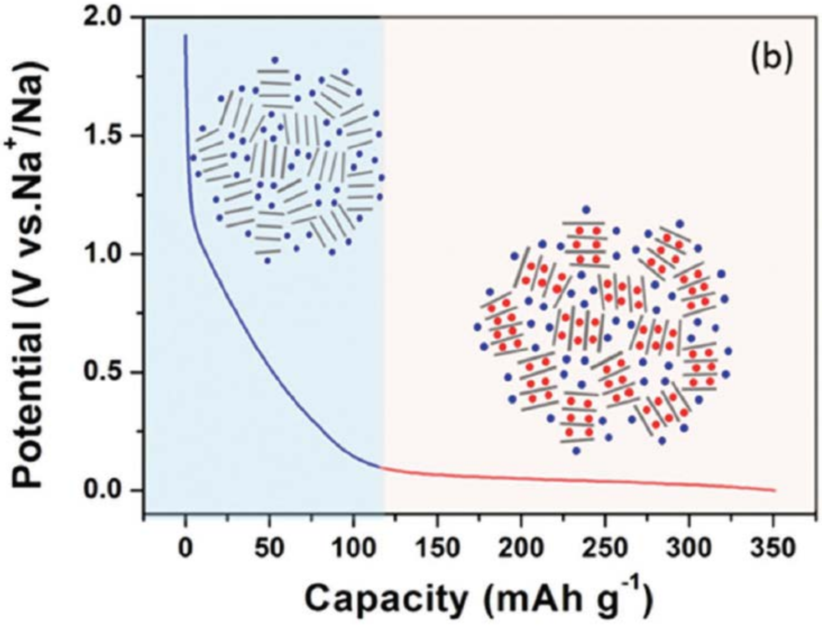

Figure 2.8 Schematic illustration of "absorption-intercalation" mechanism.[26]

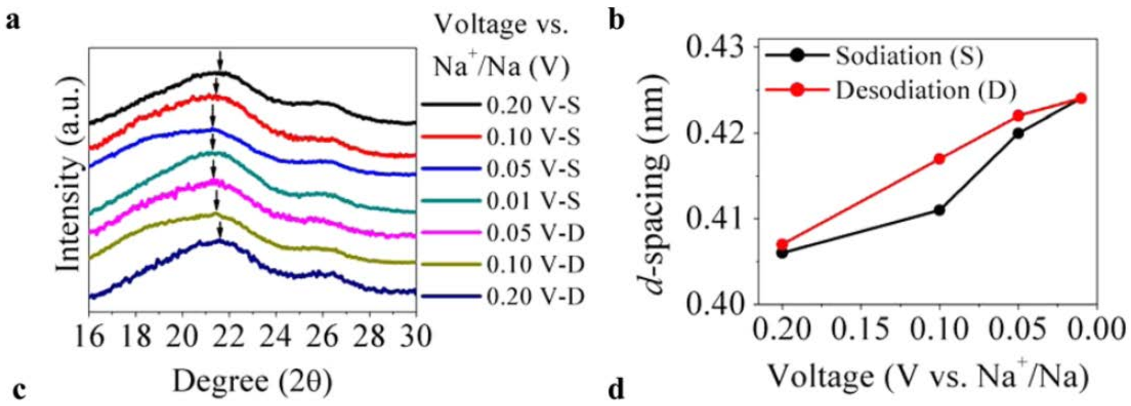

Figure 2.9 (a) ex situ XRD patterns at different states of sodiation and desodiation. (b) The corresponding variation of d_{002} spacing.[37]

This mechanism was supported by Mitlin et al. in 2013, who first observed that the (002) diffraction peak of hard carbon shifted to lower 2θ values in ex situ XRD when the discharge process was from 0.1 to 0.001 V.[36] The increase of d_{002} spacing demonstrated that the plateau capacity should be associated with Na^+ intercalation. In 2015, Ji et al. also observed the reversible dilation-contraction of d_{002} spacing in hard carbon upon discharging-charging in the plateau region by ex situ XRD, shown in Figure 2.9.[37] In addition, the sloping region was identified to depend on the concentration of defects, suggesting that defect absorption of Na ions contribute to the sloping capacity.

2.3 Cobalt Sulfides as Na-Storage Anodes

As a typical conversion-type anode material, cobalt sulfides (Co_9S_8, CoS, Co_3S_4 and CoS_2) have attracted tremendous attention for Na-ion storage, owing to their high theoretical specific capacity.[38-41] However, cobalt sulfides commonly suffer from large volume changes and sluggish kinetics during the conversion reaction due to larger Na ions (radius of 1.02 Å) than Li ions (radius of 0.76 Å), which lead to poor cycling and rate capabilities.[42-45] Until now, various effective strategies have been developed to tackle these issues, mainly including structure design, carbon modification, electrolyte optimization, and cut-off potential control.[46]

2.3.1 Structure Design

Nanostructure and hollow structure are the two main structural design for cobalt sulfide-based anodes for SIBs. The introduction of nanostructure design into cobalt sulfide can not only effectively tolerate the strains from large volume changes to enhance cycling stability, but also shorten the diffusion distance of Na ions to improve the rate performance. Additionally, extra void space can be provided by the hollow structure design to endure large volume changes and therefore boost cycling performance.

Guo et al. employed a sol-gel method to embed cobalt sulfide (Co_9S_8/CoS) quantum dots into N/S-doped carbon nanosheets, denoted as CoS_x@NSC.[10] The ultrafine CoS_x size of 3-5 nm was observed by high-resolution transmission electron microscopy (HRTEM), shown in Figure 2.10. As an anode for SIBs, the CoS_x@NSC nanocomposite exhibited superb rate performance (500 mAh g^{-1} even at a high current of 10 A g^{-1}), which benefits from fast Na-ion diffusion induced by the ultrafine CoS_x size.

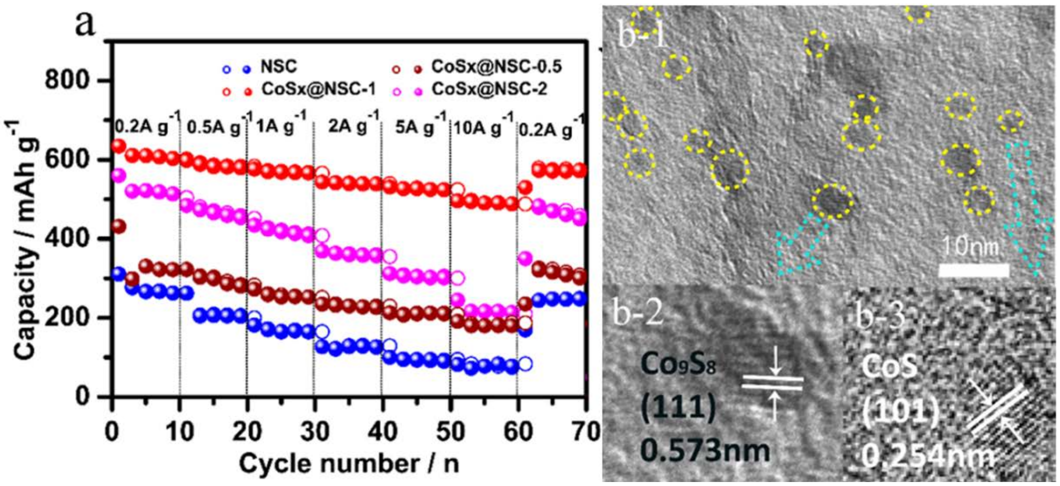

Figure 2.10 The HRTEM images of CoS_x@NSC and the rate performance for SIBs.[10]

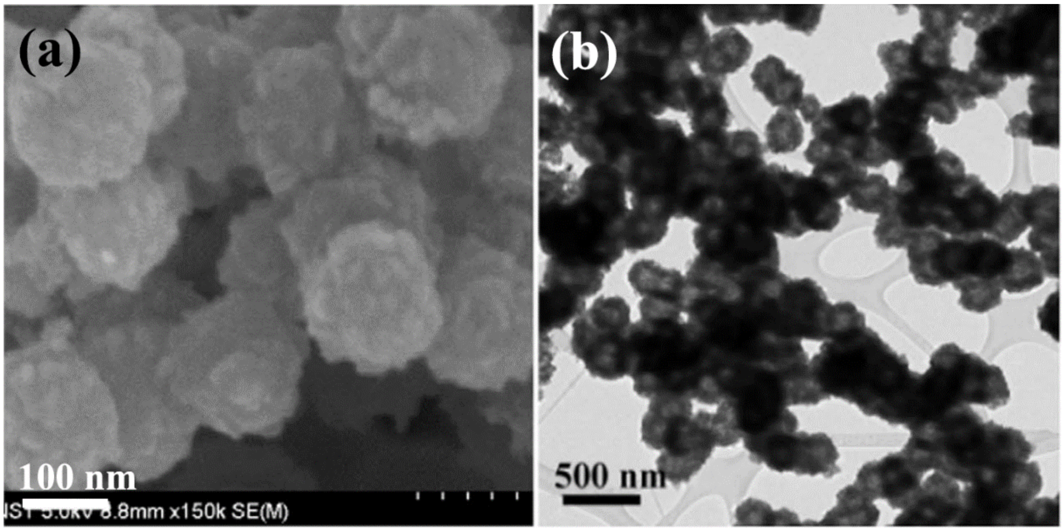

Figure 2.11 **(**a) SEM image and (b) TEM image of the cobalt sulfide hollow nanospheres.[47]

In addition, the hollow sphere structure was adopted by Xiao et al. to design Na-storage cobalt sulfides, composed of three phases of Co_9S_8, CoS, and Co_3S_4.[47] The scanning electron microscopy (SEM) showed the sphere structure with the diameter of 150-200 nm and the transmission electron microscopy (TEM) verified the hollow structure, in Figure 2.11. Owing to additional void space provided by the hollow structure design, the cobalt sulfide anode achieved good cycling stability with 83.1% capacity retention over 100 cycles at 500 mA g^{-1}. However, the anode exhibited a low ICE of 77.2%.

2.3.2 Carbon Modification

A wide variety of carbon materials (such as graphene and hard carbon) are commonly coupled with cobalt sulfide as anodes for SIBs. Owing to their high conductivity, carbon materials can achieve enhanced electrode kinetics by providing fast electron transport. In addition, as the buffer layers, carbon can alleviate the strains induced by large volume expansion.

Du et al. embedded Co_3S_4 nanosheets into graphene layers by a freeze-drying method.[39]

The nanosheet structure of pure Co_3S_4 was shown in SEM and TEM images (Figure 2.12a, b). The SEM image in Figure 2.12c demonstrated that the Co_3S_4 nanosheets were completely covered by wrinkled graphene layers. When evaluated as Na-storage anode, the composite showed good rate capability (237 mAh g^{-1} at 5 A g^{-1}) and 71% capacity retention (329 mAh g^{-1}) over 50 cycles at 0.5 A g^{-1}. The issue of low ICE (53%) still occurred.

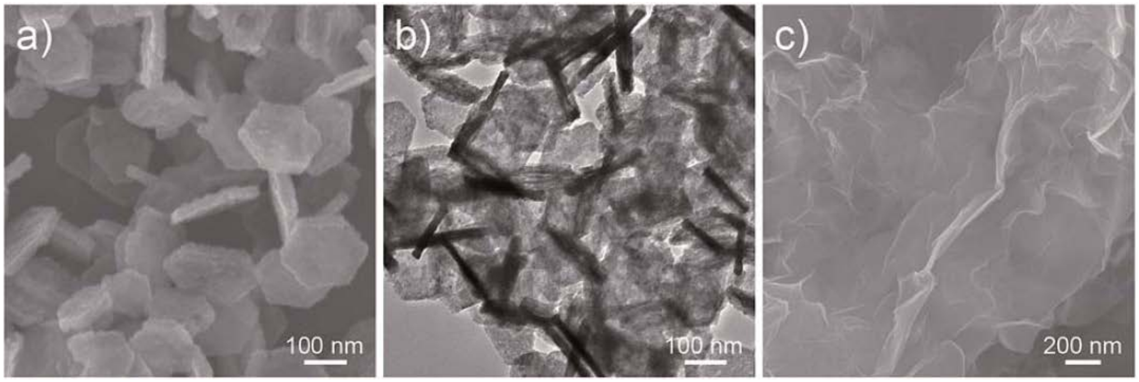

Figure 2.12 (a) SEM image and (b) TEM image of the pure Co_3S_4 nanosheets. (c) SEM image of the Co_3S_4 nanosheets coupled with graphene.[39]

2.3.3 Electrolyte Optimization

As mentioned above, the material design of cobalt sulfides can greatly enhance the electrochemical performance. Besides the material design, electrolytes also play an important role in the Na-storage properties of cobalt sulfides. The commonly used electrolytes are carbonate-based electrolytes, for example, ethylene carbonate (EC), diethyl carbonate (DEC), fluoroethylene carbonate (FEC), and propylene carbonate (PC).[48] In recent years, ether-based electrolytes (such as monoglyme, diglyme and tetraglyme) have received great interest in SIBs.[49] Compared with carbonate-based electrolytes, ether-based electrolytes usually result in better Na-storage performance, owing to the suppressed side reactions between electrolytes and electrodes.[50]

Shadike et al. integrated CoS_2 with carbon nanotubes (CNTs) through a hydrothermal route.[51] The Na-storage properties of the CoS_2-CNTs composite were separately explored in 1 M $NaCF_3SO_3$ in diglyme (ether-based electrolyte) and 1 M $NaClO_4$ in EC/PC (carbonate-based electrolyte). Both the cycling and rate performance in ether-based electrolyte surpassed those in carbonate-based electrolyte, shown in Figure 2.13.

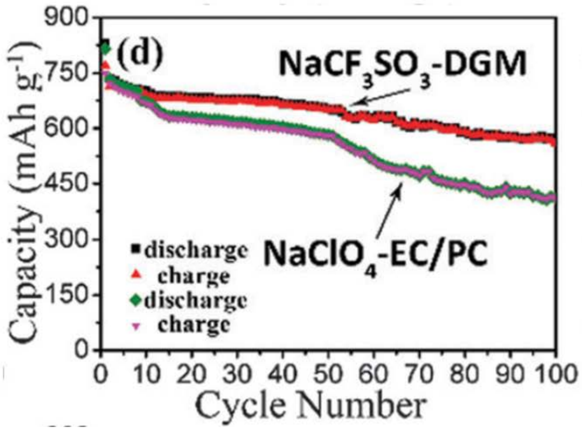

Figure 2.13 The cycling and rate performance of the CoS_2-CNTs composites in ether-based and carbonate-based electrolytes.[51]

2.3.4 Cut-Off Potential Control

In addition to the electrolyte optimization, the control of cut-off potential also has a great impact on the cycling stability of Na-storage cobalt sulfides. A higher terminal potential during the discharge process usually brings about better cycling performance, because the high discharge terminal potential can decrease the extent of conversion reactions and thus suppress the structural damage of electrode materials caused by large volume expansion.

Peng et al. developed a solvothermal method to grow CoS nanoplates on rGO as anodes for SIBs.[52] When the discharge-charge process was conducted between 0.1 and 2.9 V, the CoS/rGO only retained 148 mAh g^{-1} over 500 cycles at 1 A g^{-1}. However, after the discharge terminal potential was lifted to 0.6 V, the superior cycling stability was achieved (88% capacity retention corresponding to 420 mAh g^{-1} even after 1000 cycles), as shown in Figure 2.14.

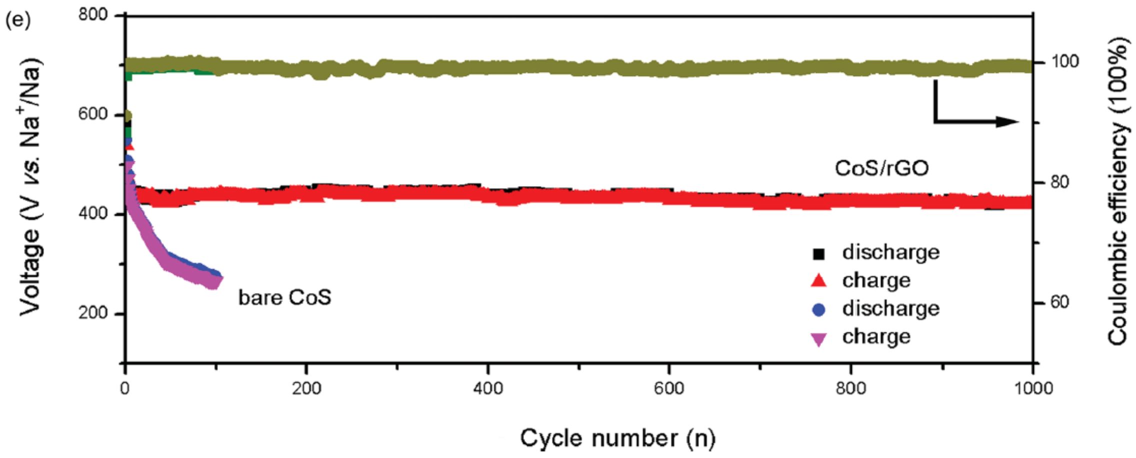

Figure 2.14 Cycling performance of CoS/rGO between 0.6 and 2.9 V at 1 A g^{-1}.[52]

References

[1] J. Y. Hwang, S. T. Myung, Y. K. Sun, *Chem. Soc. Rev.* **2017**, 46, 3529-3614.

[2] K. Chayambuka, G. Mulder, D. L. Danilov, P. H. L. Notten, *Adv. Energy Mater.* **2018**, 8, 1800079.

[3] H. Y. Kang, Y. C. Liu, K. Z. Cao, Y. Zhao, L. F. Jiao, Y. J. Wang, H. T. Yuan, *J. Mater. Chem. A* **2015**, 3, 17899-17913.

[4] W. Luo, F. Shen, C. Bommier, H. L. Zhu, X. L. Ji, L. B. Hu, *Accounts Chem. Res.* **2016**, 49, 231-240.

[5] M. R. Palacin, *Chem. Soc. Rev.* **2009**, 38, 2565-2575.

[6] Z. H. Wang, S. M. Selbach, T. Grande, *RSC Adv.* **2014**, 4, 4069-4079.

[7] Z. L. Jian, W. Luo, X. L. Ji, *J. Am. Chem. Soc.* **2015**, 137, 11566-11569.

[8] X. Wu, Y. L. Chen, Z. Xing, C. W. K. Lam, S. S. Pang, W. Zhang, Z. C. Ju, *Adv. Energy Mater.* **2019**, 9, 1900343.

[9] A. Anani, R. A. Huggins, *J. Power Sources* **1992**, 38, 351-362.

[10] Q. B. Guo, Y. F. Ma, T. T. Chen, Q. Y. Xia, M. Yang, H. Xia, Y. Yu, *ACS Nano* **2017**, 11, 12658-12667.

[11] B. Jache, P. Adelhelm, *Angew. Chem.-Int. Edit.* **2014**, 53, 10169-10173.

[12] N. Sun, Z. R. X. Guan, Y. W. Liu, Y. L. Cao, Q. Z. Zhu, H. Liu, Z. X. Wang, P. Zhang, B. Xu, *Adv. Energy Mater.* **2019**, 9, 1901351.

[13] Y. Xu, E. M. Lotfabad, H. L. Wang, B. Farbod, Z. W. Xu, A. Kohandehghan, D. Mitlin, *Chem. Commun.* **2013**, 49, 8973-8975.

[14] M. Goktas, C. Bolli, E. J. Berg, P. Novak, K. Pollok, F. Langenhorst, M. V. Roeder, O. Lenchuk, D. Mollenhauer, P. Adelhelm, *Adv. Energy Mater.* **2018**, 8, 1702724.

[15] H. Gao, T. F. Zhou, Y. Zheng, Y. Q. Liu, J. Chen, H. K. Liu, Z. P. Guo, *Adv. Energy Mater.* **2016**, 6, 1601037.

[16] R. W. Mo, D. Rooney, K. N. Sun, H. Y. Yang, *Nat. Commun.* **2017**, 8, 13949.

[17] Y. H. Xu, Y. J. Zhu, Y. H. Liu, C. S. Wang, *Adv. Energy Mater.* **2013**, 3, 128-133.

[18] C. C. Wang, L. B. Wang, F. J. Li, F. Y. Cheng, J. Chen, *Adv. Mater.* **2017**, 29, 1702212.

[19] Q. Li, Z. Q. Li, Z. W. Zhang, C. X. Li, J. Y. Ma, C. X. Wang, X. L. Ge, S. H. Dong, L. W. Yin, *Adv. Energy Mater.* **2016**, 6, 1600376.

[20] M. Xu, Q. T. Xia, J. L. Yue, X. H. Zhu, Q. B. Guo, J. W. Zhu, H. Xia, *Adv. Funct. Mater.* **2019**, 29, 1807377.

[21] J. Zhang, K. Zhang, J. Yang, G. H. Lee, J. Shin, V. Wing-hei Lau, Y. M. Kang, *Adv. Energy Mater.* **2018**, 8, 1800283.

[22] D. Saurel, B. Orayech, B. W. Xiao, D. Carriazo, X. L. Li, T. Rojo, *Adv. Energy Mater.* **2018**, 8, 1703268.

[23] D. A. Stevens, J. R. Dahn, *J. Electrochem. Soc.* **2001**, 148, A803-A811.

[24] J. T. Xu, M. Wang, N. P. Wickramaratne, M. Jaroniec, S. X. Dou, L. M. Dai, *Adv. Mater.* **2015**, 27, 2042-2048.

[25] S. Komaba, W. Murata, T. Ishikawa, N. Yabuuchi, T. Ozeki, T. Nakayama, A. Ogata, K. Gotoh, K. Fujiwara, *Adv. Funct. Mater.* **2011**, 21, 3859-3867.

[26] S. Qiu, L. F. Xiao, M. L. Sushko, K. S. Han, Y. Y. Shao, M. Y. Yan, X. M. Liang, L. Q. Mai, J. W. Feng, Y. L. Cao, X. P. Ai, H. X. Yang, J. Liu, *Adv. Energy Mater.* **2017**, 7, 1700403.

[27] K. L. Hong, L. Qie, R. Zeng, Z. Q. Yi, W. Zhang, D. Wang, W. Yin, C. Wu, Q. J. Fan, W. X. Zhang, Y. H. Huang, *J. Mater. Chem. A* **2014**, 2, 12733-12738.

[28] Y. M. Li, S. Y. Xu, X. Y. Wu, J. Z. Yu, Y. S. Wang, Y. S. Hu, H. Li, L. Q. Chen, X. J. Huang, *J. Mater. Chem. A* **2015**, 3, 71-77.

[29] Y. M. Li, Y. S. Hu, M. M. Titirici, L. Q. Chen, X. J. Huang, *Adv. Energy Mater.*

2016, 6, 1600659.

[30] S. Q. Wang, L. Xia, L. Yu, L. Zhang, H. H. Wang, X. W. Lou, *Adv. Energy Mater.* **2016**, 6, 1502217.

[31] L. F. Xiao, Y. L. Cao, W. A. Henderson, M. L. Sushko, Y. Y. Shao, J. Xiao, W. Wang, M. H. Engelhard, Z. M. Nie, J. Liu, *Nano Energy* **2016**, 19, 279-288.

[32] T. Q. Chen, Y. Liu, L. K. Pan, T. Lu, Y. F. Yao, Z. Sun, D. H. C. Chua, Q. Chen, *J. Mater. Chem. A* **2014**, 2, 4117-4121.

[33] D. A. Stevens, J. R. Dahn, *J. Electrochem. Soc.* **2000**, 147, 1271-1273.

[34] A. Ponrouch, A. R. Goni, M. R. Palacin, *Electrochem. Commun.* **2013**, 27, 85-88.

[35] Y. L. Cao, L. F. Xiao, M. L. Sushko, W. Wang, B. Schwenzer, J. Xiao, Z. M. Nie, L. V. Saraf, Z. G. Yang, J. Liu, *Nano Lett.* **2012**, 12, 3783-3787.

[36] J. Ding, H. L. Wang, Z. Li, A. Kohandehghan, K. Cui, Z. W. Xu, B. Zahiri, X. H. Tan, E. M. Lotfabad, B. C. Olsen, D. Mitlin, *ACS Nano* **2013**, 7, 11004-11015.

[37] C. Bommier, T. W. Surta, M. Dolgos, X. L. Ji, *Nano Lett.* **2015**, 15, 5888-5892.

[38] Y. L. Pan, X. D. Cheng, L. L. Gong, L. Shi, T. Zhou, Y. R. Deng, H. P. Zhang, *ACS Appl. Mater. Interfaces* **2018**, 10, 31441-31451.

[39] Y. C. Du, X. S. Zhu, X. S. Zhou, L. Y. Hu, Z. H. Dai, J. C. Bao, *J. Mater. Chem. A* **2015**, 3, 6787-6791.

[40] Z. L. Chen, R. B. Wu, M. Liu, H. Wang, H. B. Xu, Y. H. Guo, Y. Song, F. Fang, X. B. Yu, D. L. Sun, *Adv. Funct. Mater.* **2017**, 27, 1702046.

[41] F. Han, C. Z. Zhang, B. Sun, W. Tang, J. X. Yang, X. K. Li, *Carbon* **2017**, 118, 731-742.

[42] Y. Ma, Y. J. Ma, D. Bresser, Y. C. Ji, D. Geiger, U. Kaiser, C. Streb, A. Varzi, S. Passerini, *ACS Nano* **2018**, 12, 7220-7231.

[43] C. Wu, Y. Jiang, P. Kopold, P. A. van Aken, J. Maier, Y. Yu, *Adv. Mater.* **2016**, 28, 7276-7283.

[44] J. S. Cho, J. M. Won, J. K. Lee, Y. C. Kang, *Nano Energy* **2016**, 26, 466-478.

[45] Y. N. Ko, Y. C. Kang, *Carbon* **2015**, 94, 85-90.

[46] Z. Hu, Q. N. Liu, S. L. Chou, S. X. Dou, *Adv. Mater.* **2017**, 29, 1700606.

[47] Y. Xiao, J. Y. Hwang, I. Belharouak, Y. K. Sun, *Nano Energy* **2017**, 32, 320-328.

[48] A. Ponrouch, D. Monti, A. Boschin, B. Steen, P. Johansson, M. R. Palacin, *J. Mater.*

Chem. A **2015**, 3, 22-42.

[49] J. Zhang, D. W. Wang, W. Lv, L. Qin, S. Z. Niu, S. W. Zhang, T. F. Cao, F. Y. Kang, Q. H. Yang, *Adv. Energy Mater.* **2018**, 8, 1801361.

[50] K. K. Li, J. Zhang, D. M. Lin, D. W. Wang, B. H. Li, W. Lv, S. Sun, Y. B. He, F. Y. Kang, Q. H. Yang, L. M. Zhou, T. Y. Zhang, *Nat. Commun.* **2019**, 10, 725.

[51] Z. Shadike, M. H. Cao, F. Ding, L. Sang, Z. W. Fu, *Chem. Commun.* **2015**, 51, 10486-10489.

[52] S. J. Peng, X. P. Han, L. L. Li, Z. Q. Zhu, F. Y. Cheng, M. Srinivansan, S. Adams, S. Ramakrishna, *Small* **2016**, 12, 1359-1368.

Chapter 3

Experimental Methodology

Chapter 3 describes the detailed information for material synthesis and coin cell assembly. In addition, the basic working principles of material characterization and electrochemical measurements are summarized.

3.1 Material Synthesis

3.1.1 Synthesis of HICFs

Commercially available melamine sponge was purchased from Suzhou Superlong Aviation Heat Resistance Material Technology Co., Ltd. The hollow interconnected carbon foam (HICF) samples were prepared using the melamine sponge as the template through a one-step pyrolysis process at 1100 ℃ with a ramping rate of 10 ℃ min^{-1} under the argon atmosphere for 0.5, 1, and 2 h, respectively.[1] After cooling naturally in the tube furnace, the resultant HICFs were obtained and denoted as HICF-0.5, HICF-1, and HICF-2.

3.1.2 Synthesis of GF

The graphite foam (GF) was prepared using a modified chemical vapor deposition based on a previously reported method.[2, 3] In detail, some pieces of nickel foam were firstly immersed with 2 M HCl for 3 h to completely remove surface oxides and impurities. The clean nickel foam was then calcinated in a tube furnace at 1000 ℃ for 10 min under a mixed gas flow of CH_4 (150 sccm), H_2 (100 sccm) and Ar (800 sccm) to obtain graphite coated nickel foam. Finally, GF with an areal density of ~0.9 mg cm^{-2} was obtained by thoroughly etching nickel from the graphite coated nickel foam using $FeCl_3$/HCl (1 M/1 M) solution.

3.1.3 Synthesis of CoS_x NF@GF

Co_9S_8/CoS nanoflakes were grown on GF through a solvothermal route. In a typical synthesis, the solution was first prepared by dissolving 2.5 mmol of cobalt acetate tetrahydrate [$Co(CH_3COO)_2 \cdot 4H_2O$] and 2.5 mmol of thioacetamide in a mixed solvent (22 mL of H_2O/18 mL of ethanol), and then transferred into a 50 mL Teflon-lined autoclave containing a piece of GF (2.5×5 cm^2). The autoclave was sealed and maintained in an oven at 180 ℃ for 12 h. After being cooled to room temperature, the sample was rinsed with deionized water and ethanol three times, and subsequently dried at 80 ℃ in vacuum to obtain the final product marked as CoS_x NF@GF. The CoS_x loading was ~0.9 mg cm^{-2}.

3.1.4 Synthesis of CoS_x Film@GF

CoS_x Film@GF was prepared through a one-pot hydrothermal method. Typically, a piece of GF was immersed into a 40 mL of aqueous solution of 1.2 mmol of cobalt acetate tetrahydrate [$Co(CH_3COO)_2{\cdot}4H_2O$] and 1.2 mmol of thioacetamide in an autoclave, and then kept at 180 ℃ for 12 h to obtain the sample CoS_x Film@GF.

3.1.5 Synthesis of Co-MOFs NS@GF

50 mL of 0.05 M aqueous solution of cobalt nitrate hexahydrate [$Co(NO_3)_2{\cdot}6H_2O$] was quickly poured into a beaker containing 50 mL of 0.4 M aqueous solution of 2-methylimidazole [$C_4H_6N_2$] at room temperature, followed by ultrasound for 1 min.[4, 5] A piece of acid-treated GF (2.5×5 cm^2) with the bottom end pasted on a piece of glass was then immersed into the above solution and maintained for 53 min. Finally, the GF covered with purple Co-MOFs was taken out, washed with deionized water twice, and dried in 60 ℃ to obtain the product denoted as Co-MOFs NS@GF. The Co-MOFs loading was ~2.3 mg cm^{-2}.

3.1.6 Synthesis of Co-C NS@GF

A piece of purple Co-MOFs NS@GF was annealed in a tube furnace under the Ar/H_2 (97:3) atmosphere at 350 ℃ for 20 min with a ramp rate of 2 ℃ min^{-1}, followed by increasing temperature to 800 ℃, 870 ℃, and 900 ℃, respectively, with a heating rate of 5 ℃ min^{-1} and holding time for 2 h. After cooling down, the black samples were collected and marked as Co-C NS@GF-800, Co-C NS@GF-870, and Co-C NS@GF-900.

3.1.7 Synthesis of Co_9S_8-C NS@GF

The as-prepared Co-C NS@GF at the above different temperatures was separately sulfurized at 650 °C for 2 h with a ramp rate of 2 °C min^{-1} in a tube furnace, accompanied with ~40 mg sulfur powder at the upstream side under a gas flow of Ar/H_2 (97:3, 50 sccm). After cooling down, the products were obtained and denoted as Co_9S_8-C NS@GF-800, Co_9S_8-C NS@GF-870, and Co_9S_8-C NS@GF-900. The mass loading of Co_9S_8-C NS was ~0.9 mg cm^{-2}.

3.2 Coin Cell Assembly

For all the electrochemical performance test, CR2032 coin half cells (Figure 3.1) were assembled in an Ar-filled glove box (O_2 < 0.1 ppm, H_2O < 0.1 ppm).[6] For CoS_x NF@GF-based cells, a freestanding CoS_x NF@GF (a punched disk with a diameter of 10 mm) without any binder or additive was used as the working electrode, a disk of sodium foil was used as the counter electrode, as well as glass fiber (Whatman GF/D) was used as the separator. Two different electrolytes were used, one was 1 M $NaCF_3SO_3$ in diethylene glycol dimethyl ether (diglyme) and the other was 1 M $NaCF_3SO_3$ in ethylene carbonate (EC)/diethyl carbonate (DEC) (1:1 in volume). The assembling procedure of HICF-based, GF-based, CoS_x Film@GF-based, Co-C NS@GF-based, and Co_9S_8-C NS@GF-based cells was the same as that of CoS_x NF@GF. The mass loading of active materials was about 0.8-1.2 mg cm^{-2}.

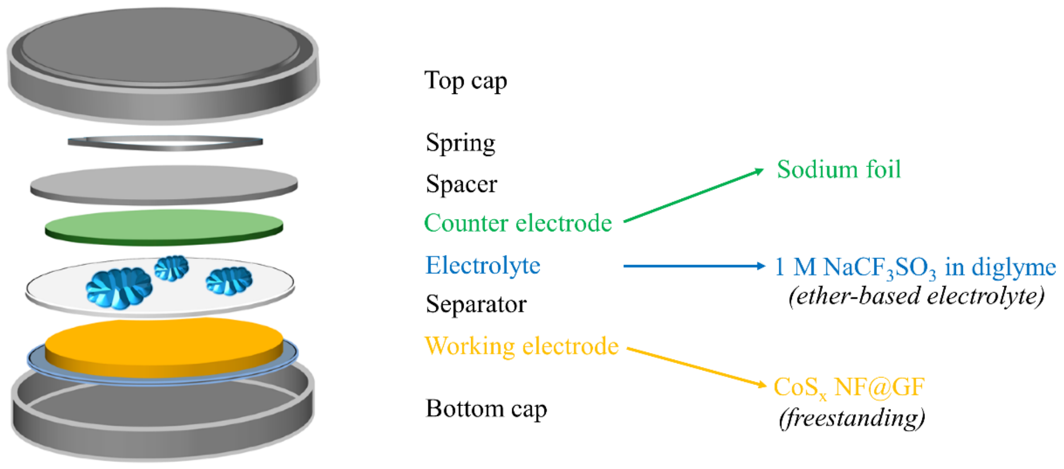

Figure 3.1 Schematic illustration of a CR2032 coin half cell.[6]

3.3 Material Characterization

3.3.1 X-ray Diffraction (XRD)

The X-ray diffraction (XRD) technique can be used to quickly identify the phase structure of a crystalline material. The fundamental principles of XRD are built on constructive interference of monochromatic X-rays and a crystal. In detail, crystalline samples can function as diffraction gratings for X-rays, as interplanar spacing is similar to X-ray wavelength. When monochromatic X-rays interact with a crystalline substance, the constructive interference can occur if the Bragg's law ($n\lambda=2d \sin \theta$) is satisfied (Figure 3.2). Here n is a positive integer, λ is the wavelength of the X-rays, d is the lattice spacing between adjacent diffracting planes, and θ is the incident angle of the X-rays. Through scanning the sample in the angle range of 2θ and collecting the corresponding diffracted X-rays, all possible d-spacings in the sample lattice can be obtained. Typically, the crystal structure of the sample can be identified by comparing these d-spacings with standard reference patterns.

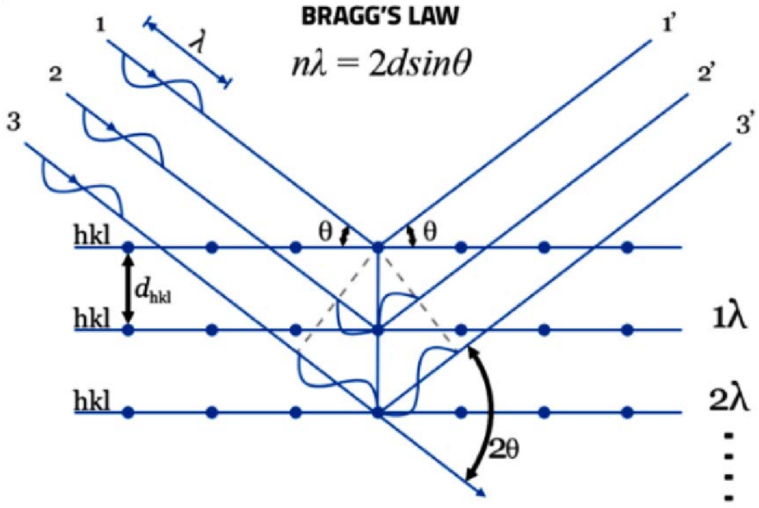

Figure 3.2 Scheme of Bragg's law.

A typical X-ray diffractometer includes three basic components: X-ray tube, sample holder, and X-ray detector (Figure 3.3). The monochromatic X-rays are generated from the X-ray tube, where electrons produced by heating the cathode filament are accelerated with a voltage to bombard the target material (such as the most common used Cu), thus generating X-rays. These X-rays are then filtered to obtain monochromatic X-rays (such as λ=1.5418 Å for CuK_α radiation), which can be directed onto the sample and the resultant diffracted X-rays are recorded and processed by the X-ray detector.

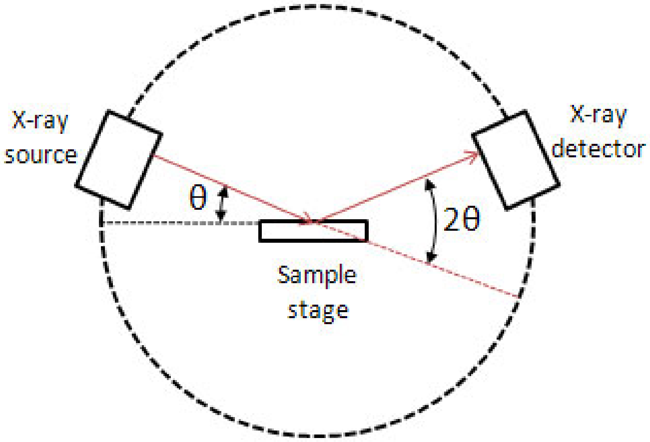

Figure 3.3 Scheme of an X-ray diffractometer.

3.3.2 Scanning Electron Microscopy (SEM)

The scanning electron microscopy (SEM) can be used to observe the morphology and topography of a solid sample. The fundamental principles of SEM are based on the interactions between electrons and the surface of the sample. In detail, the accelerated and focused electron beams collide with the sample surface and are decelerated to generate different types of signals, including secondary electrons, backscattered electrons, and characteristic X-rays, shown in Figure 3.4. Among them, the former two signals are commonly used to picture the samples, in which the secondary electrons are responsible for displaying the morphology and topography of specimens and the backscattered electrons are responsible for illustrating contrasts of different elements in the specimens.

The secondary electrons come from the top surface atoms within a few nanometers of a sample due to the inelastic interactions of the primary electron beams with the sample. In addition, the signals from the secondary electrons are highly confined to the specific positions where primary electron beams impact, making them precisely reflect the detailed surface information of the sample with a high resolution. By contrast, the backscattered electrons originate from deeper regions of the sample as a result of elastic scattering of the primary electron beams and thereby belong to the primary electron beams. Moreover, the signal intensities of the backscattered electrons strongly depend on the atomic number (Z) of elements within the specimens. The higher atomic number generally leads to the brighter region in the SEM image, providing the distribution information of different elements of the sample.

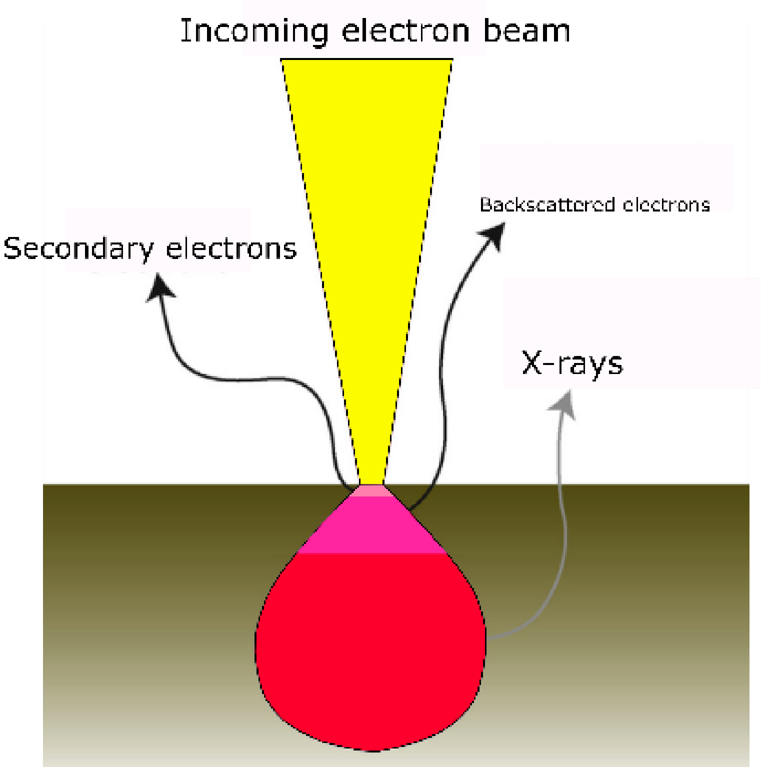

Figure 3.4 Different kinds of signals detected by SEM and the corresponding areas from which they originate.

The basic components of an SEM are shown in Figure 3.5. Typically, electron beams are firstly emitted from the electron source normally using tungsten filament cathode, then accelerated by the positively-charged anode and focused to a spot by the condenser lens, and finally collide with the sample surface to generate a variety of signals, which are collected by the corresponding detectors. In addition, the whole electron column should be kept high vacuum, as the vacuum condition can remove other atoms and molecules in the column, which may collide with the electron beams to deflect these beams, therefore leading to poor image quality.

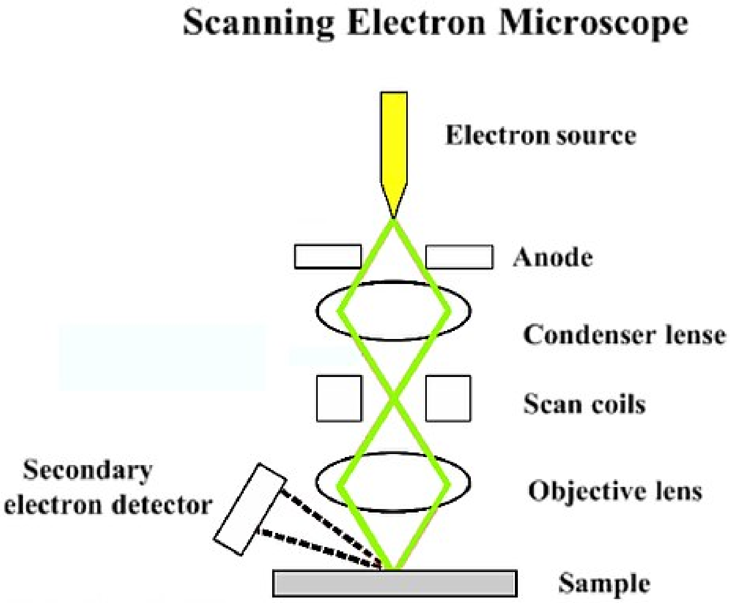

Figure 3.5 Basic components of an SEM.

3.3.3 Energy-Dispersive X-ray Spectroscopy (EDS)

Energy-dispersive X-ray spectroscopy (EDS) is a powerful technique to analyze the elemental compositions of a specimen. The main principle of EDS is that each element can emit characteristic X-rays due to its unique atomic structure. Figure 3.6 gives an example of how EDS operates. One atom consists of an atomic nucleus and electrons. The electrons are located at different energy levels (n=1, 2, 3, …) corresponding to the letters K, L, M, in which electrons at K level are the nearest to the atomic nucleus and possess the lowest energy. In addition, the size of electron transition between different energy levels is represented by α and β. For example, the electron transition from L to K is named as K_{α}, while the relaxation from M to K is denoted as K_{β}.

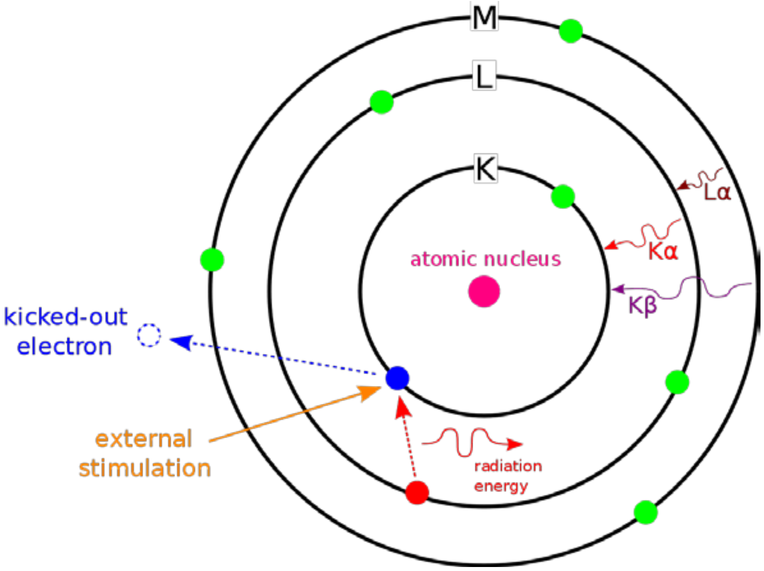

Figure 3.6 Principle of EDS.

The EDS equipment is commonly integrated into the SEM instrument. As stated before in the section of SEM, the characteristic X-rays are also emitted from the deepest surface area of the sample by the inelastic collision of high-energy electron beams, except for the secondary electrons and backscattered electrons. In detail, at rest, the electrons within an atom of the sample are in the ground state (or unexcited) distributed in discrete energy levels. The incident electron beams (external stimulation) with high energy can create an electron hole in an inner shell through exciting and ejecting the corresponding inner electron (kicked-out electron) from the shell. Then, an outer electron in a higher energy level automatically jumps into the electron hole with a lower energy level, accompanying with the emission of characteristic X-rays (radiation energy) with the energy of the difference between the two energy levels. The energy of X-rays depends on the specific energy difference between the two electron shells, which is a unique value for different atoms, therefore the emitted X-rays can function as the fingerprint for each element and different elements in the sample can be identified by EDS.

An energy-dispersive spectrometer typically includes four major parts: an excitation source (electron beams), an X-ray detector, a pulse processor, and an analyzer, illustrated in Figure 3.7. The electron beams come from the SEM equipment. The X-ray detector commonly uses Si(Li) crystals, which can absorb and convert individual characteristic X-rays into voltage signals with proportional values to the energy of X-rays. These signals are then measured by the pulse processor and finally sent to the analyzer.

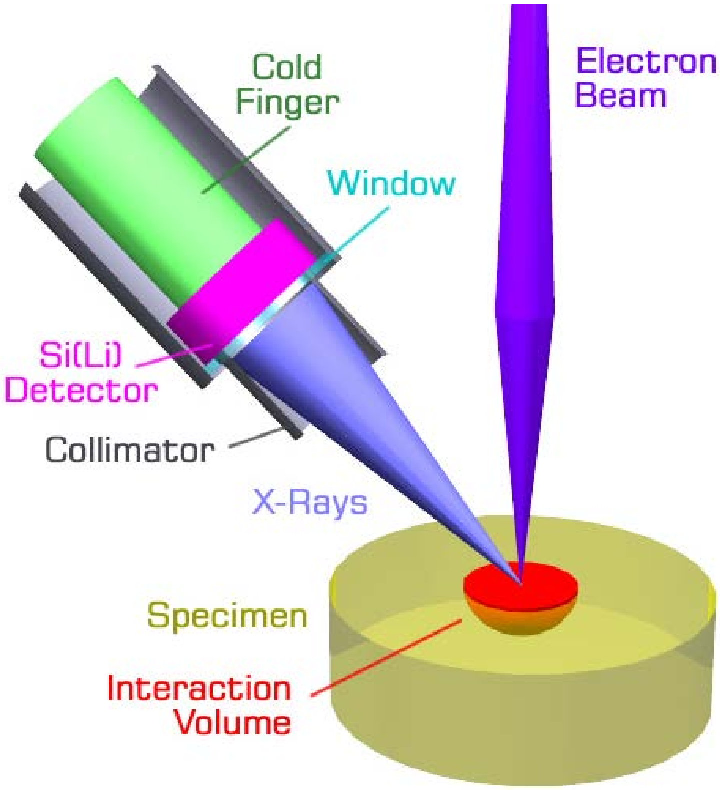

Figure 3.7 Scheme of an energy-dispersive spectrometer.

3.3.4 Transmission Electron Microscopy (TEM)

Transmission electron microscopy (TEM) is a powerful tool to provide the information about the morphology, structure and crystallization of a specimen, whereas SEM only shows the morphology. In addition, TEM can observe the sample with a higher resolution, compared with SEM. TEM works on the same basic principles as a light microscope and they share similar organizations, shown in Figure 3.8. The major difference is that TEM uses electrons as the illumination source instead of light in the light microscope. Owing to the much shorter wavelength of electrons than that of light, TEM can be used to visualize the specimen with much higher magnification and resolution compared to the light microscope. Another obvious difference is that TEM uses the electromagnetic lens to focus electrons, while the glass lens is employed to focus light in the case of light microscopes.

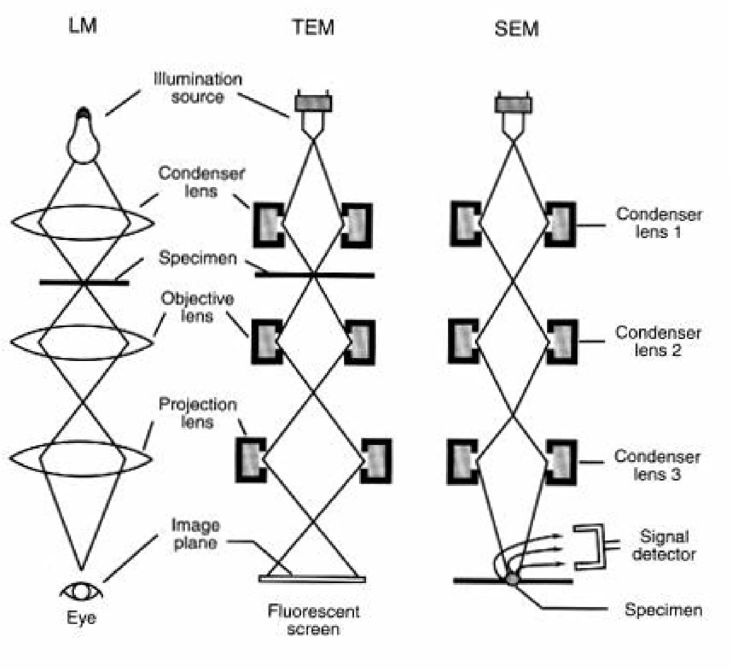

Figure 3.8 The general layouts of TEM, light microscope and SEM.

The TEM instrument is composed of three essential systems: (1) the electron gun and the condenser lens, (2) the image-producing system including the movable specimen stage, the objective lens, the intermediate lens and the projection lens, (3) the image-recording system including the fluorescent screen and the digital camera. The imaging process is as follows. The high-energy electron beams are generated from the electron gun and focused by the condenser lens. These beams then strike an ultrathin specimen, which is semi-transparent to electrons, therefore parts of the incident electrons are transmitted. The transmitted electron beams are focused by the objective lens into an electron image (a micrograph), which is further enlarged by the intermediate lens and the projection lens. Finally, the electron image hits the fluorescent screen to generate light, which allow operators to see the image. The image is captured digitally by the charge-coupled device (CCD) camera. Additionally, to prevent gas atoms from colliding with and deflecting the electron beams, the column in the TEM maintains high vacuum.

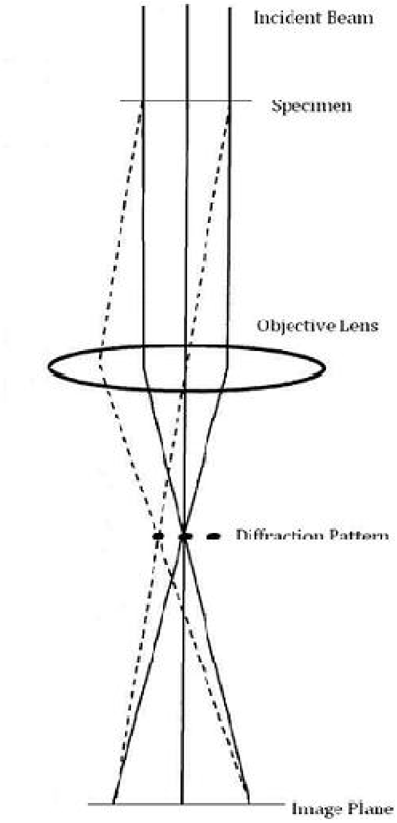

Figure 3.9 The ray diagram for the imaging and diffraction mechanism in TEM.

Figure 3.9 sketches the path of electron beams in the TEM. When the incident electron beams go through the specimen, they are scattered by the specimen. The objective lens can focus the scattered electrons from one point of the sample into the opposite position on the image plane to form the image, the corresponding path is represented by the dotted line. Besides, the scattered electrons with the same direction are focused by the objective lens into a single point on the back focal plane of the objective lens, forming the diffraction pattern.

3.3.5 X-ray Photoelectron Spectroscopy (XPS)

X-ray photoelectron spectroscopy (XPS) as a surface technique can be employed to analyze the elemental composition as well as the chemical and electronic states of the elements at the surface of a sample (1-10 nm). The fundamental principle of XPS is based on the photoelectric effect, which was first explained by Albert Einstein in 1905 (Nobel Prize in Physics 1921). In detail, as shown in Figure 3.10, the incident X-rays with sufficiently high energy of h*v* (typically Al K_α) irritate a specimen to eject the core level electrons (such as 1s electrons) of the sample atoms to pass through the Fermi level and the free electron level (also called as the vacuum level) and emerge as the photoelectrons with remnant kinetic energy E_{kin}. Only the photoelectrons close enough to the sample surface (within 10 nm) can escape from the sample and be collected by the electron detector with discriminating and measuring their kinetic energy E_{kin} and number.

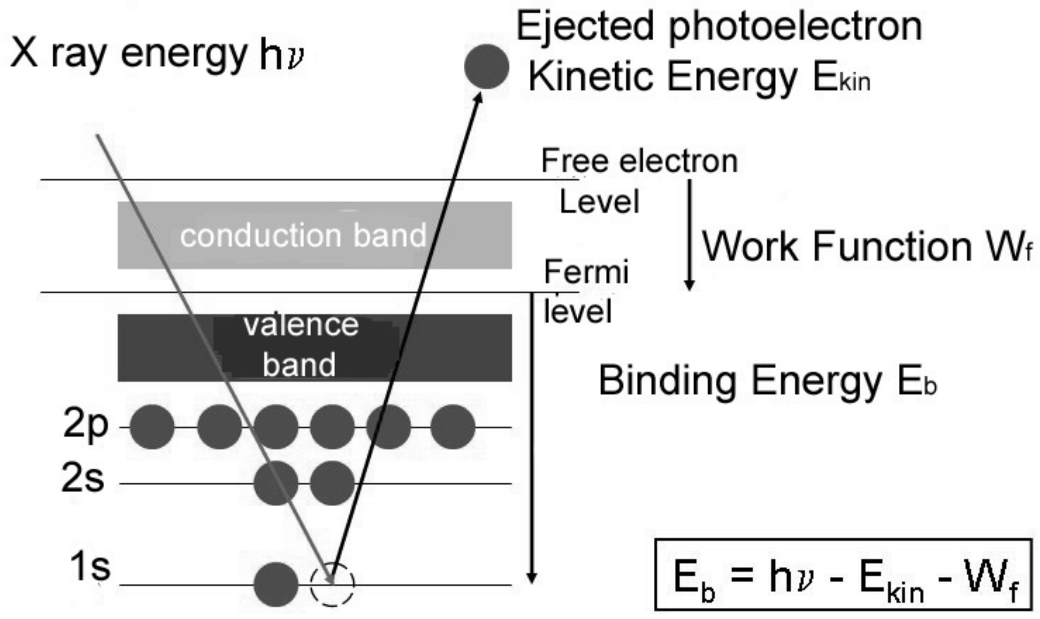

Figure 3.10 The principle of XPS.

The measured E_{kin} can be used for calculating the binding energy E_b of the corresponding electrons (the minimum energy required for electrons to escape from the attraction of the nucleus), according to the equation in Figure 3.10. W_f is the work function, representing the minimum energy needed for electrons to escape from the atom. The resulting XPS spectrum reflect the relationship between the binding energy E_b of electrons and the corresponding intensity (represented by counts per second of electrons hitting the detector).

The E_b value of each peak in the spectrum can be indexed to a certain element within the sample through comparing them with the reference database, which thus can determine the elemental composition of the sample. The corresponding elemental content can also be calculated from the peak intensity of each element. In addition, the chemical and electronic states of each element can be revealed by the subtle chemical shifts in binding energy, because the binding energy E_b is not only determined by the shell where electrons are positioned, but also affected by the chemical environment of atoms, that is, the chemical bonds with another atom.

3.3.6 Raman Spectroscopy

Raman spectroscopy can be used to analyze the chemical and structural information of a sample. The basic principle of Raman spectroscopy is using Raman scattering to detect the molecular vibrations within the sample. The Raman scattering was first discovered by the Indian physicist C. V. Raman in 1928 (Nobel Prize in Physics 1930). Generally, light interacts with matter in four major ways, including absorption, reflection, transmission, and scattering, illustrated in Figure 3.11. When light (such as a laser) is scattered by a molecule of a sample, the molecule absorbs the photon energy through molecular vibrations to enter a higher energy state (commonly called the virtual state), which is very unstable and immediately re-emits a photon as scattered light. Among them, most of the scattered light maintain the same energy as that of the incident light, which is called Rayleigh scattering belonging to an elastic scattering, shown in Figure 3.12. A tiny fraction of the scattered light (nearly 1 in 10 million) loses or gains energy, named as Raman scattering belonging to an inelastic scattering, as a result of energy transfer between incident photons and molecular vibrations of sample. The Raman scattering includes two types: Stokes (energy is lost) and anti-Stokes (energy is gained). As the Stokes Raman light is more intense than the anti-Stokes, the Raman spectroscopy always measures the Stokes Raman scattering.

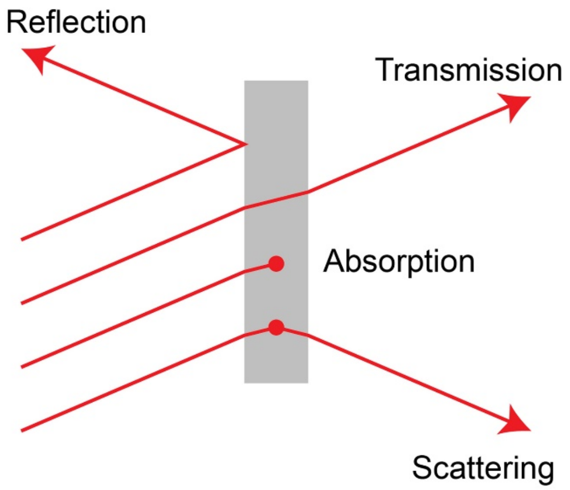

Figure 3.11 Four major ways light interacts with matter.

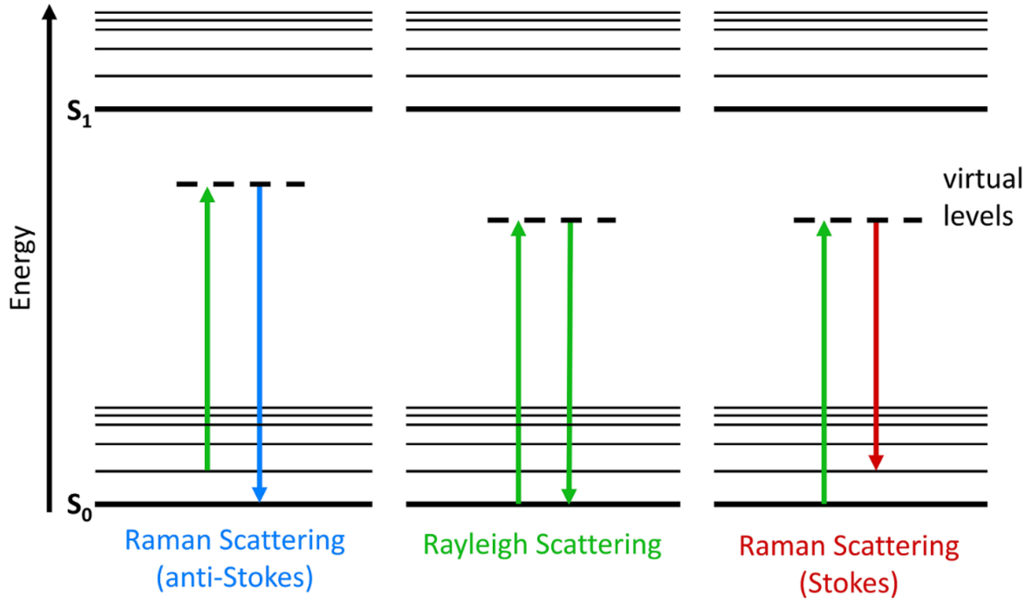

Figure 3.12 Three types of scattering.

3.4 Electrochemical Measurements

3.4.1 Cyclic Voltammetry (CV)

Cyclic voltammetry (CV) as the most important potential technique can be used to understand the electrochemical reactions of electrodes. The basic principle of the CV technique is to monitor the current response to applied potential.[7] To conduct a CV measurement, two terminal potentials (E_1 and E_2) and a scan rate (v) need to be set up. Typically, the applied potential (E) between E_1 and E_2 evolves with time in a linear scan mode, shown in Figure 3.13a. The corresponding current response (i) is recorded for a single electrochemical reaction, where the peak potential (E_p) and current (i_p) are important values in Figure 3.13b. The subscripts c and a refer to the cathodic and anodic scans, respectively. One peak potential (E_p) represents a specific electrode reaction occurring at this potential. The peak current (i_p) is corelated with the faradic capacity of the electrode reaction.

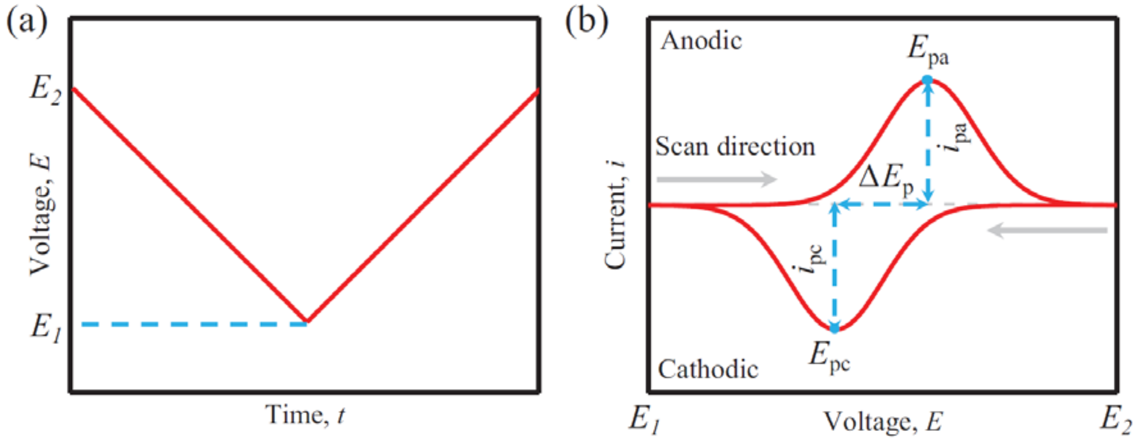

Figure 3.13 (a) The evolution of applied potential with time, (b) current response to applied potential in a CV measurement.[7]

When the current in the CV curves is transformed to the faradic capacity, the profiles of potential versus faradic capacity are obtained, shown in Figure 3.14. The charge and discharge plateaus correspond to the potentials of anodic (E_{pa}) and cathodic (E_{pc}) peaks, respectively. In addition, the criteria for appropriate terminal potentials (E_1 and E_2) are that the electrode reactions happen between E_1 and E_2, as well as the current almost decreases to zero at the terminal potentials. The appropriate scan rate (v) is from 0.1 to 10 mV s^{-1} (commonly slow) in batteries to ensure that the integral capacity approximates to the theoretical capacity of electrode materials.

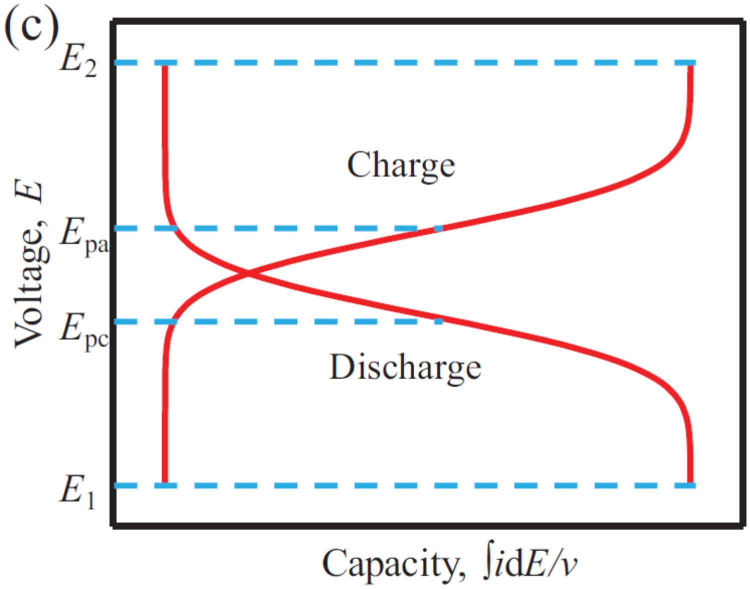

Figure 3.14 The profiles of potential versus faradic capacity.[7]

3.4.2 Galvanostatic Charge-Discharge (GCD)

Galvanostatic charge–discharge (GCD) as an important galvanic technique can be used to evaluate various electrochemical properties of electrode materials, including the capacity, reversibility, cycling and rate performance. The basic principle of the GCD technique is to monitor the potential response to constant applied current.[7] To perform a GCD measurement, two terminal potentials (E_1 and E_2) also need to be set up, commonly the same as those of the CV measurement. The evolution of constant applied current (i) with time is shown in Figure 3.15a. The corresponding potential response (E) versus capacity (calculated from *i*, time, and mass of active electrode materials) is recorded, where plateaus can be recognized in Figure 3.15b. The charge and discharge plateaus (E_C and E_D) correspond to the potentials of anodic (E_{pa}) and cathodic (E_{pc}) peaks in the CV curves, respectively. In addition, the current (*i*) in the GCD measurement is commonly normalized to specific current (in the unit of mA g^{-1}) based on the mass of active electrode materials, corresponding to specific capacity (mAh g^{-1}).

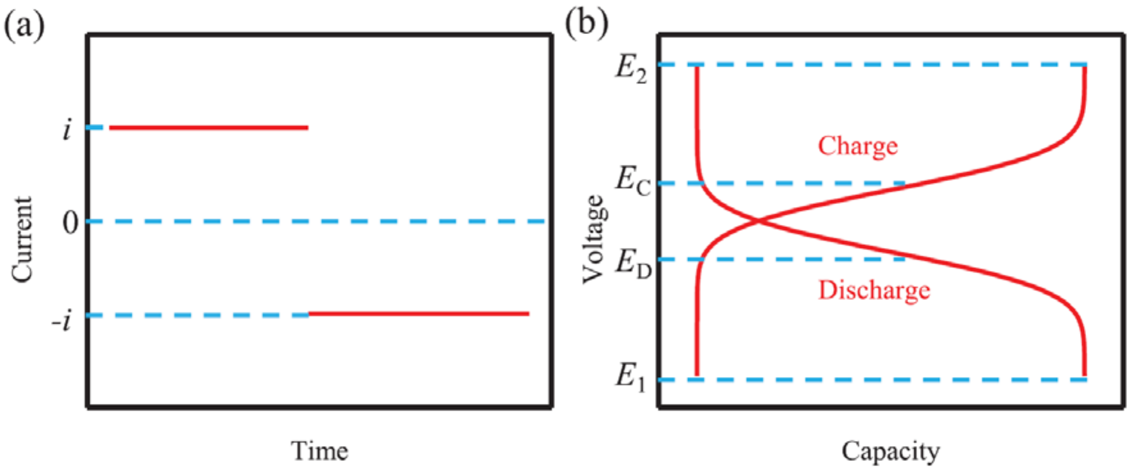

Figure 3.15 (a) The evolution of constant applied current with time, (b) potential response to capacity in a GCD measurement.[7]

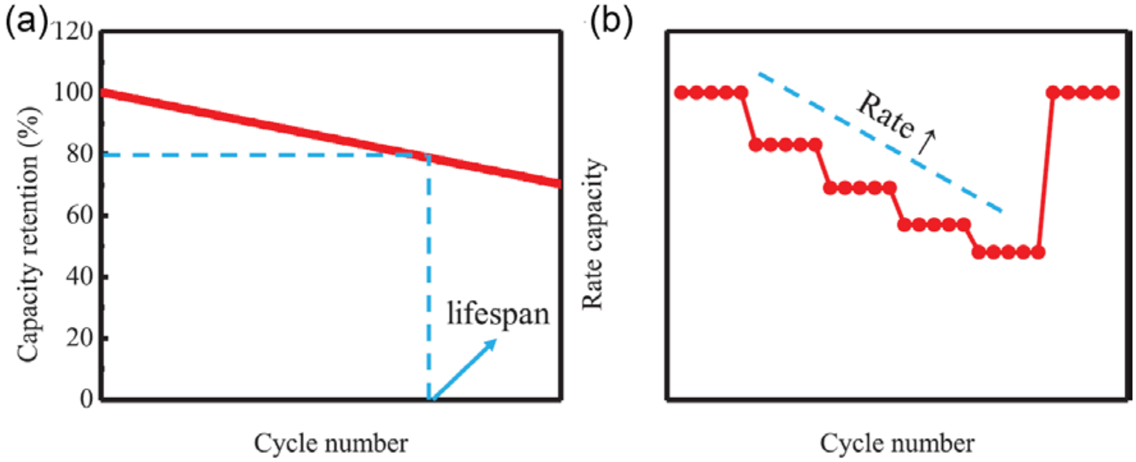

Figure 3.16 (a) Cycling stability and (b) rate capability assessed by the GCD technique.[7]

The cycling stability of electrode materials is the most important property of secondary batteries. The cycling stability can be evaluated by repeated GCD procedures, in which battery lifespan is defined as the cycle number corresponding to the 80% capacity retention of the initial reversible capacity, shown in Figure 3.16a. Furthermore, the rate capability can be assessed using GCD procedures with a series of increased currents in Figure 3.16b. Typically, the capacity drops with increased current because of aggravated polarization. It should be emphasized that if the capacity decreases drastically at specific current rate, the evaluation at higher rate will be meaningless.

3.4.3 Electrochemical Impedance Spectroscopy (EIS)

Electrochemical impedance spectroscopy (EIS) as an important impedance technique can be used to measure charge transfer resistance (R_{ct}) and calculate ion diffusion coefficient (D) of electrode materials. The fundamental principle of EIS is based on linear current response to small sinusoidal potential.[7] In an EIS measurement, the amplitude of sinusoidal potential is only a few mV and the frequency range is usually 10^{-2}-10^{5} Hz. The EIS data are typically given in the form of Nyquist plot (the inverse imaginary part of impedance versus its real part), shown in Figure 3.17a. The corresponding equivalent electrical circuit (Randles circuit model) is composed of resistors and capacitors, specifically R_{int} (internal resistance), R_{ct}, Z_w (Warburg impedance), and C_{dl} (double layer capacitance).

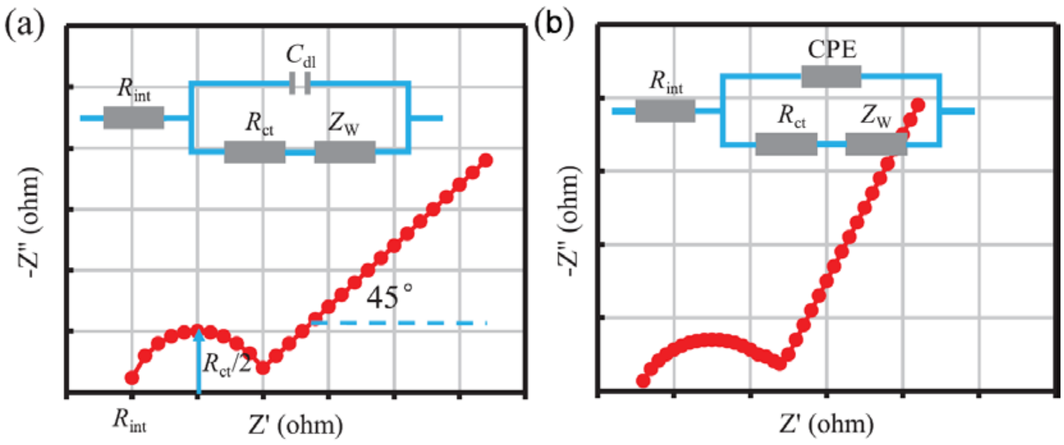

Figure 3.17 (a) The Nyquist plot (in red) and the corresponding equivalent electrical circuit (in blue), (b) the deviation of EIS data.[7]

R_{ct} can be identified as the diameter of the semicircle in high-frequency region of Nyquist plot, and R_{int} is the starting point. The low-frequency region appears as a slope at 45°, which can be used to calculate ion diffusion coefficient (D). In addition, the deviation of EIS data from the standard Randles model usually occurs in practice, where the semicircle is replaced with an arc and the slope is not at 45°, shown in Figure 3.17b.

References

[1] D. S. Bin, X. J. Lin, Y. G. Sun, Y. S. Xu, K. Zhang, A. M. Cao, L. J. Wan, *J. Am. Chem. Soc.* **2018**, 140, 7127-7134.

[2] Z. P. Chen, W. C. Ren, L. B. Gao, B. L. Liu, S. F. Pei, H. M. Cheng, *Nat. Mater.* **2011**, 10, 424-428.

[3] J. L. Liu, L. L. Zhang, H. B. Wu, J. Y. Lin, Z. X. Shen, X. W. Lou, *Energy Environ. Sci.* **2014**, 7, 3709-3719.

[4] C. Guan, A. Sumboja, H. J. Wu, W. N. Ren, X. M. Liu, H. Zhang, Z. L. Liu, C. W. Cheng, S. J. Pennycook, J. Wang, *Adv. Mater.* **2017**, 29, 1704117.

[5] G. Z. Fang, J. Zhou, C. W. Liang, A. Q. Pan, C. Zhang, Y. Tang, X. P. Tan, J. Liu, S. Q. Liang, *Nano Energy* **2016**, 26, 57-65.

[6] E. Talaie, P. Bonnick, X. Q. Sun, Q. Pang, X. Liang, L. F. Nazar, *Chem. Mat.* **2017**, 29, 90-105.

[7] X. M. Yang, A. L. Rogach, *Adv. Energy Mater.* **2019**, 9, 1900747.

Chapter 4

Maximized Pseudo-Graphitic Content in Self-Supported Hollow Interconnected Carbon Foam Boosting Ultrastable Na-Ion Storage

Herein, a self-supported hollow interconnected carbon foam (HICF) is developed by one-step pyrolysis of a commercial and low-cost melamine sponge. The integration of interconnected network and hollow feature can not only provide strong mechanical stability and additional inner space to effectively accommodate the structural deformation from Na^+ *insertion/extraction, but also enable fast electron and Na-ion transport to achieve a large reversible capacity. As a result, HICF delivers a large reversible capacity of 305.7 mAh* g^{-1} *at 100 mA* g^{-1} *and an ultralong cycle life with 86.4% capacity retention over 1000 cycles at 1000 mA* g^{-1}*. The superior Na-storage performance is also contributed by the maximized content (63.24%) of pseudo-graphitic phase in HICF realized by tuning pyrolysis time, as the pseudo-graphitic phase could store more sodium ions and maintain more stable microstructure owing to its appropriate d-spacing than highly disordered phase.*

---

*This section published substantially as X.L. Ye, H.S. Wang, Z.F. Chen, M. Li, T. Wang, C. Wu, J.X. Zhang, and Z.X. Shen. Maximized Pseudo-graphitic Content in Self-supported Hollow Interconnected Carbon Foam Boosting Ultrastable Na-Ion Storage. *Electrochimica Acta*, **2021**, 371, 137776. Reprinted with permission. Copyright (2021) Elsevier Ltd.

4.1 Introduction

Due to the depletion of fossil resources, renewable and clean energy technologies are urgently needed to establish a global green economy.[1] Lithium-ion batteries (LIBs) have become the mainstream in energy storage field due to the high energy density and long cycle life over the past few decades. Nonetheless, the ever-growing demand of LIBs leads to a relatively high price for lithium resources, which restricts their further large-scale applications.[2] As a low-cost alternative, sodium-ion batteries (SIBs) have recently inspired growing interest due to the inexpensive and abundant sodium resources.[3, 4] However, it is still challenging to develop low-cost and high-performance electrodes for SIBs.[5]

Compared with other anode choices (such as transition metal sulfides, alloys, and organic materials), hard carbons are considered as the most promising commercialized Na-storage anodes, owing to the suitable reversible capacity (150-350 mAh g^{-1}), low potential plateau (~0 V vs. Na^+/Na), inexpensiveness, and high abundance.[6-8] However, it is still a great challenge to design highly stable hard carbon anodes coupled with a large reversible capacity to effectively alleviate the structural deformation, resulting from repeated intercalation/deintercalation of sodium ions with much larger radius (1.02 Å) than that of lithium ions (0.76 Å).[9, 10]

Recently, three-dimensional interpenetrating carbon architectures as self-supported electrodes have attracted great interest in different electrochemical systems.[11-14] Owing to its structural integrity, the carbon network can not only tolerate the repeated structural deformation induced by electrochemical reactions, but also provide interconnected channels to accelerate ion/electron transport, which should be especially crucial for the large and sluggish Na ions.[15] As the self-supported electrode, the carbon network can directly act as an electrode and avoid the cumbersome slurry-casting electrode fabrication method, which needs polymer binders, conductive additives, solvents, and metal current collectors.[7] Additionally, hollow structures were demonstrated to greatly boost the cycling stability of conversion-type and alloying-type negative materials with severe volume changes during the electrochemical reactions through providing extra inner cavity to alleviate the induced strains.[16-19] The hollow structure can also shorten the ionic diffusion distance to achieve a larger reversible capacity, compared with the solid one at the same current rate.[20] Therefore, the advantageous combination of self-supported carbon network with hollow structure is very promising to achieve the hard carbon anodes with both long cycling stability and large reversible capacity for SIBs.

Herein, we developed a free-standing hollow interconnected carbon foam (HICF) via one-step pyrolysis of a commercial and low-cost melamine sponge. The integrated hollow carbon network could not only provide the strong structural stability and additional inner space to ensure repeated sodiation/desodiation process, but also enable fast electron and Na-ion transport to achieve a large reversible capacity. As a self-supported Na-ion anode, HICF delivered a high reversible capacity of 305.7 mAh g^{-1} at 100 mA g^{-1} and an ultralong cycle life with 86.4% capacity retention over 1000 cycles at 1000 mA g^{-1}. Furthermore, the high content (63.24%) of pseudo-graphitic phase (d_{002}-spacing between 0.36 and 0.40 nm) in HICF realized by tuning pyrolysis time also contributed to the superior Na-storage performance, as the pseudo-graphitic phase could not only store more Na ions but also maintain more stable microstructure than highly disordered phase (d_{002}-spacing above 0.40 nm). This work provided a low-cost and high-performance anode candidate for the future practical applications of SIBs.

4.2 Results and Discussion

Figure 4.1a displays the representative scanning electron microscopy (SEM) image of commercial melamine sponge precursor, which owned porous interconnected structure with units of tetrapod-shaped joints and rod-shaped fibers. After carbonization at 1100 °C for 1 h with a ramping rate of 10 °C min^{-1} under argon atmosphere, the white melamine sponge was converted into black HICF-1, accompanied with a shrinkage in volume. As shown in Figure 4.1b, HICF-1 not only inherited the backbone structure of the melamine sponge precursor, but also evolved into a distinct bubble structure with a diameter of ~10 μm in the position of joint. Besides, a hollow interconnected structure was observed in the cross sections of the rod-shaped fiber and tetrapod-shaped joint (Figure 4.1c, d), which was contributed by the skeleton self-inflation resulting from fast gas release at the high heating rate of 10 ℃ min^{-1}.[14] Additionally, the HICF-0.5 and HICF-2 obtained at 1100 ℃ with different heat holding time (0.5 and 2 h) showed similar morphology to HICF-1, except a little difference of surface feature.

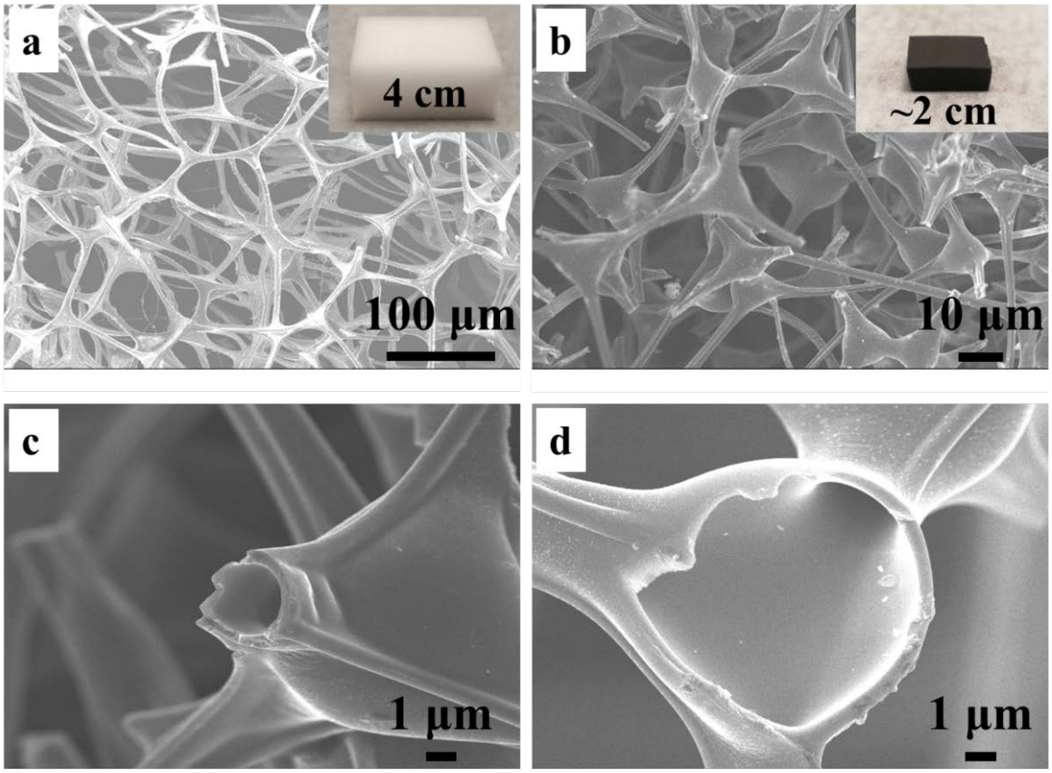

Figure 4.1 SEM images of (a) melamine sponge precursor (Inset: a photograph of melamine sponge), (b) HICF-1 (Inset: a photograph of HICF-1) and (c, d) the hollow interconnected structures of HICF-1.

The crystal structures of the above three HICF samples were studied by X-ray diffraction (XRD), displayed in Figure 4.2a. All the samples showed broad peaks at ~24° and ~44° corresponding to the (002) and (101) diffractions of hard carbon, indicating an amorphous structure.[21] In addition, the (002) diffraction peaks could be simulated by a profile-fitting process to further investigate the microcrystalline evolution in HICF with pyrolysis holding time. Generally, the carbon phases could be classified into three types according to the *d*-spacing values.[8] (1) When the *d*-spacing is less than 0.36 nm, the phase is named as the graphite-like carbon, whose interlayers are too small for Na ions to enter. (2) With a larger *d*-spacing between 0.36 and 0.40 nm, the carbon phase with relatively ordered microcrystallites is favorable for the Na-ion insertion/extraction process, which is defined as pseudo-graphitic carbon.[8, 22, 23] (3) With the *d*-spacing exceeding 0.40 nm, the carbon microcrystallites are much more disordered, leading to a decreased resistance during the sodium ion migration process.[20, 24]

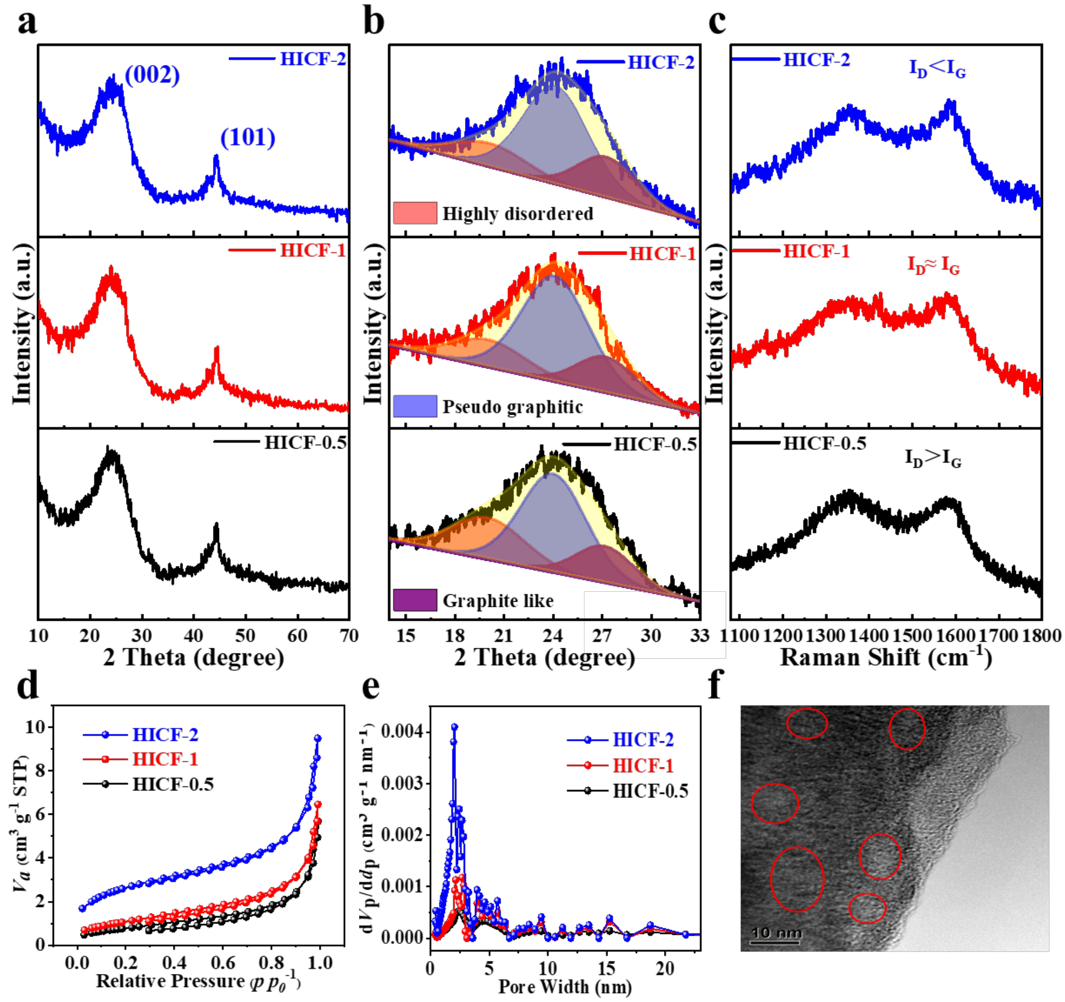

Figure 4.2 (a) XRD patterns, (b) fitting results of the (002) diffraction peaks, (c) Raman spectra, (d) Nitrogen adsorption-desorption isothermal curves and (e) the corresponding pore size distributions of the three HICF samples; (f) HRTEM image of HICF-1.

To guarantee the accuracy and reliability of the fitting results, the full width at half-maximum (FWHM) of each kind of carbon phase in the three HICF samples was fixed at specific value and the corresponding results were shown in Figure 4.2b. The detailed fitting information of *d*-spacing and area is listed in Table 4.1. As expected, each HICF included three different kinds of carbon phase, of which the peak values moved to a higher degree with the prolonged heat holding time. Besides, HICF-0.5 possesses the highest proportion of disordered microcrystallite structure (26.54%) and the lowest proportion of graphite-like carbon (18.17%) among the three HICF samples. By contrast, the lowest proportion of highly disordered carbon (16.44%) and the highest proportion of graphite-like carbon (22.27%) existed in HICF-2, indicating that the highly disordered phase transforms to the pseudo-graphitic phase gradually, and finally into the graphite-like phase with increase in heating duration. This is also demonstrated by the Raman spectra (Figure 4.2c), where the broad peak at ~1590 cm^{-1} (the G-band) corresponds to the sp^2 bonds specific for the graphitic structure while the peak at ~1355 cm^{-1} (the D-band) represents the disordered structure.[25] With the prolonged pyrolysis holding time, the intensity of G-band increases with respect to that of D-band, and finally exceeds that of D-band, further revealing the gradual increase of graphitization degree.

Table 4.1 Physical parameters of the HICF samples from XRD.

Sample	**Highly Disordered**			**Pseudo-Graphitic**			**Graphite-Like**		
	2θ /°	**d_{002} /nm**	**Area /%**	**2θ /°**	**d_{002} /nm**	**Area /%**	**2θ /°**	**d_{002} /nm**	**Area /%**
HICF-2	20.14	0.440	16.44	24.17	0.368	61.29	27.28	0.327	22.27
HICF-1	20.07	0.442	18.17	24.14	0.368	63.24	27.25	0.327	18.59
HICF-0.5	20.04	0.443	26.54	24.03	0.370	55.29	27.18	0.328	18.17

Figure 4.2d, e show the nitrogen adsorption-desorption isotherms and corresponding pore-size distributions of the HICF samples with the detailed data in Table 4.2. HICF-0.5

possessed the smallest specific surface area of 2.91 m^2 g^{-1} and pore volume of 0.0085 cm^3 g^{-1} with a concentrated pore distribution between 0 and 5 nm. With prolonged pyrolysis time, the specific surface area and pore volume became larger (9.18 m^2 g^{-1} and 0.0141 cm^3 g^{-1} for HICF-2) due to more and more pores created by small molecules gradually escaping from the HICFs. The high-resolution transmission electron microscopy (HRTEM) of HICF-1 (Figure 4.2f) confirmed the existence of nanopores, circled in red. These nanopores can act as Na-storage active sites and reduce Na^+ diffusion distance. Furthermore, the specific surface areas of HICFs were much lower than those of some reported sodium-storage hard carbon materials, which might be in favor of limiting the solid electrolyte interphase (SEI) formation and thereby improving the initial Coulombic efficiency.[10, 15, 26]

Table 4.2 Physical parameters of the HICF samples from N_2 adsorption-desorption isotherm and XPS.

Sample	XPS			BET	V_p
	C /%	N /%	O /%	/m^2 g^{-1}	/cm^3 g^{-1}
HICF-2	89.68	1.13	9.19	9.18	0.0141
HICF-1	88.54	1.46	10.00	4.06	0.0101
HICF-0.5	87.45	2.14	10.41	2.91	0.0085

X-ray photoelectron spectroscopy (XPS) was conducted to investigate the chemical state and element composition. Figure 4.3a shows the XPS survey scan spectrum of HICF-1, demonstrating the existence of carbon (C), oxygen (O), and nitrogen (N) elements in the sample. Figure 4.3b displays the high-resolution C 1s spectrum of HICF-1, which confirms the signals of C=O (289.1 eV), C-O (286.8 eV), C-N (285.2 eV), and C-C (284.5 eV) bonds.[27, 28] As to the O 1s spectrum, Figure 4.3c displays the corresponding fitting peaks representing C-O (532.9 eV) and C=O (531.3 eV) bonds.[29] The N 1s spectrum could be deconvoluted into graphitic N at 401.5 eV, pyrrolic N at 400.7 eV, and pyridinic N at 398.5 eV in Figure 4.3d.[30] The graphitic nitrogen atoms are able to introduce extra free electrons and thereby increase the conductivity, while the latter two are favorable for the adsorption of the supernumerary atoms, thus increasing the number of the sodium storage points.[31] Besides, the XPS analysis in Table 4.2 demonstrates that the content of the heteroatoms (N and O) is gradually reduced from 12.55 at% for HICF-0.5 to 11.46 at% for HICF-1 to 10.32 at% for HICF-2, which achieves the enrichment of C element with increasing pyrolysis time.

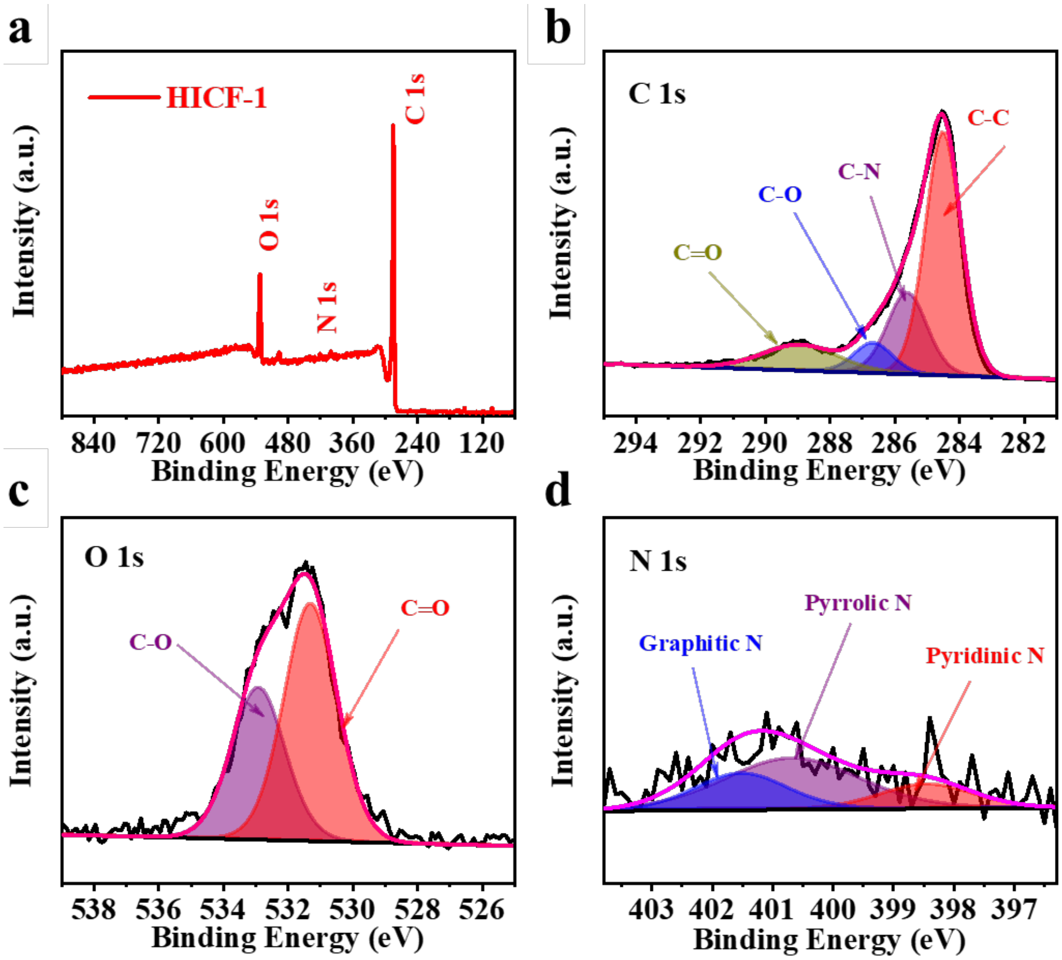

Figure 4.3 (a) XPS survey spectrum and the corresponding high-resolution XPS analysis of (b) C 1s, (c) O 1s, and (d) N 1s of HICF-1.

To investigate the Na storage performance of the three HICFs, CR2032 half coin cells were assembled using the self-supported freestanding HICFs as the working electrodes and 1 M $NaCF_3SO_3$ in diglyme as the ether-based electrolyte. Figure 4.4a shows the cyclic voltammetry (CV) curves of HICF-1 anode for the initial three cycles at the scan rate of 0.1 mV s^{-1} between 0.01 and 2.9 V. In the first cathodic scan, two major peaks appeared.

The broad peak at about 0.5 V could be attributed to Na-ion absorption in the highly disordered carbon phase as well as other defects including nanopores and heteroatoms, which shifts to ~0.7 V in the subsequent scans.[20] The sharp peak between 0 and 0.1 V corresponds to Na^+ intercalation into the interlayers of pseudo-graphitic phase.[8, 32] Additionally, the CV curves of HICF-0.5 and HICF-2 (Figure 4.5a, b) exhibit similar characteristics to that of HICF-1.

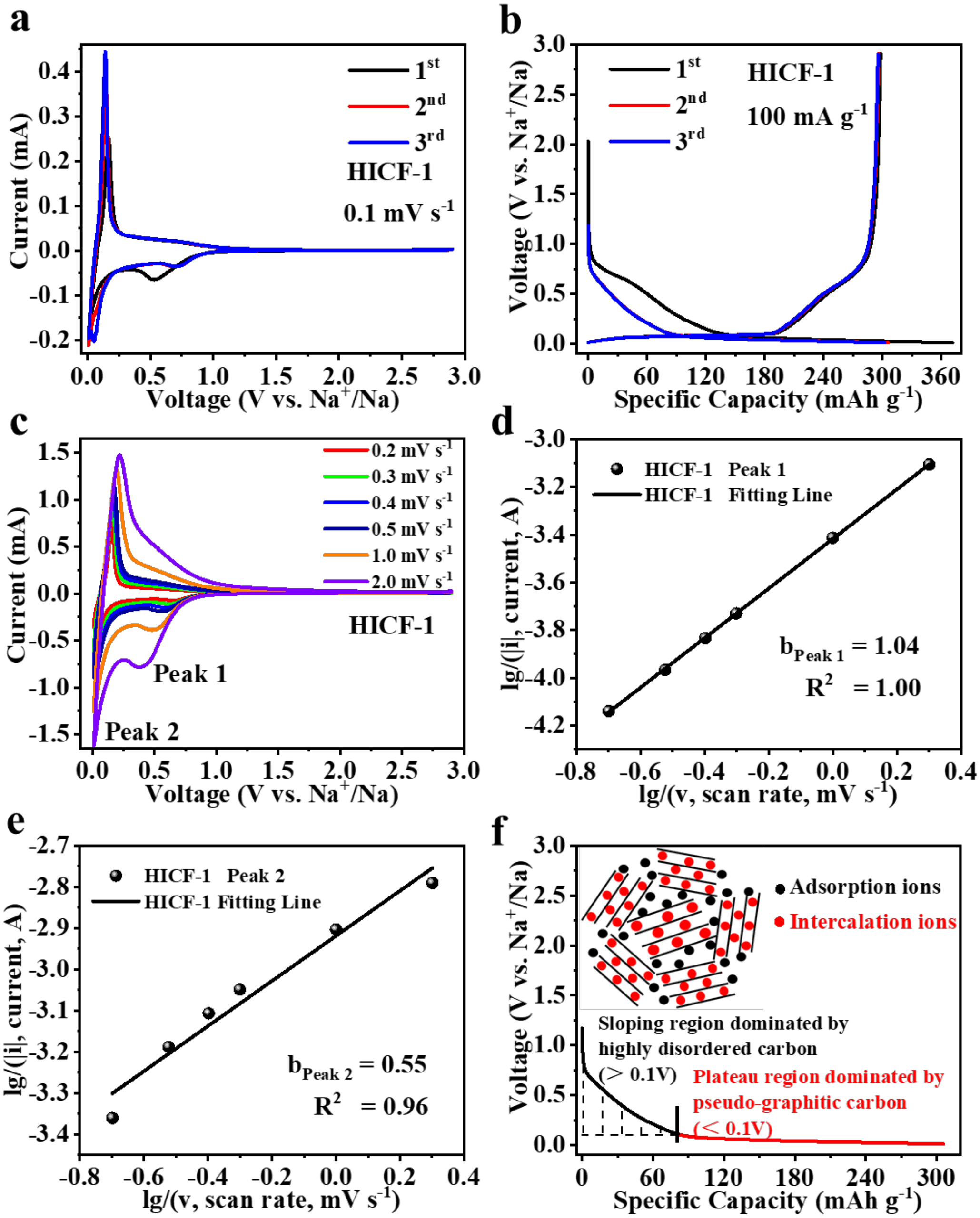

Figure 4.4 (a) CV curves of HICF-1 at the scan rate of 0.1 mV s^{-1} between 0.01 and 2.9 V; (b) Galvanostatic charge/discharge profiles of HICF-1 at 100 mA g^{-1}; (c) CV curves of HICF-1 at different scan rates from 0.2 to 2.0 mV s^{-1}; The correlation of current with different scan rates for (d) Peak 1 and (e) Peak 2 of HICF-1; (f) The schematic diagram of sodium-storage mechanism in the HICFs.

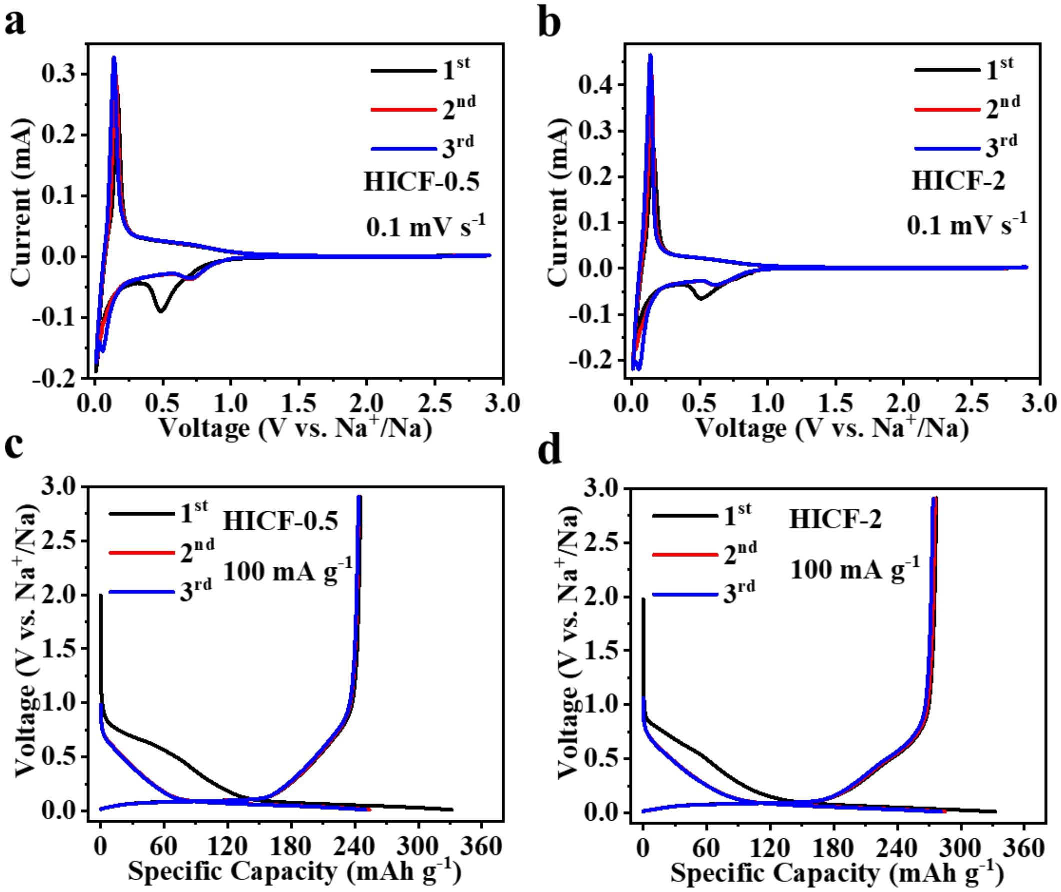

Figure 4.5 CV curves of (a) HICF-0.5 and (b) HICF-2 between 0.01 and 2.9 V at the scan rate of 0.1 mV s^{-1}; Galvanostatic charge/discharge profiles of (c) HICF-0.5 and (d) HICF-2 for the initial three cycles at 100 mA g^{-1}.

Figure 4.4b displays the discharge/charge profiles of HICF-1 for the initial three cycles at 100 mA g^{-1}. The short sloping region (>0.1 V) and the long plateau region (< 0.1 V) correspond to the two reduction peaks at ~0.7 and 0-0.1 V in the CV curves (Figure 4.4a), respectively. The initial discharge and charge capacities are 371.4 and 298.0 mAh g^{-1}, respectively, leading to a high initial Coulombic efficiency of 80.2%. In addition, HICF-1 delivers a much higher reversible capacity of 305.7 mAh g^{-1} (the second cycle) than those of HICF-0.5 (245.6 mAh g^{-1}) and HICF-2 (276.9 mAh g^{-1}) in Figure 4.5c, d. It can be easily noted that the capacity contributed by the plateau was much larger than that contributed by the slope. Moreover, the plateau capacity contribution of HICF-1 (221.7 mAh g^{-1}) is also the largest among the three HICFs, which should originate from the largest content of pseudo-graphitic phase (63.24%) in HICF-1 compared to those of HICF-0.5 (55.29%) and HICF-2 (61.29%) listed in Table 4.1.

Kinetic analysis was then performed to elucidate the Na-ion storage mechanism of HICF-1 based on the CV tests at a variety of scan rates from 0.2 to 2.0 mV s^{-1}, shown in Figure 4.4c. The obtained scan rate (v) and peak current (i) could be described by the following equations:

$$i = a\, v^{b} \qquad (1)$$

$$lg\ |i| = b \times lg\ v + lg\ a \qquad (2)$$

where b and a are constants. Particularly, the b value has a close connection with the kinetics for the sodium ion storage. If the constant b is equal to 0.5, the electrochemical process is diffusion-controlled, like sodium ion insertion/extraction between the interlayer zone, while the b value close to 1.0 means the surface-controlled process like surface adsorption.[33] Here, two cathodic peaks are selected to analyze the kinetics: one is the broad peak at ~0.7 V (Peak 1) standing for the slope region in the discharge/charge curves, the other is the sharp peak between 0 and 0.1 V (Peak 2) corresponding to the plateau region. The fitted results based on equation (2) show a good linear relationship between $lg\ v$ and $lg\ |i|$ in Figure 4.4d, e. The fitted b-value for Peak 1 is 1.04, suggesting a non-diffusion limited process of the sloping capacity, which agree well with the fast adsorption process at the surface active sites provided by the highly disordered carbon phase. As to Peak 2, the fitted b-value is 0.55, revealing that the plateau zone is a diffusion-controlled process, which supports the slow sodium intercalation process into the pseudo-graphitic phase.[8] The kinetic analysis of HICF-0.5 and HICF-2 based on CV curves shows the similar results. The sodium ion adsorption-intercalation mechanism in the HICFs is schematically illustrated in Figure 4.4f, which accords well with the previously reported ones.[15, 34, 35]

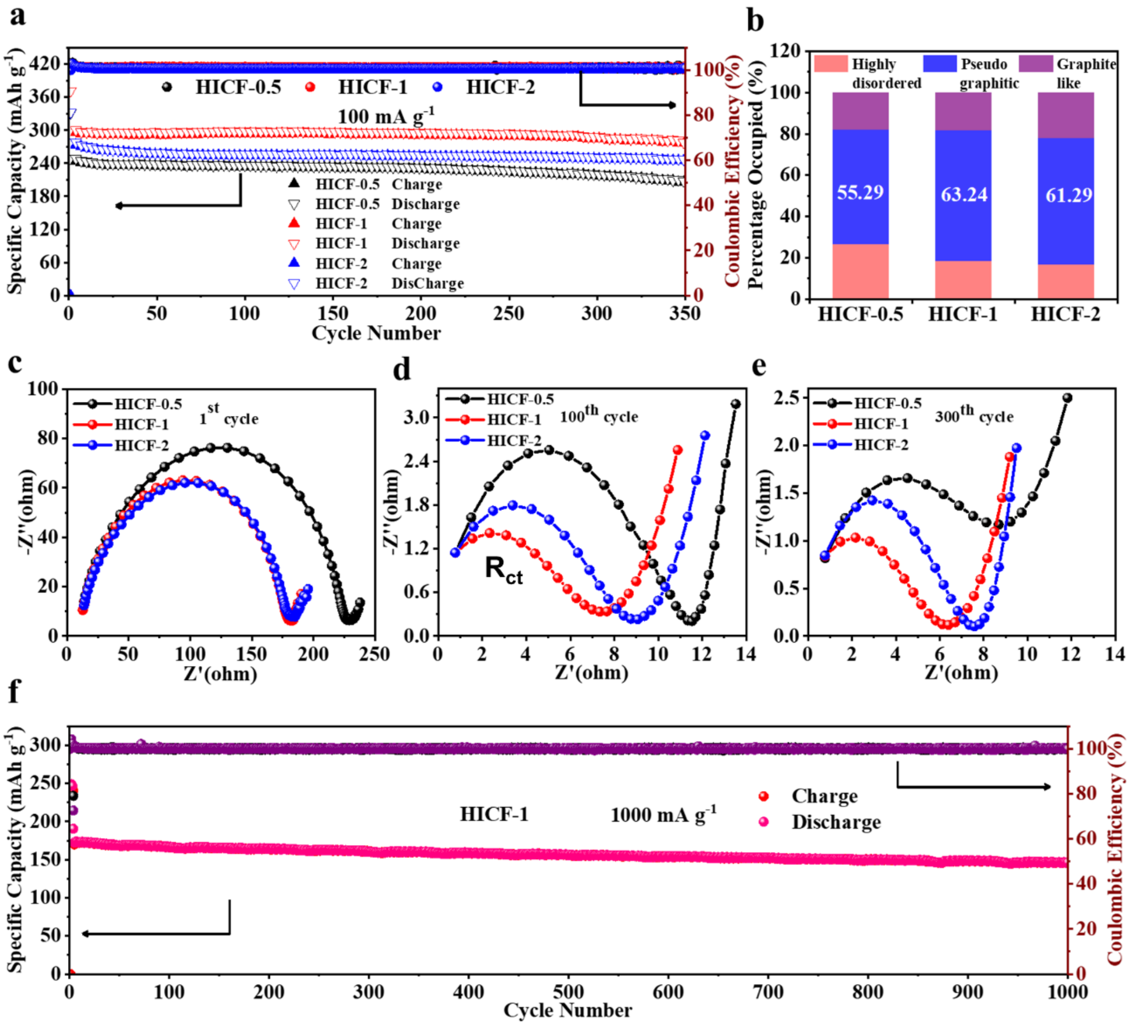

Figure 4.6 (a) Cycling performance of the HICF electrodes at 100 mA g^{-1}; (b) The percentage of pseudo-graphitic phase in the HICF samples; Nyquist plots of the HICF electrodes at fully discharged state at (c)1st, (d) 100th, and (e) 300th cycles; (f) Cycling performance of the HICF-1 electrode at 1000 mA g^{-1}.

The cycling stabilities of the three HICF samples are compared at 100 mA g^{-1} (Figure 4.6a), in which HICF-1 exhibits the best cycling performance, retaining a high reversible capacity of 281.1 mAh g^{-1} over 350 cycles, corresponding to the highest capacity retention of 92.0% with respect to second-cycle capacity. On the contrary, the capacities of HICF-0.5 and HICF-2 drop to 207.3 and 247.1 mAh g^{-1} with a capacity retention of 81.4% and 86.8%, respectively. The excellent cycling stability of HICF-1 benefits from the combination of interconnected network structure and hollow feature. The strong mechanical stability from the network and additional inner space from the hollow structure can effectively accommodate the structural deformation from Na^+ insertion/extraction. Moreover, the differences in microstructures of the three HICFs affect the cycling performance. As shown in Figure 4.6b, the microcrystalline evolution of HICFs proceeds from disordered structure to pseudo-graphitic state and graphite-like carbon along with the prolonged pyrolysis holding time as stated before. HICF-0.5 with the highest percentage of highly disordered phase (26.54%) delivers the worst cycling performance and the lowest capacity, while HICF-1 with the highest percentage of pseudo-graphitic phase (63.24%) exhibits the best cycling stability and the largest capacity, indicating that the pseudo-graphitic phase can not only store more Na ions, but also maintain more stable microstructure than the highly disordered phase.

The electrochemical impedance spectroscopy (EIS) tests were conducted at different cycles (Figure 4.6c-e) to investigate the charge-transfer resistance (R_{ct}), which is represented by the diameter of approximate semicircle in the high-frequency zone of Nyquist plots.[36] Among the three HICF electrodes, the R_{ct} of HICF-1 kept smallest from 1st cycle to 300th cycle, which could definitely prevent capacity loss and explain the superior cycling performance. The largest R_{ct} in HICF-0.5 should be induced by the largest content of highly disordered carbon phase, which usually shows much lower electrical conductivity, compared with the other pseudo-graphitic and graphite-like states. Besides, the larger R_{ct} in HICF-2 could be attributed to the relatively smaller d-spacing in the pseudo-graphitic phase, causing more resistance on Na-ion intercalation. In addition, the long-term cycling performance of the HICF-1 at 1000 mA g^{-1} was evaluated in Figure 4.6f. After activation of three cycles at 100 mA g^{-1}, HICF-1 displays a discharge capacity of 147.0 mAh g^{-1} at 1000 mA g^{-1} even over 1000 cycles with a very high capacity retention of 86.4%, which further shows an outstanding ultralong cycling stability.

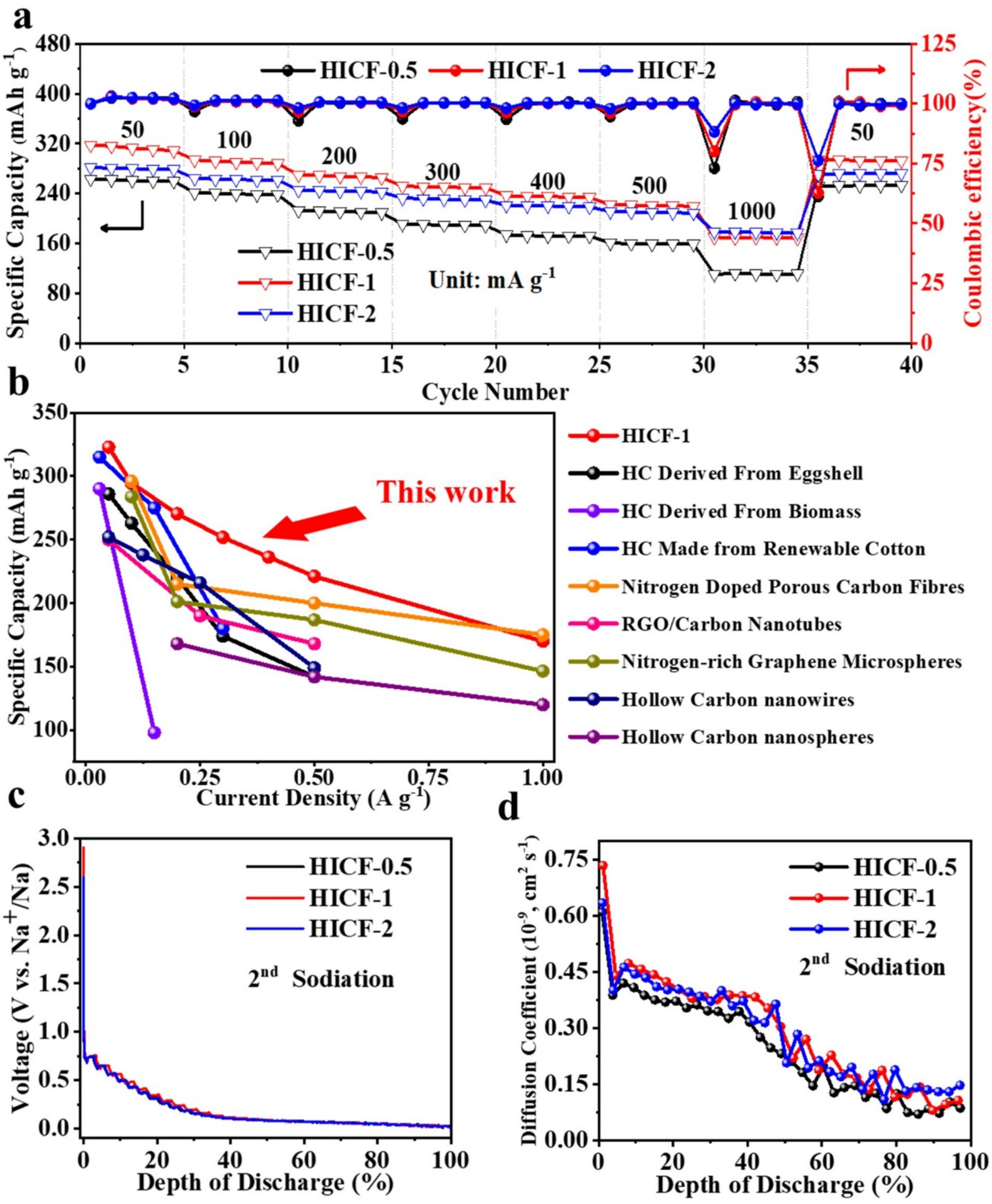

Figure 4.7 (a) Rate capabilities of the HICF electrodes at enhanced current densities from 50 to 1000 mA g^{-1}; (b) The comparison of the rate performance of HICF-1 with those of previously reported carbon-based materials for SIBs; (c) GITT profiles of the HICF electrodes for sodiation process during the second cycle; (d) Na-ion apparent diffusion coefficients of the HICF electrodes for discharge process of the second cycle from GITT.

The rate performance of the HICF electrodes were measured at different rates from 50 to 1000 mA g^{-1} shown in Figure 4.7a. The capacities of HICF-1 at 50, 100, 200, 300, 400, and 500 mA g^{-1} are 319.0, 292.9, 268.6, 251.4, 235.5, and 220.8 mAh g^{-1}, respectively. Even a large capacity of 170.1 mAh g^{-1} could still be maintained when the current increases to 1000 mA g^{-1}. HICF-1 also displays excellent structural stability against high current rates, as a reversible capacity of 297.5 mAh g^{-1} is recovered after the current density is switched to 50 mA g^{-1} again. On the contrary, HICF-0.5 performs worse as the capacities at 50, 100, 200, 300, 400, 500 and 1000 mA g^{-1} are 266.8, 241.5, 212.1, 190.3, 173.1, 159.6, and 110.6 mAh g^{-1}, respectively, which might be attributed to poorer conductivity resulting from the largest number of highly disordered phase in HICF-0.5. In addition, Figure 4.7b compares the rate capability of HICF-1 with some previously reported typical carbon-based materials for SIBs.[10, 20, 37-42] The excellent rate performance of HICF-1 should originate from fast Na-ion and electron transport provided by the interconnected channels of highly conductive carbon network and the further reduced Na-ion diffusion distance from hollow structure.

The galvanostatic intermittent titration technique (GITT) was employed to monitor the variation of sodium ion diffusion coefficient ($D_{\mathrm{Na+}}$) in the three HICFs during the second-cycle discharge process and the corresponding GITT profiles are shown in Figure 4.7c. The $D_{\mathrm{Na+}}$ is calculated according to the Fick's second law as follows:[5, 43]

$$D = \frac{4}{\pi\tau}\left(\frac{\Delta E_s}{\Delta E_t}\right)^2\left(\frac{V_m m_B}{M_B S}\right)^2 \qquad (3)$$

where τ is the pulse duration, ΔE_{s} is the steady-state voltage change caused by the current pulse, ΔE_{t} is the voltage change during the constant current pulse after eliminating the iR drop, V_{m}, M_{B} and m_{B} are the molar volume, molar mass and mass of HICFs, respectively, and S is the surface area of HICFs. Figure 4.7d show the $D_{\mathrm{Na+}}$ variation of the three HICF electrodes during the sodiation process of the second cycle. The $D_{\mathrm{Na+}}$ of HICFs gradually decrease with the sodiation proceeding, suggesting slower Na-ion transport of the plateau than that of the sloping region. This trend accords well with the adsorption-intercalation mechanism, as Na ions spread quickly in the highly disordered carbon phase due to the surface adsorption and then slowly insert into the pseudo-graphitic phase. Besides, it is worth noting that HICF-1 and HICF-2 show larger D_{Na+} than HICF-0.5, as the largest content of highly disordered carbon in HICF-0.5 leads to lowest electrical conductivity and definitely slows down the Na^+ transport, which is in line with the observed difference in rate performance.

4.3 Conclusion

In summary, the HICF was developed by one-step pyrolysis of a commercial and low-cost melamine sponge. The integration of interconnected network structure and hollow feature can not only enable strong mechanical stability and extra inner space to effectively accommodate the structural deformation from Na^+ insertion/extraction, but also achieve fast sodium-ion and electron transport. As a self-supported anode for SIBs, HICF-1 delivered a large reversible capacity (305.7 mAh g^{-1} at 100 mA g^{-1}) with a high initial Coulombic efficiency of 80.2%, an ultralong cycle life (86.4% capacity retention after 1000 cycles at 1000 mA g^{-1}), as well as superior rate performance (170.1 mAh g^{-1} at 1000 mA g^{-1}). The excellent Na-storage performance is also contributed by the maximum content (63.24%) of pseudo-graphitic phase (d_{002}-spacing between 0.36 and 0.40 nm) in HICF-1 realized by tuning pyrolysis holding time, because the pseudo-graphitic phase could store more sodium ions and maintain more stable microstructure owing to its appropriate *d*-spacing than highly disordered phase (d_{002}-spacing above 0.40 nm). Furthermore, kinetic analysis based on CV and GITT verified the adsorption-intercalation mechanism, in which highly disordered carbon phase absorbs Na ions fast in the sloping region and then Na ions intercalate into the pseudo-graphitic phase in the plateau region. This work provides a very promising anode candidate for the future commercialization of low-cost SIBs.

References

[1] C. H. Yang, J. W. Xiong, X. Ou, C. F. Wu, X. H. Xiong, J. H. Wang, K. Huang, M. L. Liu, *Mater. Today Energy* **2018**, 8, 37-44.

[2] J. T. Xu, M. Wang, N. P. Wickramaratne, M. Jaroniec, S. X. Dou, L. M. Dai, *Adv.*

Mater. **2015**, 27, 2042-2048.

[3] D. Saurel, B. Orayech, B. W. Xiao, D. Carriazo, X. L. Li, T. Rojo, *Adv. Energy Mater.* **2018**, 8, 1703268.

[4] C. L. Zhao, Y. X. Lu, Y. M. Li, L. W. Jiang, X. H. Rong, Y. S. Hu, H. Li, L. Q. Chen, *Small Methods* **2017**, 1, 1600063.

[5] F. Xie, Z. Xu, A. C. S. Jensen, H. Au, Y. X. Lu, V. Araullo-Peters, A. J. Drew, Y. S. Hu, M. M. Titirici, *Adv. Funct. Mater.* **2019**, 29, 1901072.

[6] C. Wu, S. X. Dou, Y. Yu, *Small* **2018**, 14, 1703671.

[7] A. Beda, C. Villevieille, P. L. Taberna, P. Simon, C. M. Ghimbeu, *J. Mater. Chem. A* **2020**, 8, 5558-5571.

[8] N. Sun, Z. R. X. Guan, Y. W. Liu, Y. L. Cao, Q. Z. Zhu, H. Liu, Z. X. Wang, P. Zhang, B. Xu, *Adv. Energy Mater.* **2019**, 9, 1901351.

[9] G. Q. Zou, H. S. Hou, P. Ge, Z. D. Huang, G. G. Zhao, D. L. Yin, X. B. Ji, *Small* **2018**, 14, 1702648.

[10] Y. M. Li, Y. S. Hu, M. M. Titirici, L. Q. Chen, X. J. Huang, *Adv. Energy Mater.* **2016**, 6, 1600659.

[11] X. B. Wang, Y. J. Zhang, C. Y. Zhi, X. Wang, D. M. Tang, Y. B. Xu, Q. H. Weng, X. F. Jiang, M. Mitome, D. Golberg, Y. Bando, *Nat. Commun.* **2013**, 4, 2905.

[12] G. Li, J. H. Sun, W. P. Hou, S. D. Jiang, Y. Huang, J. X. Geng, *Nat. Commun.* **2016**, 7, 10601.

[13] L. Liu, Y. X. Yin, J. Y. Li, N. W. Li, X. X. Zeng, H. Ye, Y. G. Guo, L. J. Wan, *Joule* **2017**, 1, 563-575.

[14] D. S. Bin, X. J. Lin, Y. G. Sun, Y. S. Xu, K. Zhang, A. M. Cao, L. J. Wan, *J. Am. Chem. Soc.* **2018**, 140, 7127-7134.

[15] B. H. Hou, Y. Y. Wang, Q. L. Ning, W. H. Li, X. T. Xi, X. Yang, H. J. Liang, X. Feng, X. L. Wu, *Adv. Mater.* **2019**, 31, 1903125.

[16] R. W. Mo, D. Rooney, K. N. Sun, H. Y. Yang, *Nat. Commun.* **2017**, 8, 13949.

[17] C. F. Dong, J. W. Liang, Y. Y. He, C. C. Li, X. X. Chen, L. J. Guo, F. Tian, Y. T. Qian, L. Q. Xu, *ACS Nano* **2018**, 12, 8277-8287.

[18] Y. H. Zhang, C. X. Lv, X. Wang, S. Chen, D. H. Li, Z. Peng, D. J. Yang, *ACS Appl. Mater. Interfaces* **2018**, 10, 40531-40539.

[19] M. Xu, Q. T. Xia, J. L. Yue, X. H. Zhu, Q. B. Guo, J. W. Zhu, H. Xia, *Adv. Funct. Mater.* **2019**, 29, 1807377.

[20] Y. L. Cao, L. F. Xiao, M. L. Sushko, W. Wang, B. Schwenzer, J. Xiao, Z. M. Nie, L. V. Saraf, Z. G. Yang, J. Liu, *Nano Lett.* **2012**, 12, 3783-3787.

[21] G. Wang, M. Shao, H. R. Ding, Y. Qi, J. B. Lian, S. Li, J. X. Qiu, H. M. Li, F. W. Huo, *Angew. Chem.-Int. Edit.* **2019**, 58, 13584-13589.

[22] E. M. Lotfabad, J. Ding, K. Cui, A. Kohandehghan, W. P. Kalisvaart, M. Hazelton, D. Mitlin, *ACS Nano* **2014**, 8, 7115-7129.

[23] Y. M. Li, L. Q. Mu, Y. S. Hu, H. Li, L. Q. Chen, X. J. Huang, *Energy Storage Mater.* **2016**, 2, 139-145.

[24] B. Cao, H. Liu, B. Xu, Y. F. Lei, X. H. Chen, H. H. Song, *J. Mater. Chem. A* **2016**, 4, 6472-6478.

[25] J. L. Liu, J. Wang, Z. L. Ku, H. H. Wang, S. Chen, L. L. Zhang, J. Y. Lin, Z. X. Shen, *ACS Nano* **2016**, 10, 1007-1016.

[26] Y. M. Li, Y. S. Hu, X. G. Qi, X. H. Rong, H. Li, X. J. Huang, L. Q. Chen, *Energy Storage Mater.* **2016**, 5, 191-197.

[27] H. P. Cong, X. C. Ren, P. Wang, S. H. Yu, *Energy Environ. Sci.* **2013**, 6, 1185-1191.

[28] R. Hao, Y. Yang, H. Wang, B. B. Jia, G. S. Ma, D. D. Yu, L. Guo, S. H. Yang, *Nano Energy* **2018**, 45, 220-228.

[29] Y. W. He, P. X. Bai, S. Y. Gao, Y. H. Xu, *ACS Appl. Mater. Interfaces* **2018**, 10, 41380-41388.

[30] Z. Ling, C. Yu, X. M. Fan, S. H. Liu, J. Yang, M. D. Zhang, G. Wang, N. Xiao, J. S. Qiu, *Nanotechnology* **2015**, 26, 374003.

[31] S. F. Huang, Z. P. Li, B. Wang, J. J. Zhang, Z. Q. Peng, R. J. Qi, J. Wang, Y. F. Zhao, *Adv. Funct. Mater.* **2018**, 28, 1706294.

[32] J. Ding, H. L. Wang, Z. Li, A. Kohandehghan, K. Cui, Z. W. Xu, B. Zahiri, X. H. Tan, E. M. Lotfabad, B. C. Olsen, D. Mitlin, *ACS Nano* **2013**, 7, 11004-11015.

[33] J. L. Liu, J. Wang, C. H. Xu, H. Jiang, C. Z. Li, L. L. Zhang, J. Y. Lin, Z. X. Shen, *Adv. Sci.* **2018**, 5, 1700322.

[34] S. Qiu, L. F. Xiao, M. L. Sushko, K. S. Han, Y. Y. Shao, M. Y. Yan, X. M. Liang, L. Q. Mai, J. W. Feng, Y. L. Cao, X. P. Ai, H. X. Yang, J. Liu, *Adv. Energy Mater.* **2017**,

7, 1700403.

[35] H. Y. Lu, F. X. Ai, Y. L. Jia, C. Y. Tang, X. H. Zhang, Y. H. Huang, H. X. Yang, Y. L. Cao, *Small* **2018**, 14, 1802694.

[36] J. Wang, J. L. Liu, D. L. Chao, J. X. Yan, J. Y. Lin, Z. X. Shen, *Adv. Mater.* **2014**, 26, 7162-7169.

[37] X. Zhao, Y. Ding, Q. Xu, X. Yu, Y. Liu, H. Shen, *Adv. Energy Mater.* **2019**, 9, 1803648.

[38] Y. M. Li, S. Y. Xu, X. Y. Wu, J. Z. Yu, Y. S. Wang, Y. S. Hu, H. Li, L. Q. Chen, X. J. Huang, *J. Mater. Chem. A* **2015**, 3, 71-77.

[39] L. J. Fu, K. Tang, K. P. Song, P. A. van Aken, Y. Yu, J. Maier, *Nanoscale* **2014**, 6, 1384-1389.

[40] X. Y. Yue, N. Huang, Z. Q. Jiang, X. N. Tian, Z. D. Wang, X. G. Hao, Z. J. Jiang, *Carbon* **2018**, 130, 574-583.

[41] K. Tang, L. J. Fu, R. J. White, L. H. Yu, M. M. Titirici, M. Antonietti, J. Maier, *Adv. Energy Mater.* **2012**, 2, 873-877.

[42] J. M. Feng, L. Dong, X. F. Li, D. J. Li, P. Y. Lu, F. Hou, J. Liang, S. X. Dou, *Electrochim. Acta* **2019**, 302, 65-70.

[43] L. Liu, Y. Chen, Y. H. Xie, P. Tao, Z. J. Wang, Q. Y. Li, K. X. Wang, C. L. Yan, *Small* **2019**, 15, 1804158.

Chapter 5

Cobalt Sulfide Nanoflakes Grown on Graphite Foam for Na-Ion Batteries with Ultrahigh Initial Coulombic Efficiency

Sodium-ion batteries (SIBs) are regarded as promising low-cost alternatives to the prevailing lithium-ion batteries. However, most anode materials for SIBs suffer from low initial Coulombic efficiency (ICE), limiting their commercial applications. Herein, we demonstrate a Na-ion anode with an extremely high ICE of 99.4%, based on cobalt sulfide (Co_9S_8*/CoS) nanoflakes grown on graphite foam (GF) in diglyme-based electrolyte. The achievement of such a high ICE can be ascribed to the following three aspects: i) negligible side reactions between diglyme-based electrolyte and* Co_9S_8*/CoS, owing to much higher Fermi level of diglyme reduction than anode potential* μ_A *of* Co_9S_8*/CoS, which can block electron transfer from anode to electrolyte, ii) highly reversible conversion reaction of* Co_9S_8*/CoS, and iii) much lower initial capacity loss of substrate GF, compared with other sorts of carbon. The underlying rules revealed in this study serve as general guidelines in the development of sodium-ion anodes to achieve superb ICE.*

---

*This section published substantially as H.S. Wang, J.L. Liu, H.H. Wang, X.Y. Cai, X.L. Ye, L.L. Zhang, Z. Chen, and Z.X. Shen. Cobalt Sulfide Nanoflakes Grown on Graphite Foam for Na-Ion Batteries with Ultrahigh Initial Coulombic Efficiency. *Journal of Materials Chemistry A*, **2020**, 8, 14900-14907. DOI: 10.1039/D0TA04312E. Reprinted with permission. Copyright (2020) Royal Society of Chemistry.

5.1 Introduction

Various materials have been investigated as sodium-ion anodes, mainly including three types: insertion-type materials (for example, hard carbon and graphite), conversion-type materials (for example, transition metal sulfides and oxides) and alloying-type materials (such as tin and phosphorous).[1-3] The HICF in chapter 4 belongs to hard carbon. In order to achieve higher energy density of SIBs, the conversion-type materials have drawn increasing attention owing to their higher specific capacities than those of insertion-type, and smaller volume changes during electrochemical reactions than those of alloying-type.[4] As typical conversion-type materials, cobalt sulfides (i.e., Co_9S_8, CoS, CoS_2) have been widely investigated as Na-ion storage anodes.[5-7] However, the conversion-type anode materials suffer from low energy efficiency owing to the severe voltage decay during charge/discharge process, relative to intercalation-type anode materials.[8-10] The conversion reaction of cobalt sulfides also suffers from sluggish kinetics and severe volume expansion, causing poor rate and cycling performance, respectively.[11-13]

Improved rate capability and cycling stability of cobalt sulfide-based anodes for SIBs have been achieved through coupling various nanosized cobalt sulfides with different carbon materials.[14-16] The Na-ion diffusion length can be shortened due to nanosized cobalt sulfides and fast electron transfer can be accomplished by highly conductive carbon. Furthermore, the strain resulted from the large volume change of cobalt sulfides can be greatly accommodated by its nanostructures as well as the carbon matrix as a buffer layer.[17] Nevertheless, most of previously reported cobalt sulfide-based anode materials suffered from low initial Coulombic efficiency (ICE), which is less a problem in the case of half cells which usually supply sufficient Na ions from thick metallic Na. However, when assembling full cells, sufficiently high ICE of electrode materials is essential for obtaining high cell performance, because higher ICE can ensure lower irreversible loss of Na ions from the cathodes and lead to higher reversible capacities in full cells.[18-22] However, until now, no effective strategies have been proposed to settle the issue of low ICE for cobalt sulfide-based electrodes.

Herein, we report a strategy of growing CoS_x (Co_9S_8/CoS) nanoflakes on the substrate of graphite foam (GF) through a one-pot solvothermal route (denoted as CoS_x NF@GF hereafter). When coupled with diglyme-based electrolyte, the freestanding CoS_x NF@GF exhibited an ultrahigh ICE of 99.4%. To our knowledge, this is the highest among the previously reported Na-ion storage anodes based on cobalt sulfides. The underlying reasons were uncovered by investigating the following four aspects: electrochemical stability of electrolytes, crystal phase of cobalt sulfides, initial capacity loss of employed carbon, and morphology of cobalt sulfides, where the first three factors were revealed to play the major role in achieving such an extremely high ICE. While the morphology has little influence on the ICE, it nonetheless showed a great impact on the cycling and rate performance, predominantly by alleviating the volume expansion and enhancing the ionic and electronic kinetics in the case of CoS_x ultrathin nanoflakes on GF. Our study provides a deeper understanding of developing anode materials for SIBs with superb ICE.

5.2 Results and Discussion

5.2.1 Material Synthesis and Characterization

Figure 5.1 schematically shows the fabrication procedures of CoS_x NF@GF. In brief, the as-prepared highly conductive and flexible GF was used as the substrate to grow CoS_x (Co_9S_8/CoS) nanoflakes on its surface through a one-step solvothermal route. The crystalline structure and morphology of GF were identified via X-ray diffraction (XRD) and scanning electron microscopy (SEM), respectively, shown in Figure 5.2a, b.

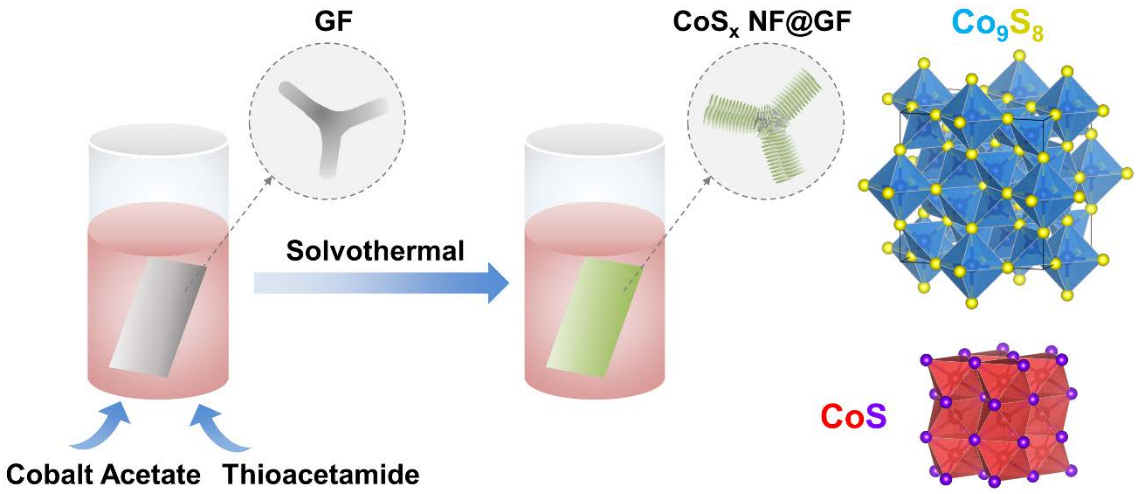

Figure 5.1 Schematic illustration for synthesis procedures of the CoS$_x$ NF@GF composite and crystal structures of Co$_9$S$_8$ and CoS.

The XRD diffraction peaks (Figure 5.2a) can be assigned to graphitic carbon (ICDD card no. 00-008-0415) without other impurity phases. In addition, the highly crystalline structure of GF was indicated by the strong and sharp XRD reflections, which suggests high conductivity of substrate GF that enhances electronic kinetics of cobalt sulfides. Figure 5.2b presents the SEM image of GF. The GF was revealed to be highly macroporous with interconnected network structure, which exhibits rather low areal density and excellent mechanical flexibility that offers sufficient buffer for the volume changes of cobalt sulfides.

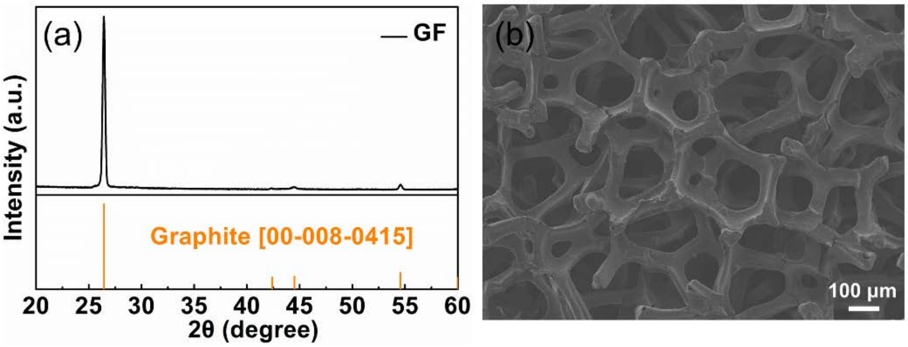

Figure 5.2 (a) XRD pattern and (b) SEM image of pure GF.

The XRD pattern of CoS_x NF@GF is displayed in Figure 5.3a, in which the diffraction peaks could be assigned to the cubic Co_9S_8 (ICDD card no. 04-004-4525) as well as the hexagonal CoS (ICDD card no. 01-075-0605), except for those peaks attributed to GF, demonstrating that the CoS_x composed of Co_9S_8 and CoS phases (the crystal structures shown in Figure 5.1) were grown on GF. In addition, the CoS/Co_9S_8 ratio was estimated to be 0.49 from the XRD pattern using the method of reference intensity ratio. The SEM images (Figure 5.3b, c) display the typical nanoflakes array morphology with a thickness of ~15 nm of CoS_x NF@GF uniformly and vertically aligned on the entire surface of GF. Additionally, the homogenous elemental distribution of Co, S and C within the sample was validated by the energy-dispersive X-ray spectroscopy (EDS) elemental mappings (Figure 5.3d-f) of the corresponding region shown in Figure 5.3c.

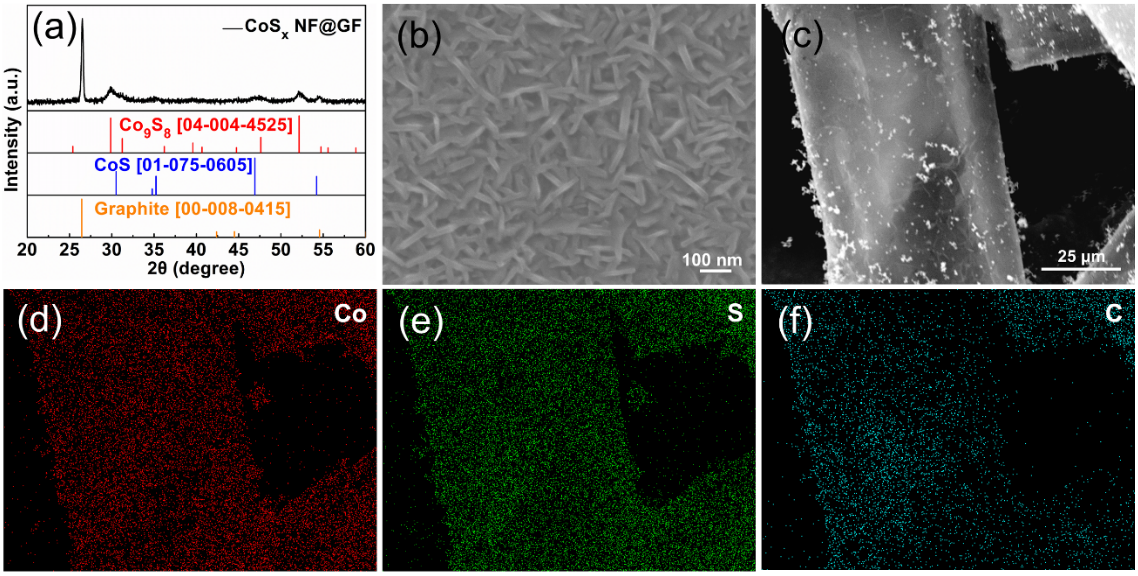

Figure 5.3 (a) XRD pattern, (b, c) SEM images, (d-f) EDS mappings of Co, S and C elements of the CoS_x NF@GF composite.

The chemical and electronic state of CoS_x NF@GF was analyzed by X-ray photoelectron spectroscopy (XPS). The XPS survey scan spectrum displayed in Figure 5.4a corroborates the existence of Co, S, C, and O four elements in the CoS_x NF@GF composite. The Co 2p core-level XPS spectrum is shown in Figure 5.4b, in which two peaks for Co-S bonds (Co 2p$_{3/2}$ and Co 2p$_{1/2}$) in cobalt sulfides are observed at 778.8 and 793.9 eV, respectively, with the energy separation of 15.1 eV.[23] Additionally, two corresponding satellite peaks at 781.2 and 797.1 eV can be observed. Another two peaks at 785.6 and 802.6 eV are ascribed to Co-O bonds, because oxygen in the air is easily absorbed on cobalt ions due to their strong affinity.[12, 13, 24] Three types of S components were identified in the high-resolution S 2p spectrum (Figure 5.4c). Two characteristic peaks at 161.9 and 163.1 eV correspond to S 2p$_{3/2}$ and S 2p$_{1/2}$ of cobalt sulfides (Co-S bonds), respectively, with the energy separation of 1.2 eV.[23] Another two characteristic peaks located at 164.8 and 166 eV could be attributed to C-S 2p$_{3/2}$ and 2p$_{1/2}$. Additionally, the remaining two peaks for S-O bonds are located at 167.6 and 168.8 eV, probably due to the oxidation of air. The C 1s core-level XPS spectrum (Figure 5.4d) confirms the presence of C-C, C-S, and C=O bonds with the corresponding peaks centred at 284.6, 286.0 and 288.2 eV, respectively, indicating that S and O-containing groups existed on the surface of GF.[12]

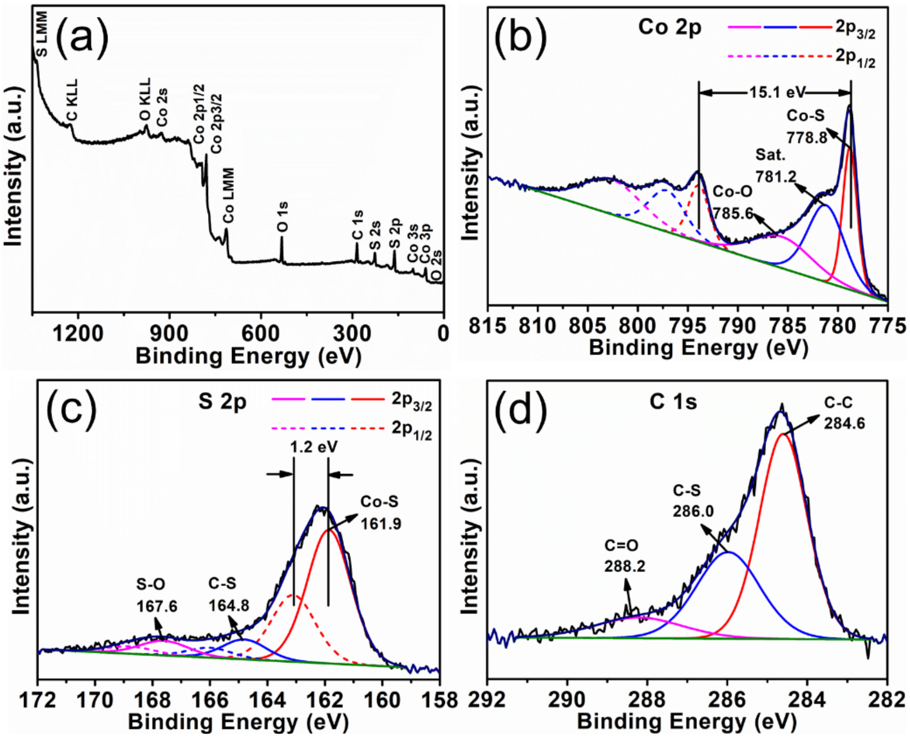

Figure 5.4 (a) XPS survey scan spectrum, (b) Co 2p, (c) S 2p, and (d) C 1s core-level spectra of CoS$_x$ NF@GF.

5.2.2 Initial Coulombic Efficiency

To evaluate the Na-ion storage performance of CoS_x NF@GF, CR2032 half coin cells were assembled with freestanding CoS_x NF@GF as the working electrode and 1 M $NaCF_3SO_3$ in diglyme as the ether-based electrolyte.[25] The discharge/charge profiles of CoS_x NF@GF in diglyme-based electrolyte for the initial three cycles at a current density of 0.5 A g^{-1} between 0.4 and 2.9 V are shown in Figure 5.5a. The long discharge plateau located at ~0.9 V and the long charge plateau observed at ~1.7 V correspond to the conversion reaction of Co_9S_8/CoS.[12, 13] Additionally, another pair of short plateaus at around 0.6 V (discharging) and 0.7 V (charging) was evidenced, which can be ascribed to the co-intercalation reaction of GF.[26-28] CoS_x NF@GF delivers high initial specific discharge and charge capacities of 577.3 and 573.6 mAh g^{-1}, respectively, calculated using the mass of CoS_x, leading to the highest ICE of 99.4% among the reported cobalt sulfide-based Na-ion anodes. When assembling full cells, the sufficiently high ICE of anode materials is essential for obtaining superior cell performance, because higher ICE can ensure less irreversible loss of Na ions from the cathodes and result in higher reversible capacities in full cells.[18-20]

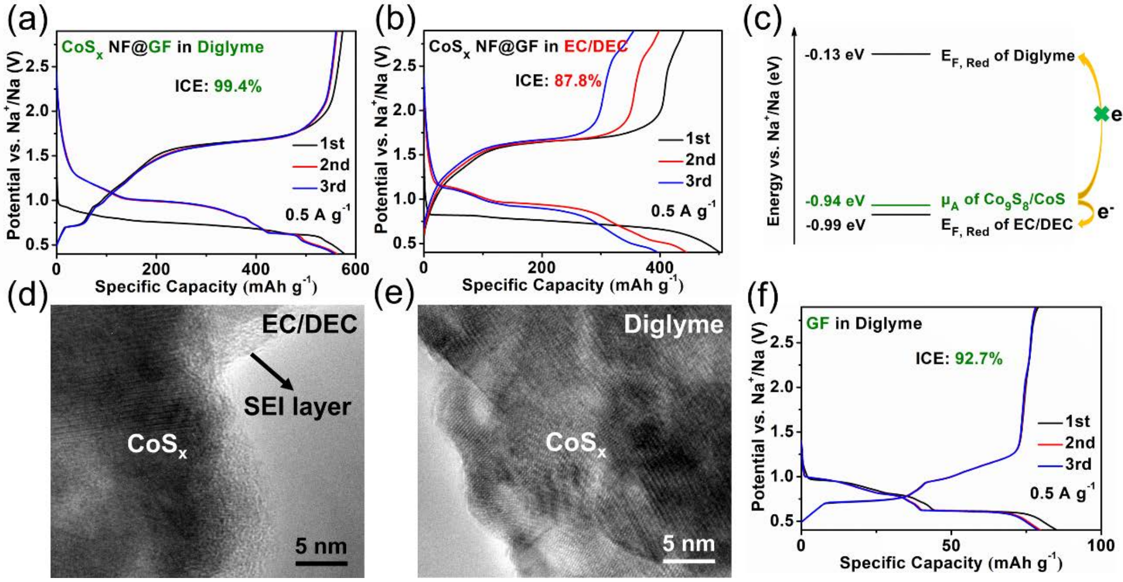

Figure 5.5 Discharge/charge profiles of CoS_x NF@GF (a) in diglyme-based electrolyte and (b) in EC/DEC-based electrolyte at 0.5 A g^{-1}. (c) Electrochemical stability of diglyme-based and EC/DEC-based electrolytes versus Co_9S_8/CoS electrode. HRTEM images of CoS_x NF@GF electrodes after one cycle (d) in EC/DEC-based electrolyte and (e) in diglyme-based electrolyte. (f) Discharge/charge profiles of pure GF in diglyme-based electrolyte at 0.5 A g^{-1}.

To find out the reasons for such a high ICE for CoS_x NF@GF associated with diglyme-based electrolyte, the impacts of electrolyte and anode material were investigated separately. Firstly, a controlled experiment employing a carbonate-based electrolyte,[29] i.e., 1 M $NaCF_3SO_3$ in ethylene carbonate (EC)/diethyl carbonate (DEC), and CoS_x NF@GF was conducted. With the EC/DEC-based electrolyte, the ICE of CoS_x NF@GF anode was only 87.8%, much lower than that in diglyme-based electrolyte, as demonstrated by the first discharge/charge curves in Figure 5.5b. Furthermore, a drastic capacity decay was observed for the second and third discharge/charge curves, indicating strong irreversible capacity loss resulting from the interactions between CoS_x and EC/DEC-based electrolyte. The underlying reasons are given in Figure 5.5c. The Fermi level of EC/DEC reduction (about -0.99 eV)[30] is lower than the reduction potential μ_A of Co_9S_8/CoS (about -0.94 eV), which means that during the initial sodiation process, electrons can transfer from Co_9S_8/CoS to EC/DEC,[31, 32] leading to electrolyte reduction on the surface of anode, therefore causing initial capacity loss and lower ICE. The solid electrolyte interphase (SEI) layers resulting from EC/DEC reduction were detected by high-resolution transmission electron microscopy (HRTEM) in Figure 5.5d. On the contrary, the Fermi level of diglyme reduction (about -0.13 eV)[30] is much higher than the anode potential μ_A of Co_9S_8/CoS (about -0.94 eV), which can block transfer of electrons from Co_9S_8/CoS to diglyme,[31] resulting in negligible side reactions of electrolyte with anode and thus higher ICE. The HRTEM image (Figure 5.5e) validates no SEI layers formed in diglyme-based electrolyte.

Furthermore, Table 5.1 lists some reported anode materials (Co_9S_8, CoS, Ni_3S_2, $Cu_{1.8}S$, ZnSe, and $Co_{0.85}Se$) with verified reversible electrochemical reactions in diglyme-based electrolytes for SIBs.[33-36] The anode potentials μ_A of these materials are all much lower than the Fermi level of diglyme reduction (about -0.13 eV), indicating that no electrons can transfer from anodes to electrolytes. Actually, after eliminating initial capacity loss from the contributions of employed carbon, all these anode materials exhibit an ICE of nearly 100%, implying negligible side reactions between these anodes and diglyme-based electrolytes. Especially, in the work of $Cu_{1.8}S$ hollow octahedra,[34] the HRTEM measurements revealed that no SEI layers existed at the $Cu_{1.8}S$ surface in diglyme-based electrolyte, but SEI layers were detected in EC/DEC-based electrolyte, originating from side reactions between EC/DEC and $Cu_{1.8}S$.

Table 5.1 ICE analysis of the reported anode materials in diglyme-based electrolytes for SIBs.

Materials	**Anode Potential μ_A (eV)**	**1st Discharge Capacity (mAh g^{-1}) / ICE (%)**	**1st Discharge Capacity / Initial Capacity Loss of Carbon (mAh g^{-1})**	**Carbon Content (wt%)**	**ICE (%) Calculated without Carbon**	**Ref.**
Co_9S_8/CoS@NSC	-0.9	696/**94.5**	276/116	51	**103.8**	[12]
CoS@rGO	-0.93	780/**89.7**	726/184	41	**99.2**	[13, 37]
(Co_9S_8 QD@HCP)@rGO	-0.9	679/**89.0**	HCP: 415/240 rGO: 375/105	HCP: 6 rGO: 35	**95.6**	[7]
Ni_3S_2@NS-CNTs	-0.9	463/**93.3**	262/43	46	**96.8**	[33]
$Cu_{1.8}S$ Hollow Octahedra	-0.76	403/**99.0**	no carbon	0	**99.0**	[34]
ZnSe NP@NHC	-0.56	311/**99.1**	no data of NHC	6.7	**>99.1**	[35]
$Co_{0.85}Se$ NSs/G	-0.95	470/**82.5**	548/368	21	**98.6**	[36]
CoS_x NF@GF	-0.94	577/**99.4**	85/6	50	**100.4**	**This work**

The sulfur-poor crystal phases of Co_9S_8 and CoS also contribute to the ultrahigh ICE of CoS_x NF@GF in diglyme-based electrolyte. The conversion reactions of Co_9S_8 and CoS were verified to be highly reversible by ex situ XRD,[12] resulting in negligible initial capacity loss and thus high ICE. From the discharge/charge curves (Figure 5.5a), it is worthwhile to mention that CoS_x NF@GF achieved high reversibility.

Another factor that contributes to the ultrahigh ICE of 99.4% of CoS_x NF@GF in diglyme-based electrolyte is rather low initial capacity loss of substrate GF, resulting from its low capacity (<80 mAh g^{-1}) and high ICE (92.7%), shown in Figure 5.5f. In contrast, other works mostly employed carbon, such as reduced graphene oxide (rGO) or hard carbon, to enhance the electrical conductivity of cobalt sulfide anodes for SIBs.[7, 12, 13] However, as Na-ion storage anodes, rGO, ordered mesoporous carbon (CMK-3) and activated carbon[37] all exhibited substantially higher initial capacity loss with lower ICE in diglyme-based electrolytes, compared with GF, listed in Table 5.2. Thereby, benefiting from the advantageous features of high ICE and low capacity contribution, the selection of GF as the substrate for CoS$_x$ plays also an important role for achieving such an extremely high ICE.

Table 5.2 Initial capacity loss of the previously reported typical carbon materials in diglyme-based electrolytes for SIBs.[37]

Carbon	**Electrolyte**	**1st Discharge Capacity (mAh g^{-1})**	**ICE (%)**	**Initial Capacity Loss (mAh g^{-1})**
rGO	1M NaCF$_3$SO$_3$ in Diglyme	~726	74.6	~184
CMK-3	1M NaCF$_3$SO$_3$ in Diglyme	~550	62.8	~205
Activated Carbon	1M NaCF$_3$SO$_3$ in Diglyme	~364	59.6	~147

In addition, to investigate the potential impact of morphology of cobalt sulfide on ICE, CoS$_x$ film was grafted on GF via a hydrothermal route, marked as CoS$_x$ Film@GF, which consists of the same phase (Co$_9$S$_8$ and CoS) as CoS$_x$ NF@GF, but shows irregular morphology, verified by Figure 5.6a, b. Figure 5.6c shows that the ICE of CoS$_x$ Film@GF in diglyme-based electrolyte was still very high (97.4%), suggesting that the morphology of cobalt sulfide has little influence on ICE.

Furthermore, to explore the potential influence of current density and potential range on ICE, the discharge/charge curves of CoS$_x$ NF@GF in diglyme-based electrolyte were measured at a low current density of 0.1 A g^{-1} in a wide potential range of 0.01-2.9V, shown in Figure 5.6d. The high ICE of 97.8% was still obtained. Additionally, the surface and structure of CoS$_x$ NF@GF electrodes in diglyme-based electrolyte after continuous five cycles were examined by HRTEM. No SEI layers were observed at the surface of electrodes (Figure 5.6e), further verifying highly stable interface between diglyme-based electrolyte and CoS_x. Moreover, most of CoS_x remained the nanoflake structure (Figure 5.6f).

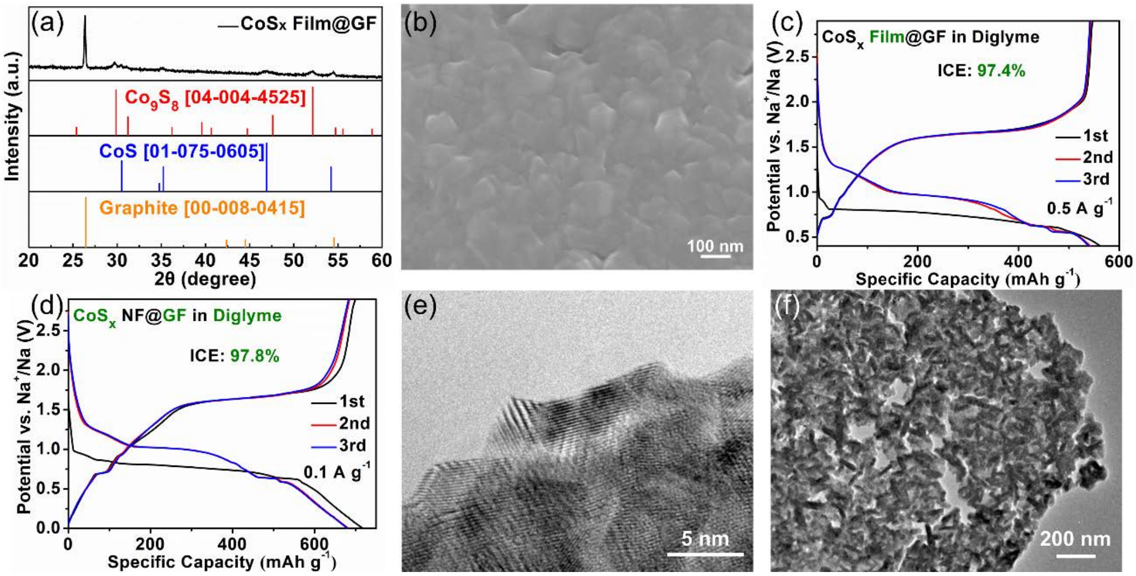

Figure 5.6 (a) XRD pattern and (b) SEM image of CoS_x Film@GF. (c) Discharge/charge profiles of CoS_x Film@GF in diglyme-based electrolyte at 0.5 A g^{-1}. (d) Discharge/charge profiles of CoS_x NF@GF in diglyme-based electrolyte at 0.1 A g^{-1} in a potential range of 0.01-2.9V. (e, f) HRTEM images of CoS_x NF@GF electrodes after five cycles in diglyme-based electrolyte.

Owing to the three aspects, including the negligible side reactions between diglyme-based electrolyte and Co_9S_8/CoS, the reversible conversion reaction of Co_9S_8/CoS, as well as the rather low initial capacity loss of substrate GF, the CoS_x NF@GF in diglyme-based electrolyte exhibited the highest ICE of 99.4% among the reported cobalt sulfide-based anodes for SIBs, listed in Table 5.3. The lower ICE in other works can be ascribed to carbonate-based electrolytes with side reactions between electrolytes and cobalt sulfides, CoS_2 with irreversible conversion reaction,[6] or employed carbon like rGO, hard carbon with high initial capacity loss.

Table 5.3 ICE of the previously reported cobalt sulfide-based anode materials for SIBs.

Materials	**Cobalt Sulfides**	**Carbon**	**Electrolytes**	**ICE (%)**	**Ref.**
CoS_2/MCNFs	CoS_2	carbonized PAN/PS	1M $NaCF_3SO_3$ in Diglyme	80.2	[5]
CoS_2-C/CNT	CoS_2	carbonized MOFs	1 M $NaPF_6$ in DME	82	[6]
(Co_9S_8 QD@HCP)@rGO	Co_9S_8	rGO, carbonized MOFs	0.5M $NaCF_3SO_3$ in Diglyme	89	[7]
CNT@CoS@C	CoS	CNT, carbonized PDA	1M $NaClO_4$ in EC/DEC with 5 wt% FEC	61	[11]
CoS_x@NSC	Co_9S_8, CoS	carbonized glucose	1M $NaCF_3SO_3$ in Diglyme	94.5	[12]
CoS@rGO	CoS	rGO	1M $NaCF_3SO_3$ in Diglyme	89.7	[13]
CoS⊂carbon NWs	CoS	carbonized glucose	1M $NaClO_4$ in PC with 5 wt% FEC	54	[14]
CoS_2-CoS-GC	CoS, CoS_2	carbonized dextrin	1M $NaClO_4$ in EC/DMC with 5 wt% FEC	68	[15]
Co_9S_8–carbon	Co_9S_8	carbonized PVP	1M $NaClO_4$ in EC/DMC with 5 wt% FEC	68.9	[16]
CoS_x NF@GF	**Co_9S_8, CoS**	**graphite foam**	**1M $NaCF_3SO_3$ in Diglyme**	**99.4**	**This work**

5.2.3 Cycling and Rate Performance

To investigate electrochemical reactions of CoS_x NF@GF in diglyme-based electrolyte, cyclic voltammetry (CV) measurements were carried out (Figure 5.7a). In the cathodic scans, the three major reduction peaks at 1.22, 0.94 and 0.52 V can be ascribed to the multi-step conversion reactions of Co_9S_8/CoS into Co and Na_2S.[12] In the anodic scans, the two major oxidation peaks at 1.69 and 2.06 V are associated with the reversible formation of Co_9S_8/CoS.[13] Besides, the two main cathodic peaks located at 0.82 and 0.61 V as well as the two main anodic peaks centred at 0.72 and 0.93 V could be attributed to the reversible co-intercalation reactions of substrate GF,[26, 27] which is consistent to the CV curves of pure GF (Figure 5.8a).

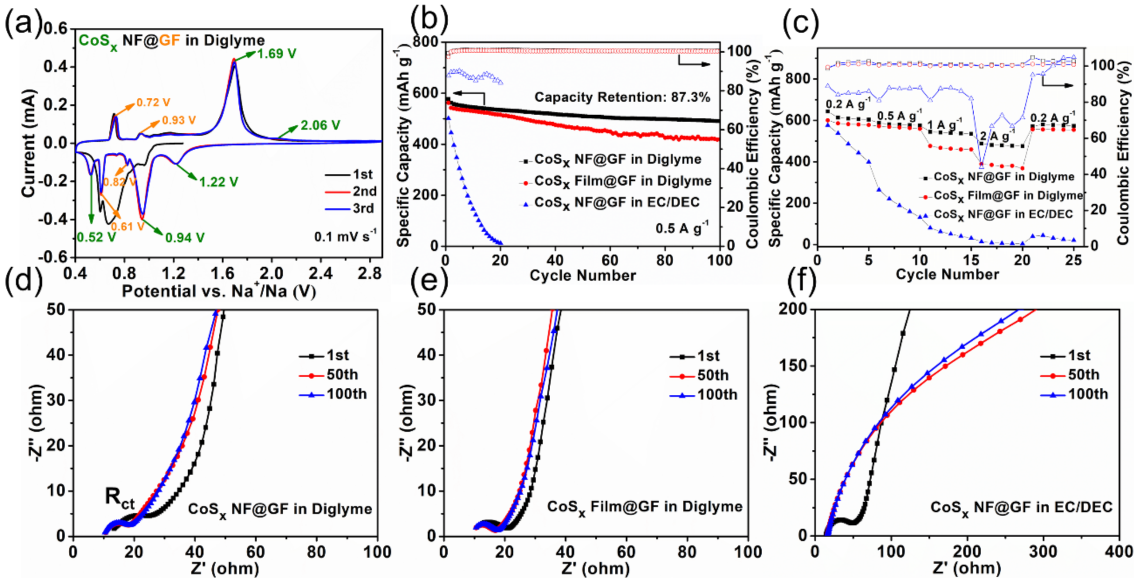

Figure 5.7 (a) CV curves of CoS_x NF@GF in diglyme-based electrolyte at a scan rate of 0.1 mV s^{-1}. (b) Cycling performance of the three combinations including CoS_x NF@GF in diglyme-based electrolyte, CoS_x Film@GF in diglyme-based electrolyte, and CoS_x NF@GF in EC/DEC-based electrolyte at 0.5 A g^{-1}. (c) Rate performance of the above three combinations at different current densities from 0.2 to 2 A g^{-1}. (d-f) EIS of the above three combinations at fully charged state after different cycles (1^{st}, 50^{th}, 100^{th}).

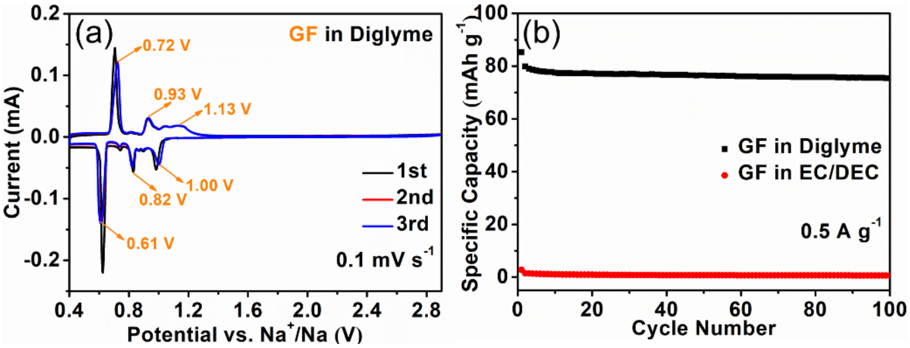

Figure 5.8 (a) CV curves of pure GF in diglyme-based electrolyte at a scan rate of 0.1 mV s^{-1}. (b) Cycling performance of GF in diglyme-based and EC/DEC-based electrolytes at 0.5 A g^{-1}.

Figure 5.7b compares the cycling performance of three combinations including CoS_x NF@GF in diglyme-based electrolyte, CoS_x Film@GF in diglyme-based electrolyte, as well as CoS_x NF@GF in EC/DEC-based electrolyte at 0.5 A g^{-1}. It is notable that CoS_x NF@GF in diglyme-based electrolyte delivered not only the highest capacity throughout the entire cycling test, compared to the other two counterparts, but also exhibited the best cycling stability, retaining a high discharge capacity of 491.0 mAh g^{-1} (87.3% of the second-cycle capacity) after 100 cycles. In comparison, the capacity retention of CoS_x Film@GF in diglyme-based electrolyte was lower, i.e., 77.2%. As for CoS_x NF@GF in EC/DEC-based electrolyte, the capacity decreased rapidly to nearly zero at the 20th cycle, an indication of strong irreversible reactions between CoS_x and EC/DEC-based electrolyte. The excellent cycling performance of CoS_x NF@GF in diglyme-based electrolyte can be ascribed to the following two aspects. One is the morphology impact that vertically aligned and ultrathin CoS_x nanoflakes could effectively relieve the strain associated with volume expansion during conversion reactions.[38] The other is the high electrode/electrolyte interfacial stability, owing to negligible side reactions between CoS_x and diglyme-based electrolyte. Additionally, the capacity contribution of GF substrate within CoS_x NF@GF was estimated,[26] shown in Figure 5.8b.

To have a clue about the capacity contribution of GF substrate within the CoS_x NF@GF anode composite, the cycling performance of pure GF in diglyme-based and EC/DEC-based electrolytes was measured at 0.5 A g^{-1} (Figure 5.8b). The capacity contribution of GF in diglyme-based electrolyte was evaluated to be ~75 mAh g^{-1}, originating from the reversible intercalation reaction of solvated sodium ions by diglyme into GF. In contrast, the capacity contribution of GF in EC/DEC-based electrolyte was almost zero, as the formation of Na-rich binary graphite intercalation compounds is thermodynamically unfavorable.

Figure 5.7c exhibits the rate performance of the above three combinations, among which CoS_x NF@GF in diglyme-based electrolyte still showed the best rate capability. In detail, the average discharge capacities were 609, 580, 539, 479 mAh g^{-1} at 0.2, 0.5, 1 and 2 A g^{-1}, respectively. Such excellent rate capability is attributed to the fast Na-ion diffusion deriving from ultrathin CoS_x nanoflakes[39] as well as the small charge-transfer resistance (R_{ct}) at the interface between CoS_x and diglyme-based electrolyte.

To monitor the R_{ct} of the above three combinations, electrochemical impedance spectroscopy (EIS) measurements were conducted after different cycles in Figure 5.7d-f. The R_{ct} can be represented by the diameter of compressed semicircle between high and medium frequency.[12, 40] As for the first cycle, the R_{ct} in diglyme-based electrolyte (Figure 5.7d, e) was substantially smaller than that in EC/DEC-based electrolyte (Figure 5.7f), corresponding to negligible side reactions between diglyme and CoS_x, but existing side reactions between EC/DEC and CoS_x. Moreover, the R_{ct} in diglyme-based electrolyte remained small during cycling, suggesting the highly stable interface between diglyme and CoS_x. In contrast, the R_{ct} in EC/DEC-based electrolyte increased dramatically upon cycling, indicating the very unstable interface between EC/DEC and CoS_x, which is in accordance with the rapid capacity loss for the corresponding cycling performance.

5.3 Conclusion

In summary, the CoS_x NF@GF composite has been developed by growing CoS_x (Co_9S_8/CoS) nanoflakes on the highly conductive and flexible substrate of GF through a one-pot solvothermal route. As a freestanding anode for SIBs, to the best of our knowledge, CoS_x NF@GF in diglyme-based electrolyte achieved the highest ICE of 99.4% among the previously reported cobalt sulfide-based Na-ion anodes. Through a systematic investigation of several factors that can potentially influence the ICE, such a high ICE could be ascribed to the following three aspects, including i) the negligible side reactions between diglyme-based electrolyte and Co_9S_8/CoS, owing to much higher Fermi level of diglyme reduction than anode potential μ_A of Co_9S_8/CoS, blocking transfer of electrons from anode to electrolyte, ii) the highly reversible conversion reaction of Co_9S_8/CoS, and iii) the rather low initial capacity loss of substrate GF. Furthermore, CoS_x NF@GF in diglyme-based electrolyte achieved excellent cycling and rate performance, primarily resulting from alleviated volume expansion and facilitated ionic and electronic kinetics ensured by ultrathin nanoflakes vertically aligned with GF, as well as negligible side reactions at the interface of electrode/electrolyte. These revealed underlying rules can be extended to develop other Na-ion storage anode materials with superb ICE.

References

[1] H. Y. Kang, Y. C. Liu, K. Z. Cao, Y. Zhao, L. F. Jiao, Y. J. Wang, H. T. Yuan, *J. Mater. Chem. A* **2015**, 3, 17899-17913.

[2] W. Luo, F. Shen, C. Bommier, H. L. Zhu, X. L. Ji, L. B. Hu, *Accounts Chem. Res.* **2016**, 49, 231-240.

[3] J. Y. Hwang, S. T. Myung, Y. K. Sun, *Chem. Soc. Rev.* **2017**, 46, 3529-3614.

[4] P. Ge, C. Y. Zhang, H. S. Hou, B. K. Wu, L. Zhou, S. J. Li, T. J. Wu, J. G. Hu, L. Q. Mai, X. B. Ji, *Nano Energy* **2018**, 48, 617-629.

[5] Y. L. Pan, X. D. Cheng, L. L. Gong, L. Shi, T. Zhou, Y. R. Deng, H. P. Zhang, *ACS Appl. Mater. Interfaces* **2018**, 10, 31441-31451.

[6] Y. Ma, Y. J. Ma, D. Bresser, Y. C. Ji, D. Geiger, U. Kaiser, C. Streb, A. Varzi, S. Passerini, *ACS Nano* **2018**, 12, 7220-7231.

[7] Z. L. Chen, R. B. Wu, M. Liu, H. Wang, H. B. Xu, Y. H. Guo, Y. Song, F. Fang, X. B. Yu, D. L. Sun, *Adv. Funct. Mater.* **2017**, 27, 1702046.

[8] W. T. Zheng, P. Lei, D. X. Luo, Y. X. Huang, G. R. Tian, X. D. Xiang, *Solid State Ion.* **2020**, 345, 115194.

[9] P. Lei, K. Liu, X. Wan, D. X. Luo, X. D. Xiang, *Chem. Commun.* **2019**, 55, 509-512.

[10] X. Wan, D. X. Luo, P. Lei, Y. X. Huang, X. D. Xiang, M. L. Sun, *Inorg. Chem. Front.* **2019**, 6, 598-603.

[11] F. Han, C. Z. Zhang, B. Sun, W. Tang, J. X. Yang, X. K. Li, *Carbon* **2017**, 118, 731-742.

[12] Q. B. Guo, Y. F. Ma, T. T. Chen, Q. Y. Xia, M. Yang, H. Xia, Y. Yu, *ACS Nano* **2017**, 11, 12658-12667.

[13] S. J. Peng, X. P. Han, L. L. Li, Z. Q. Zhu, F. Y. Cheng, M. Srinivansan, S. Adams, S. Ramakrishna, *Small* **2016**, 12, 1359-1368.

[14] C. Wu, Y. Jiang, P. Kopold, P. A. van Aken, J. Maier, Y. Yu, *Adv. Mater.* **2016**, 28,

7276-7283.

[15] J. S. Cho, J. M. Won, J. K. Lee, Y. C. Kang, *Nano Energy* **2016**, 26, 466-478.

[16] Y. N. Ko, Y. C. Kang, *Carbon* **2015**, 94, 85-90.

[17] Z. Hu, Q. N. Liu, S. L. Chou, S. X. Dou, *Adv. Mater.* **2017**, 29, 1700606.

[18] X. Ou, L. Cao, X. H. Liang, F. H. Zheng, H. S. Zheng, X. F. Yang, J. H. Wang, C. H. Yang, M. L. Liu, *ACS Nano* **2019**, 13, 3666-3676.

[19] X. Zhao, Y. Ding, Q. Xu, X. Yu, Y. Liu, H. Shen, *Adv. Energy Mater.* **2019**, 9, 1803648.

[20] H. Yang, R. Xu, Y. Yu, *Energy Storage Mater.* **2019**, 22, 105-112.

[21] B. A. Zhang, G. Rousse, D. Foix, R. Dugas, D. A. D. Corte, J. M. Tarascon, *Adv. Mater.* **2016**, 28, 9824-9830.

[22] C. C. Wang, L. B. Wang, F. J. Li, F. Y. Cheng, J. Chen, *Adv. Mater.* **2017**, 29, 1702212.

[23] T. T. Chen, Y. F. Ma, Q. B. Guo, M. Yang, H. Xia, *J. Mater. Chem. A* **2017**, 5, 3179-3185.

[24] F. Han, C. Y. J. Tan, Z. Q. Gao, *J. Power Sources* **2017**, 339, 41-50.

[25] J. Zhang, D. W. Wang, W. Lv, L. Qin, S. Z. Niu, S. W. Zhang, T. F. Cao, F. Y. Kang, Q. H. Yang, *Adv. Energy Mater.* **2018**, 8, 1801361.

[26] M. Goktas, C. Bolli, E. J. Berg, P. Novak, K. Pollok, F. Langenhorst, M. V. Roeder, O. Lenchuk, D. Mollenhauer, P. Adelhelm, *Adv. Energy Mater.* **2018**, 8, 1702724.

[27] A. P. Cohn, K. Share, R. Carter, L. Oakes, C. L. Pint, *Nano Lett.* **2016**, 16, 543-548.

[28] B. Jache, P. Adelhelm, *Angew. Chem.-Int. Edit.* **2014**, 53, 10169-10173.

[29] A. Ponrouch, D. Monti, A. Boschin, B. Steen, P. Johansson, M. R. Palacin, *J. Mater. Chem. A* **2015**, 3, 22-42.

[30] A. Ponrouch, E. Marchante, M. Courty, J. M. Tarascon, M. R. Palacin, *Energy Environ. Sci.* **2012**, 5, 8572-8583.

[31] P. Peljo, H. H. Girault, *Energy Environ. Sci.* **2018**, 11, 2306-2309.

[32] J. B. Goodenough, Y. Kim, *Chem. Mat.* **2010**, 22, 587-603.

[33] X. Q. Chang, Y. F. Ma, M. Yang, T. Xing, L. Y. Tang, T. T. Chen, Q. B. Guo, X. H. Zhu, J. Z. Liu, H. Xia, *Energy Storage Mater.* **2019**, 23, 358-366.

[34] H. Park, J. Kwon, H. Choi, D. Shin, T. Song, X. W. D. Lou, *ACS Nano* **2018**, 12,

2827-2837.

[35] Y. Y. He, L. Wang, C. F. Dong, C. C. Li, X. Y. Ding, Y. T. Qian, L. Q. Xu, *Energy Storage Mater.* **2019**, 23, 35-45.

[36] G. J. Zhang, K. H. Liu, S. T. Liu, H. H. Song, J. S. Zhou, *J. Alloy. Compd.* **2018**, 731, 714-722.

[37] J. Zhang, D. W. Wang, W. Lv, S. W. Zhang, Q. H. Liang, D. Q. Zheng, F. Y. Kang, Q. H. Yang, *Energy Environ. Sci.* **2017**, 10, 370-376.

[38] Y. Xu, M. Zhou, Y. Lei, *Adv. Energy Mater.* **2016**, 6, 1502514.

[39] D. L. Chao, C. R. Zhu, P. H. Yang, X. H. Xia, J. L. Liu, J. Wang, X. F. Fan, S. V. Savilov, J. Y. Lin, H. J. Fan, Z. X. Shen, *Nat. Commun.* **2016**, 7, 12122.

[40] K. K. Li, J. Zhang, D. M. Lin, D. W. Wang, B. H. Li, W. Lv, S. Sun, Y. B. He, F. Y. Kang, Q. H. Yang, L. M. Zhou, T. Y. Zhang, *Nat. Commun.* **2019**, 10, 725.

Chapter 6

Cobalt Sulfide Nanoparticles Embedded in Arrays of Carbon Nanosheets for Na-Ion Batteries with Enhanced Cycling Stability

Transition metal sulfides have attracted tremendous attention as anodes for sodium-ion batteries because of their large theoretical specific capacity. However, transition metal sulfides usually suffer from poor electrical conductivity and large volume variations during the conversion reactions, restricting the achievement of high capacity and stable cycling. Herein, by integrating the structural advantages of both metal organic frameworks (MOFs) and self-supported graphite foam (GF), carbon nanosheet arrays embedding Co_9S_8 *nanoparticles are anchored on GF substrate, which is prepared by carbonization and sulfurization of the precursor of Co-MOFs nanosheets grown on GF. The self-supported Na-ion anode exhibits a high reversible capacity of 401 mAh* g^{-1} *at 0.5 A* g^{-1} *and a large capacity retention of 85.4% over 300 cycles. Interestingly, the superior Na-storage performance benefits from the optimization of both the thickness and degree of graphitization of carbon nanosheets tuned by the pyrolysis temperature.*

6.1 Introduction

A wide variety of potential Na-storage anode materials have been investigated,[1] mainly including hard carbon,[2, 3] titanium oxides,[4] alloying-type materials from group 14 or group 15,[5, 6] and transition metal sulfides. As typical transition metal sulfides, cobalt sulfides (Co_9S_8, CoS, Co_3S_4 and CoS_2) show large theoretical specific capacity originating from the conversion reaction mechanism and have attracted tremendous attention.[7, 8] In particular, the sulfur-poor Co_9S_8 phase, as the thermodynamically stable phase, also exhibits highly reversible conversion reactions.[9, 10] However, cobalt sulfides usually suffer from poor electrical conductivity and large volume variations during the conversion reaction due to larger Na ions (radius of 1.02 Å) than Li ions (radius of 0.76 Å), restricting the achievement of high capacity and stable cycling.

To move further toward practical applications of cobalt sulfides studied in chapter 5, chapter 6 aims to design Na-storage cobalt sulfides with enhanced cycling stability, a high reversible capacity, and a high ICE. One effective strategy to overcome the above issues is to confine nanoscale cobalt sulfides into a carbon matrix.[9, 11, 12] The introduction of nanostructure design into cobalt sulfide can not only shorten the diffusion distance of Na ions to enlarge the capacity, but also effectively tolerate the strains from large volume changes to enhance cycling stability. More importantly, adopting a carbon matrix to encapsulate these nanostructured cobalt sulfides can further increase the conductivity and withstand the mechanical stress from conversion reactions to enhance the capacity and cycling performance. Commonly, external organic precursors (such as glucose and polydopamine) are employed to cover the surface of active materials and then carbonized to form carbon coatings. Nevertheless, external organic precursors usually could not ensure uniform coating and strong coupling of carbon with cobalt sulfides. In this regard, cobalt-based metal organic frameworks (Co-MOFs) are an ideal template precursor to construct cobalt sulfide nanoparticles embedded in carbon host, because the uniform distribution of cobalt ions and organic ligands in Co-MOFs could result in cobalt sulfide nanoparticles completely confined into the carbon matrix with strong combination after the processes of carbonization and sulfurization.[13-15] On the other hand, constructing nanoarrays of active materials (such as SnS,[16] VO_2,[17] and SnO[18]) on three-dimensional interpenetrating network of graphite foam (GF)[19, 20] has been demonstrated as an effective electrode configuration for SIBs to enhance electrical conductivity and endure mechanical stress through structural integrity, high conductivity and excellent flexibility of self-supported GF.

To integrate the advantages of Co-MOFs and self-supported GF, we designed carbon nanosheet arrays embedding Co_9S_8 nanoparticles anchored on GF substrate (denoted as Co_9S_8-C NS@GF), which was prepared by carbonization and sulfurization of the precursor of Co-MOFs nanosheets grown on GF (Co-MOFs NS@GF). The confinement of Co_9S_8 nanoparticles within carbon nanosheet combined with the excellent conductivity and flexibility of GF network could not only effectively alleviate the mechanical stress from conversion reactions to boost cycling stability, but also ensure fast transport of electrons and Na ions to achieve a high reversible capacity. As a self-supported anode for SIBs, the Co_9S_8-C NS@GF exhibited a high reversible capacity of 401 mAh g^{-1} at 0.5 A g^{-1} and a large capacity retention of 85.4% over 300 cycles. Interestingly, the superior Na-storage performance also benefited from the optimization of both the thickness and degree of graphitization of carbon nanosheets tuned by the pyrolysis temperature.

6.2 Results and Discussion

As shown in scanning electron microscopy (SEM) image in Figure 6.1a, nanosheet-like Co-MOFs arrays with a thickness of ~180 nm were uniformly grown on the highly conductive, flexible and lightweight GF network (prepared by the method of chemical vapor deposition) via a simple room-temperature solution route[21] using cobalt nitrate hexahydrate [$Co(NO_3)_2 \cdot 6H_2O$] and 2-methylimidazole [$C_4H_6N_2$], marked as Co-MOFs NS@GF.

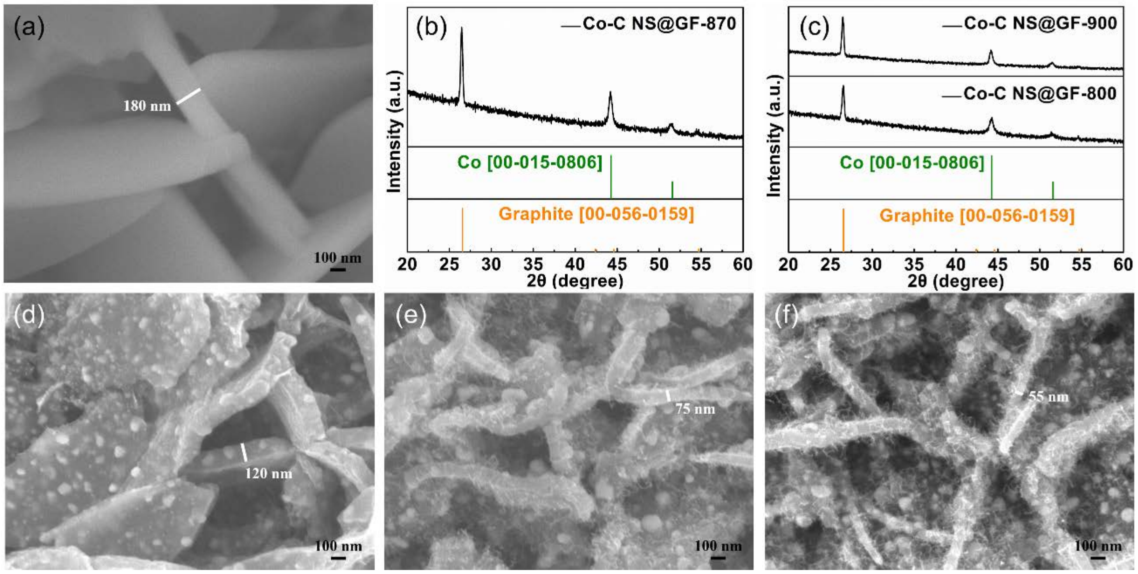

Figure 6.1 (a) SEM image of Co-MOFs NS@GF. (b, c) XRD patterns of Co-C NS@GF carbonized at 870 °C, 800 °C and 900 °C. (d-f) SEM images of Co-C NS@GF carbonized at 800 °C, 870 °C and 900 °C.

The Co-MOFs NS@GF was then pyrolyzed under inert atmosphere of Ar/H_2 (97:3), during which Co ions were reduced and aggregated into Co nanoparticles, and organic ligands (2-methylimidazole) were transformed into carbon. The phase structures of carbonized products (Co-C NS@GF) at 800 °C, 870 °C, and 900 °C were confirmed by the X-ray diffraction (XRD) shown in Figure 6.1b, c. Besides the diffraction peaks of GF substrate, the other peaks could be indexed to the metallic Co phase (ICDD card no. 00-015-0806), verifying that Co-MOFs were completely converted into Co metal after annealing. The morphologies of Co-C NS@GF annealed at 800 °C, 870 °C, and 900 °C were displayed in Figure 6.1d-f, respectively. The nanosheet structure was well maintained after pyrolysis and Co nanoparticles were uniformly distributed and completely confined into the carbon nanosheet, which benefited from the unique structure of Co-MOFs with uniform distribution of cobalt ions and organic ligands. In addition, the thickness of carbon nanosheets decreased from ~120 nm to ~75 nm to ~55 nm with carbonization temperature increasing from 800 to 900 °C. Moreover, catalyzed by the Co nanoparticles and promoted by higher temperature starting from 870 °C, carbon nanotubes grew from the surface of carbon nanosheets,[14] suggesting enhanced degree of graphitization of carbon nanosheets with increase of carbonation temperature.

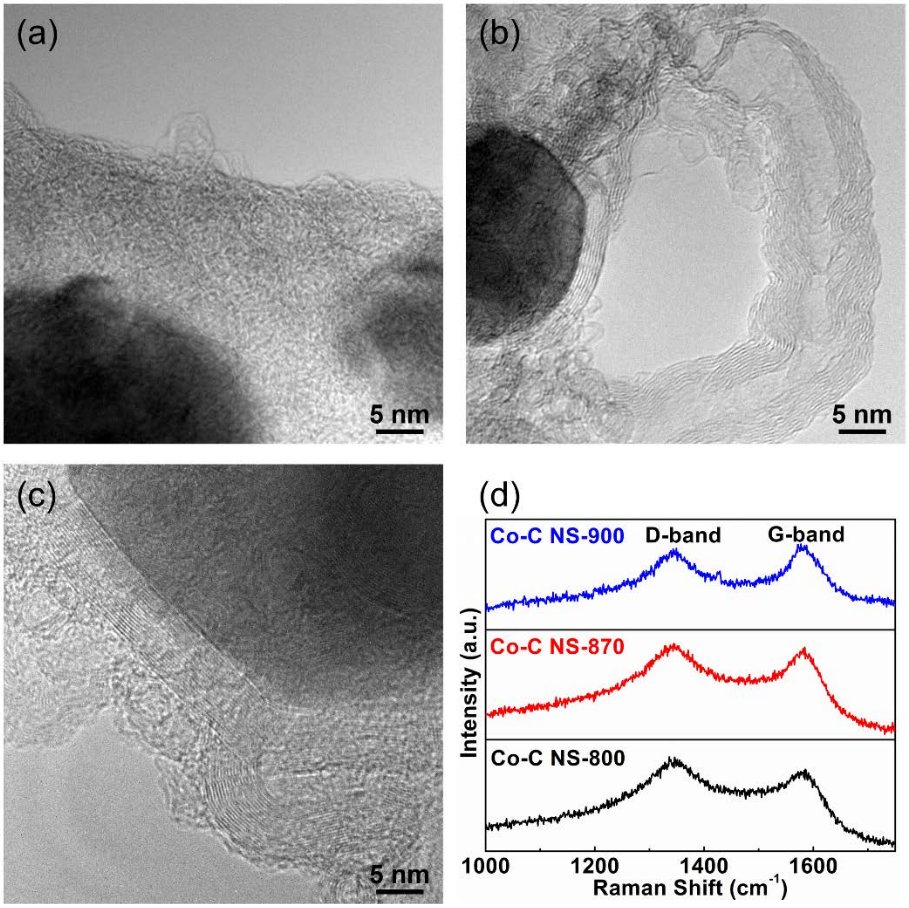

Figure 6.2 (a-c) HRTEM images of Co-C NS@GF carbonized at 800 °C, 870 °C and 900 °C. (d) Raman spectra of Co-C NS-800, 870 and 900.

The microstructures of carbon nanosheets in Co-C NS@GF annealed from 800 to 900 °C were further investigated by high-resolution transmission electron microscopy (HRTEM). The carbon nanosheets prepared at 800 °C owned amorphous structure, shown by the HRTEM image in Figure 6.2a. When the annealing temperature increased to 870 °C, the carbon nanosheets wrapping the Co nanoparticles became crystalline, accompanied with the formation of carbon nanotubes (Figure 6.2b). The degree of graphitization was further enhanced at 900 °C with smaller d_{002} spacing of carbon nanosheets than that at 870 °C, shown in Figure 6.2c. The variation of graphitization extent with temperature was also examined by Raman spectra in Figure 6.2d. The D-band peak at ~1355 cm^{-1} corresponds to the disorder structure of carbon, while the G-band peak at ~1590 cm^{-1} originates from the typical sp^2 C-C bonds in the graphitic structure.[22, 23] With increased annealing temperature from 800 to 900 °C, the G-band peak was gradually intensified compared to the intensity of D-band, further demonstrating the enhancement of crystallinity of carbon nanosheets.

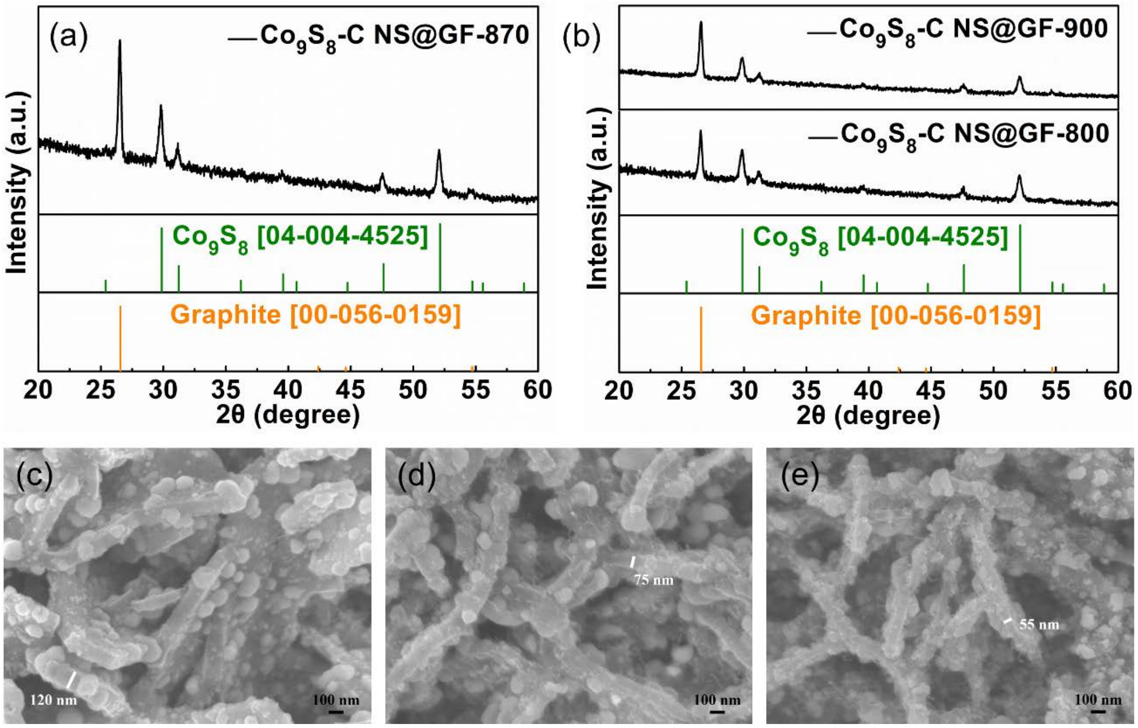

Figure 6.3 (a, b) XRD patterns of Co_9S_8-C NS@GF-870, 800, 900. (c-e) SEM images of Co_9S_8-C NS@GF-800, 870, 900.

The Co-C NS@GF obtained at 800 °C, 870 °C, and 900 °C were finally transformed to the corresponding Co_9S_8-C NS@GF-800, 870 and 900 through the sulfurization of sulfur powder at 650 °C in the tube furnace. The XRD patterns of Co_9S_8-C NS@GF-870, 800, 900 in Figure 6.3a, b confirmed the complete transformation from Co to Co_9S_8 by only detecting pure Co_9S_8 phase (ICDD card no. 04-004-4525) except for the diffraction peaks belonging to the substrate of GF. After sulfurization, the Co_9S_8 nanoparticles were still embedded into the carbon nanosheets, but became larger than the former Co nanoparticles, as shown in Figure 6.3c-e. As for the carbon nanosheets, the thickness kept unchanged after the process of sulfurization.

CR2032 half coin cells were assembled to explore the electrochemical properties of Co_9S_8-C NS@GF-870, 800 and 900 for SIBs using the self-supported Co_9S_8-C NS@GF as working electrodes, Na foils as counter and reference electrodes, and ether-based electrolyte[24] of 1 M $NaCF_3SO_3$ in diglyme. Galvanostatic charge-discharge of Co_9S_8-C NS@GF-870, 800 and 900 was measured at 0.5 A g^{-1} within a potential range of 0.3-2.9 V with the corresponding profiles for the initial three cycles shown in Figure 6.4a-c. The three Co_9S_8-C NS@GF anodes exhibited similar charge-discharge curves, in which the conversion reaction from Co_9S_8 to Co and Na_2S is correlated to the long discharge plateau at ~0.9 V and the reversed reaction occurs at ~1.7 V (the long charge plateau).[9] In addition, the co-intercalation/deintercalation of Na ions solvated by diglyme between the interlayers of the GF substrate correspond to the short discharge/charge plateaus at about 0.6 and 0.7 V, respectively.[25, 26] Among the three electrodes, Co_9S_8-C NS@GF-870 delivered the largest capacity with the initial discharge and charge specific capacities of 429.7 and 400.4 mAh g^{-1} (Figure 6.4a), also resulting in a high initial Coulombic efficiency (ICE) of 93.2%. The larger capacity of Co_9S_8-C NS@GF-870 could be attributed to faster Na^+ and electronic transfer, which resulted from higher graphitization degree of carbon nanosheets at 870 ℃ than that in Co_9S_8-C NS@GF-800, and larger contact areas between Co nanoparticles and carbon nanosheets benefiting from thicker carbon nanosheets (~75 nm) at 870 ℃ than that (~55 nm) in Co_9S_8-C NS@GF-900. In addition, the interconnected network structure and high electrical conductivity of the GF substrate also contribute to the large capacity of Co_9S_8-C NS@GF-870.

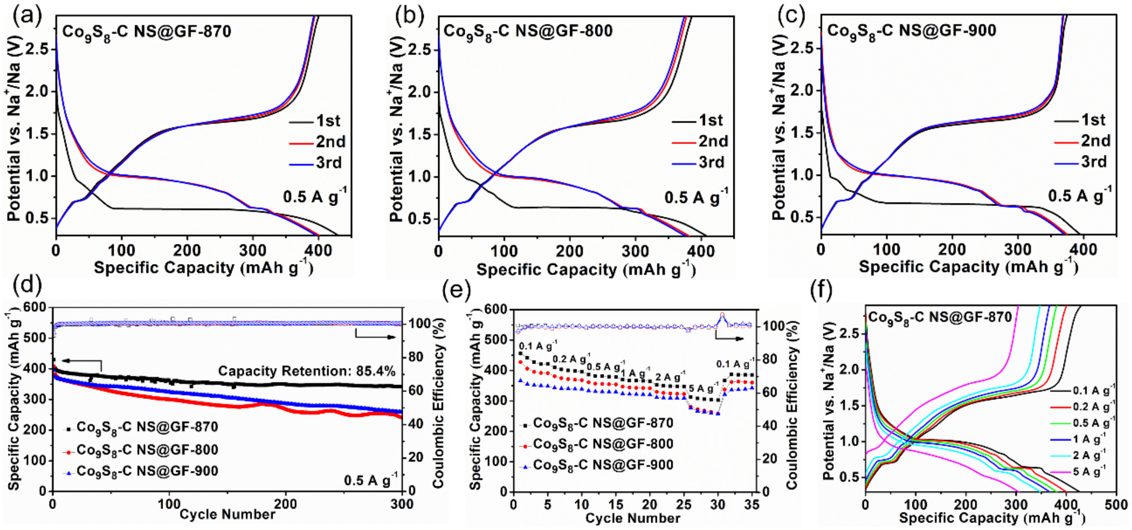

Figure 6.4 (a-c) Charge-discharge profiles and (d) cycling performance of Co_9S_8-C NS@GF-870, 800 and 900 at 0.5 A g^{-1}. (e) Rate capabilities of the three Co_9S_8-C NS@GF at different current densities from 0.1 to 5 A g^{-1}. (f) Charge-discharge curves of Co_9S_8-C NS@GF-870 at different current densities.

Figure 6.4d compares the cycling stability of the three Co_9S_8-C NS@GF at 0.5 A g^{-1} between 0.3 and 2.9 V, in which the Co_9S_8-C NS@GF-870 also achieved the best cycling performance with a high capacity retention of 85.4% (342.6 mAh g^{-1}) over 300 cycles, while the capacity retentions of Co_9S_8-C NS@GF-800 and Co_9S_8-C NS@GF-900 were only 62.9% (240.2 mAh g^{-1}) and 69.0% (258.5 mAh g^{-1}), respectively. The achievement of superior cycling performance for Co_9S_8-C NS@GF-870 is an optimization result of both the thickness and graphitization degree of carbon nanosheets. In comparison with Co_9S_8-C NS@GF-800, the higher graphitization degree of carbon nanosheets in Co_9S_8-C NS@GF-870 means not only higher electrical conductivity, but also stronger coupling between the carbon nanosheets and Co_9S_8 nanoparticles, which could effectively avoid the detachment of Co_9S_8 nanoparticles from the carbon matrix during the conversion reactions with severe volume variations. On the other hand, the thicker carbon nanosheets in Co_9S_8-C NS@GF-870 than those in Co_9S_8-C NS@GF-900 could ensure larger embedment areas of Co_9S_8 nanoparticles into carbon nanosheets, therefore fixing these Co_9S_8 nanoparticles more effectively.

The rate capabilities of the three Co_9S_8-C NS@GF were evaluated in Figure 6.4e and the Co_9S_8-C NS@GF-870 anode still exhibited the best rate performance. Specifically, Co_9S_8-C NS@GF-870 delivered the average discharge specific capacities of 427.2, 400.3, 381.0, 366.9, and 348.5 mAh g^{-1} at 0.1, 0.2, 0.5, 1, and 2 A g^{-1}, respectively. Even at 5 A g^{-1}, a large capacity of 305.6 mAh g^{-1} still remained. Such excellent rate performance should originate from high graphitization degree of carbon nanosheets, large embedment extent of Co_9S_8 nanoparticles into the carbon nanosheets, and outstanding electrical conductivity of GF network. In addition, as shown in Figure 6.4f, the polarization increased slowly from 0.1 to 2 A g^{-1}, indicating fast electrode kinetics of Co_9S_8-C NS@GF-870.

The cyclic voltammetry (CV) technique was introduced to study the electrochemical reactions of Co_9S_8-C NS@GF-870 at a scan rate of 0.1 mV s^{-1} (Figure 6.5a).[27] The cathodic peak at 0.93 V is induced by the reduction reaction of Co_9S_8 to Co and Na_2S, while the anodic peak at 1.69 V could be attributed to the reversible formation of Co_9S_8. The two cathodic and anodic peaks correspond to the long discharge and charge plateaus, respectively, shown in Figure 6.4a. In addition, the co-intercalation reactions of the GF substrate happen at 0.82 and 0.62 V, accompanied with the corresponding deintercalation reactions at 0.71 and 0.93 V.

To explore the kinetic behavior of conversion reactions within Co_9S_8-C NS@GF-870, the CV profiles were recorded at different scan rates from 0.1 to 1.0 mV s^{-1} and displayed in Figure 6.5b. The scan rate (v) and the corresponding peak current (i) can be correlated by the linear relationship between lg i and lg v. In the plot of lg i versus lg v, the slope b is an important parameter, judging the kinetic types of electrochemical reactions.[13] In detail, if an electrochemical reaction is dominated by diffusion process, the b value is close to 0.5. If the electrochemical reaction is surface-determined (also called pseudocapacitive behavior), b approximates 1.0. Here, the reduction peak at 0.93 V (Peak I) and the oxidation peak at 1.69 V (Peak II) were selected for kinetic analysis and the corresponding lg i vs. lg v plots are shown in Figure 6.5c. The fitted b values for Peak I and Peak II are 0.62 and 0.78, respectively, both between 0.5 and 1.0, indicating the co-existence of diffusion-controlled and pseudocapacitive-controlled processes in the conversion reactions of Co_9S_8-C NS@GF-870.

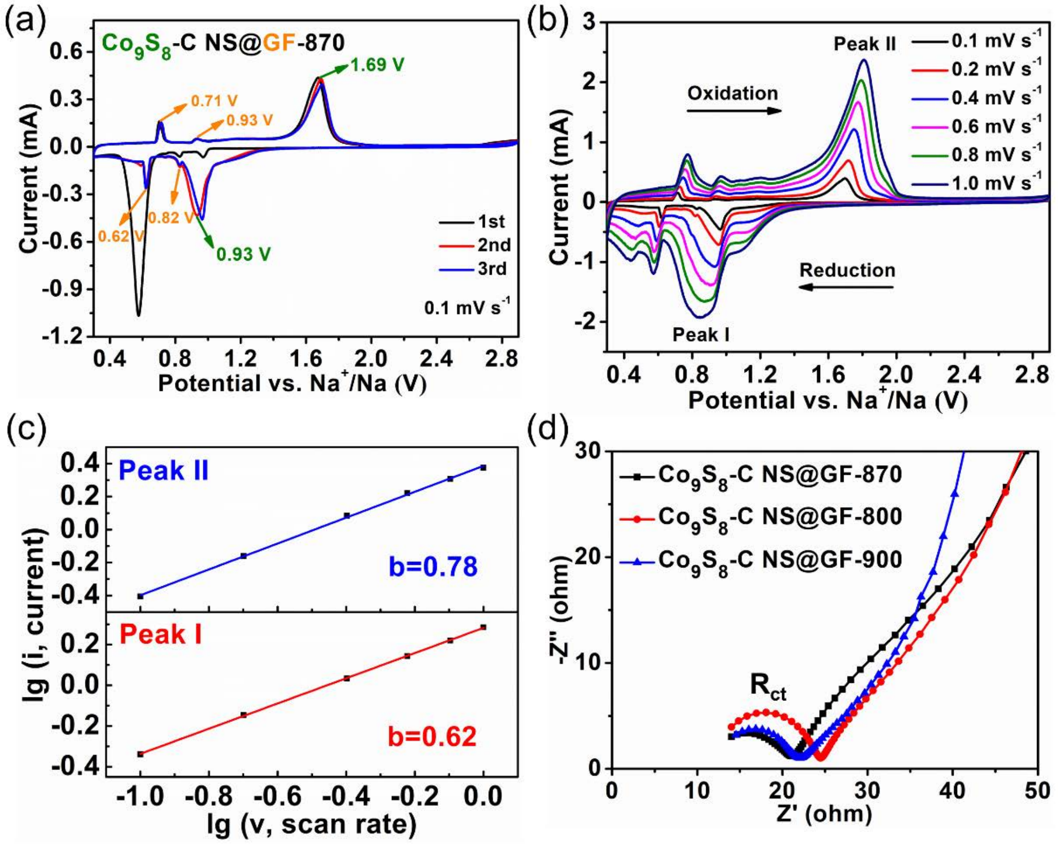

Figure 6.5 CV curves of Co_9S_8-C NS@GF-870 (a) at a scan rate of 0.1 mV s^{-1} and (b) at different scan rates from 0.1 to 1.0 mV s^{-1}. (c) Plots of lg *i* versus lg *v* for the states of reduction (Peak I) and oxidation (Peak II). (d) Nyquist plots of the three Co_9S_8-C NS@GF electrodes at fully charged state for the 50th cycle.

The electrochemical impedance spectroscopy (EIS) was performed to measure the charge-transfer resistance (R_{ct}) of the three Co_9S_8-C NS@GF at the 50th cycle in Figure 6.5d. The value of R_{ct} can be identified as the diameter of the semicircle in high-frequency region of Nyquist plot.[27] The R_{ct} values of Co_9S_8-C NS@GF-870 and 900 are obviously smaller than that of Co_9S_8-C NS@GF-800, which could be attributed to the enhanced electrical conductivity of carbon nanosheets benefiting from the high degree of graphitization at 870 and 900 ℃.

6.3 Conclusion

By taking the structural advantages of both Co-MOFs and self-supported GF, Co-MOFs nanosheets were first grown on the GF substrate. After the processes of carbonization and sulfurization, carbon nanosheet arrays embedding Co_9S_8 nanoparticles were anchored on GF substrate (Co_9S_8-C NS@GF). The confinement of Co_9S_8 nanoparticles within carbon nanosheet combined with the excellent conductivity and flexibility of GF network could not only effectively alleviate the mechanical stress from conversion reactions to boost cycling stability, but also ensure fast transport of electrons and Na ions to achieve a high reversible capacity. As a self-supported anode for SIBs, the Co_9S_8-C NS@GF exhibited a high reversible capacity of 401 mAh g^{-1} at 0.5 A g^{-1} and a large capacity retention of 85.4% over 300 cycles. Interestingly, the superior Na-storage performance also benefited from the optimization of both the thickness and degree of graphitization of carbon nanosheets tuned by the pyrolysis temperature.

References

[1] J. Y. Hwang, S. T. Myung, Y. K. Sun, *Chem. Soc. Rev.* **2017**, 46, 3529-3614.

[2] D. Saurel, B. Orayech, B. W. Xiao, D. Carriazo, X. L. Li, T. Rojo, *Adv. Energy Mater.* **2018**, 8, 1703268.

[3] N. Sun, Z. R. X. Guan, Y. W. Liu, Y. L. Cao, Q. Z. Zhu, H. Liu, Z. X. Wang, P. Zhang, B. Xu, *Adv. Energy Mater.* **2019**, 9, 1901351.

[4] K. K. Li, J. Zhang, D. M. Lin, D. W. Wang, B. H. Li, W. Lv, S. Sun, Y. B. He, F. Y. Kang, Q. H. Yang, L. M. Zhou, T. Y. Zhang, *Nat. Commun.* **2019**, 10, 725.

[5] H. Gao, T. F. Zhou, Y. Zheng, Y. Q. Liu, J. Chen, H. K. Liu, Z. P. Guo, *Adv. Energy Mater.* **2016**, 6, 1601037.

[6] Q. Li, Z. Q. Li, Z. W. Zhang, C. X. Li, J. Y. Ma, C. X. Wang, X. L. Ge, S. H. Dong, L. W. Yin, *Adv. Energy Mater.* **2016**, 6, 1600376.

[7] S. J. Peng, X. P. Han, L. L. Li, Z. Q. Zhu, F. Y. Cheng, M. Srinivansan, S. Adams, S. Ramakrishna, *Small* **2016**, 12, 1359-1368.

[8] Y. C. Du, X. S. Zhu, X. S. Zhou, L. Y. Hu, Z. H. Dai, J. C. Bao, *J. Mater. Chem. A* **2015**, 3, 6787-6791.

[9] Q. B. Guo, Y. F. Ma, T. T. Chen, Q. Y. Xia, M. Yang, H. Xia, Y. Yu, *ACS Nano* **2017**, 11, 12658-12667.

[10] Y. Y. Zhao, Q. Pang, Y. J. Wei, L. Y. Wei, Y. M. Ju, B. Zou, Y. Gao, G. Chen, *ChemSusChem* **2017**, 10, 4778-4785.

[11] C. Wu, Y. Jiang, P. Kopold, P. A. van Aken, J. Maier, Y. Yu, *Adv. Mater.* **2016**, 28, 7276-7283.

[12] T. T. Chen, Y. F. Ma, Q. B. Guo, M. Yang, H. Xia, *J. Mater. Chem. A* **2017**, 5, 3179-3185.

[13] Z. L. Chen, R. B. Wu, M. Liu, H. Wang, H. B. Xu, Y. H. Guo, Y. Song, F. Fang, X. B. Yu, D. L. Sun, *Adv. Funct. Mater.* **2017**, 27, 1702046.

[14] Y. Ma, Y. J. Ma, D. Bresser, Y. C. Ji, D. Geiger, U. Kaiser, C. Streb, A. Varzi, S. Passerini, *ACS Nano* **2018**, 12, 7220-7231.

[15] Y. F. Dong, W. Shi, P. F. Lu, J. Q. Qin, S. H. Zheng, B. S. Zhang, X. H. Bao, Z. S. Wu, *J. Mater. Chem. A* **2018**, 6, 14324-14329.

[16] D. L. Chao, C. R. Zhu, P. H. Yang, X. H. Xia, J. L. Liu, J. Wang, X. F. Fan, S. V. Savilov, J. Y. Lin, H. J. Fan, Z. X. Shen, *Nat. Commun.* **2016**, 7, 12122.

[17] D. L. Chao, C. R. Zhu, X. H. Xia, J. L. Liu, X. Zhang, J. Wang, P. Liang, J. Y. Lin, H. Zhang, Z. X. Shen, H. J. Fan, *Nano Lett.* **2015**, 15, 565-573.

[18] M. H. Chen, D. L. Chao, J. L. Liu, J. X. Yan, B. W. Zhang, Y. Z. Huang, J. Y. Lin, Z. X. Shen, *Adv. Funct. Mater.* **2017**, 27, 1606232.

[19] Z. P. Chen, W. C. Ren, L. B. Gao, B. L. Liu, S. F. Pei, H. M. Cheng, *Nat. Mater.* **2011**, 10, 424-428.

[20] J. L. Liu, L. L. Zhang, H. B. Wu, J. Y. Lin, Z. X. Shen, X. W. Lou, *Energy Environ. Sci.* **2014**, 7, 3709-3719.

[21] C. Guan, A. Sumboja, H. J. Wu, W. N. Ren, X. M. Liu, H. Zhang, Z. L. Liu, C. W. Cheng, S. J. Pennycook, J. Wang, *Adv. Mater.* **2017**, 29, 1704117.

[22] W. Xiao, Q. Sun, J. Liu, B. W. Xiao, Y. L. Liu, P. A. Glans, J. Li, R. Y. Li, X. F. Li, J. H. Guo, W. L. Yang, T. K. Sham, X. L. Sun, *Nano Energy* **2019**, 66, 104177.

[23] D. S. Bin, X. J. Lin, Y. G. Sun, Y. S. Xu, K. Zhang, A. M. Cao, L. J. Wan, *J. Am.*

Chem. Soc. **2018**, 140, 7127-7134.

[24] J. Zhang, D. W. Wang, W. Lv, L. Qin, S. Z. Niu, S. W. Zhang, T. F. Cao, F. Y. Kang, Q. H. Yang, *Adv. Energy Mater.* **2018**, 8, 1801361.

[25] B. Jache, P. Adelhelm, *Angew. Chem.-Int. Edit.* **2014**, 53, 10169-10173.

[26] M. Goktas, C. Bolli, E. J. Berg, P. Novak, K. Pollok, F. Langenhorst, M. V. Roeder, O. Lenchuk, D. Mollenhauer, P. Adelhelm, *Adv. Energy Mater.* **2018**, 8, 1702724.

[27] X. M. Yang, A. L. Rogach, *Adv. Energy Mater.* **2019**, 9, 1900747.

Chapter 7

Conclusions and Recommendations

Chapter 7 draws the conclusion of the whole thesis and presents the extent to which the hypothesis was proven. Additionally, some recommended future works are included.

7.1 Conclusions

This thesis aims to develop self-supported anode materials based on hard carbon and cobalt sulfides for sodium-ion batteries (SIBs), which are regarded as promising low-cost alternatives to the prevailing lithium-ion batteries. As hard carbons are considered as the most promising first-generation Na-storage anodes, chapter 4 aims to design Na-storage hard carbon with both long cycling stability and a large reversible capacity. In order to achieve higher energy density and ensure the possibility for assembling full cells, chapter 5 aims to develop Na-storage cobalt sulfides with a high initial Coulombic efficiency (ICE). To move further toward practical applications, chapter 6 aims to design Na-storage cobalt sulfides with enhanced cycling stability, a high reversible capacity, and a high ICE.

In chapter 4, the hollow interconnected carbon foam (HICF) was developed by one-step pyrolysis of a commercial and low-cost melamine sponge. The integration of interconnected network structure and hollow feature (Figure 7.1) can not only enable strong mechanical stability and extra inner space to effectively accommodate the structural deformation from Na^+ insertion/extraction, but also achieve fast sodium-ion and electron transport. As a self-supported anode for SIBs, HICF-1 delivered a large reversible capacity (305.7 mAh g^{-1} at 100 mA g^{-1}) with a high initial Coulombic efficiency of 80.2%, an ultralong cycle life (86.4% capacity retention after 1000 cycles at 1000 mA g^{-1}), as well as superior rate performance (170.1 mAh g^{-1} at 1000 mA g^{-1}). Therefore, the hypothesis for chapter 4 proposed in chapter 1 was fully proven. In addition, the excellent Na-storage performance is also contributed by the maximum content (63.24%) of pseudo-graphitic phase (d_{002}-spacing between 0.36 and 0.40 nm) in HICF-1 realized by tuning pyrolysis holding time, because the pseudo-graphitic phase could store more sodium ions and maintain more stable microstructure owing to its appropriate *d*-spacing than highly disordered phase (d_{002}-spacing above 0.40 nm). Furthermore, kinetic analysis based on cyclic voltammetry (CV) and galvanostatic intermittent titration technique (GITT) verified the adsorption-intercalation mechanism, in which highly disordered carbon phase absorbs Na ions fast in the sloping region and then Na ions intercalate into the pseudo-graphitic phase in the plateau region. This work provides a very promising anode candidate for the future commercialization of low-cost SIBs.

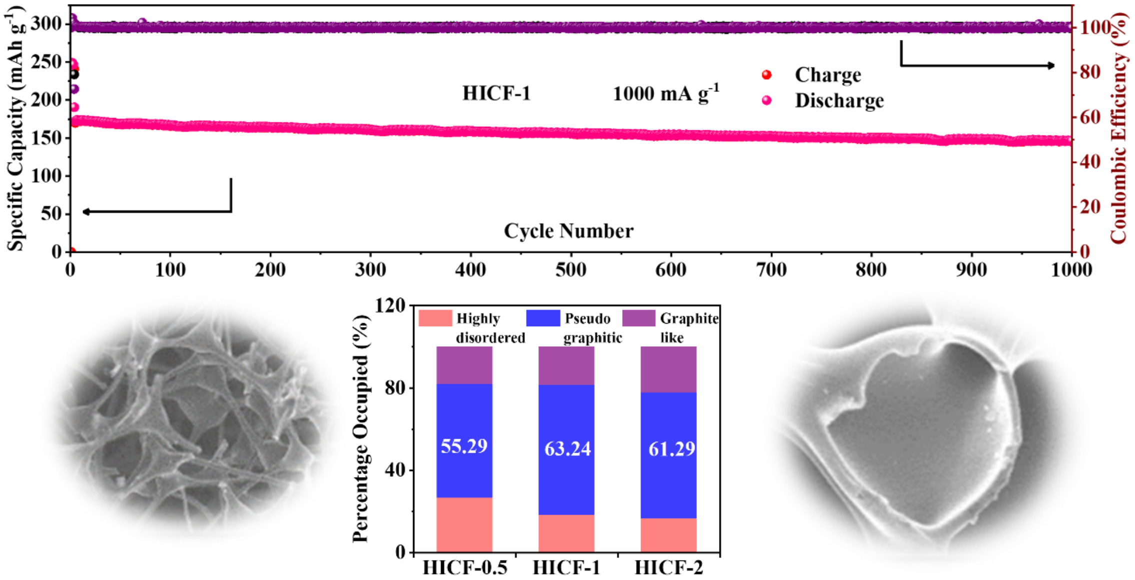

Figure 7.1 Maximized pseudo-graphitic content in self-supported hollow interconnected carbon foam boosting ultrastable Na-ion storage.

In chapter 5, the CoS_x NF@GF composite has been developed by growing CoS_x (Co_9S_8/CoS) nanoflakes on the highly conductive and flexible substrate of graphite foam (GF) through a one-pot solvothermal route. As a freestanding anode for SIBs, to the best of our knowledge, CoS_x NF@GF in diglyme-based electrolyte achieved the highest ICE of 99.4% among the previously reported cobalt sulfide-based Na-ion anodes. Through a systematic investigation of several factors that can potentially influence the ICE, such a high ICE could be ascribed to the following three aspects (Figure 7.2), including i) the negligible side reactions between diglyme-based electrolyte and Co_9S_8/CoS, owing to much higher Fermi level of diglyme reduction than anode potential μ_A of Co_9S_8/CoS, blocking transfer of electrons from anode to electrolyte, ii) the highly reversible conversion reaction of Co_9S_8/CoS, and iii) the rather low initial capacity loss of substrate GF. Therefore, the hypothesis for chapter 5 proposed in chapter 1 was fully proven. Furthermore, CoS_x NF@GF in diglyme-based electrolyte achieved excellent cycling and rate performance, primarily resulting from alleviated volume expansion and facilitated ionic and electronic kinetics ensured by ultrathin nanoflakes vertically aligned with GF, as well as negligible side reactions at the interface of electrode/electrolyte. These revealed underlying rules can be extended to develop other Na-ion storage anode materials with superb ICE.

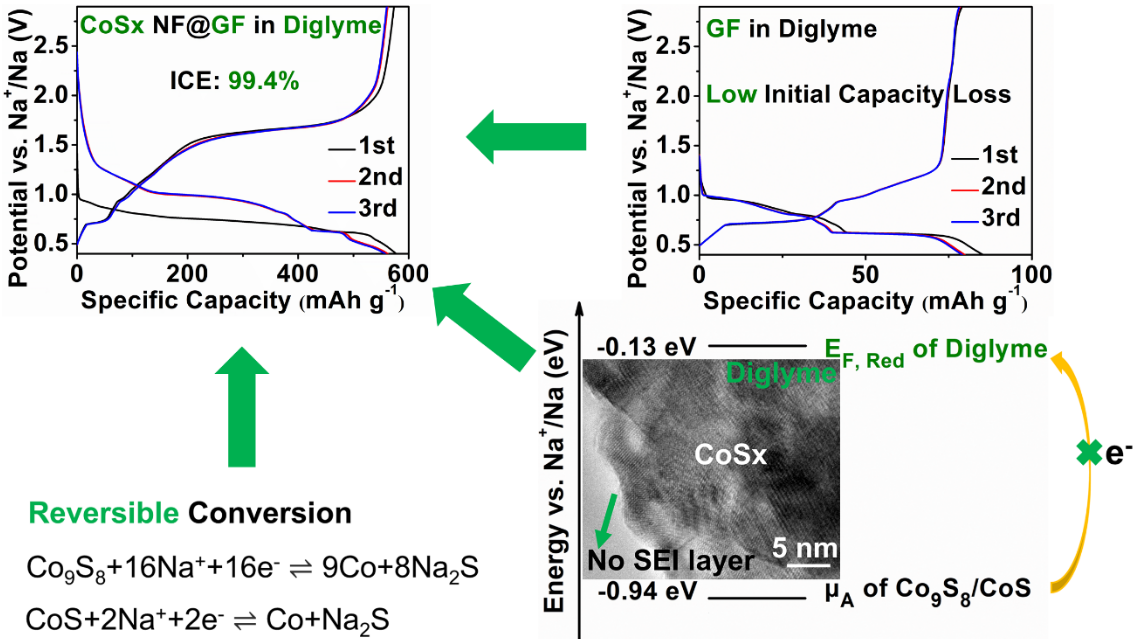

Figure 7.2 Three underlying root causes for ultrahigh ICE of Na-storage cobalt sulfide nanoarrays.

In chapter 6, by taking the structural advantages of both cobalt-based metal organic frameworks (Co-MOFs) and self-supported GF, Co-MOFs nanosheets were first grown on the GF substrate. After the processes of carbonization and sulfurization, carbon nanosheet arrays embedding Co_9S_8 nanoparticles were anchored on GF substrate (Co_9S_8-C NS@GF). The confinement of Co_9S_8 nanoparticles within carbon nanosheet combined with the excellent conductivity and flexibility of GF network could not only effectively alleviate the mechanical stress from conversion reactions to boost cycling stability, but also ensure fast transport of electrons and Na ions to achieve a high reversible capacity. As a self-supported anode for SIBs, the Co_9S_8-C NS@GF exhibited a high reversible capacity of 401 mAh g^{-1} at 0.5 A g^{-1} with a high ICE of 93.2% and a large capacity retention of 85.4% over 300 cycles. Therefore, the hypothesis for chapter 6 proposed in chapter 1 was fully proven. Interestingly, the superior Na-storage performance also benefited from the optimization of both the thickness and degree of graphitization of carbon nanosheets tuned by the pyrolysis temperature.

7.2 Future Work

7.2.1 Effect of Crystal Phases of Cobalt Sulfides on Na and K Storage

In the work of chapter 5, the CoS_x NF@GF composite was composed of mixed phase of cubic Co_9S_8 and hexagonal CoS. The crystal structures of Co_9S_8 and CoS are illustrated in Figure 7.3. The atomic ratio of Co/S for the two phases is very similar and they also have approximate theoretical specific capacities: 545 mAh g^{-1} for Co_9S_8 and 589 mAh g^{-1} for CoS. However, how will the phase differences of cubic Co_9S_8 and hexagonal CoS affect Na-storage performance? Until now, no research has been focused on this interesting point.

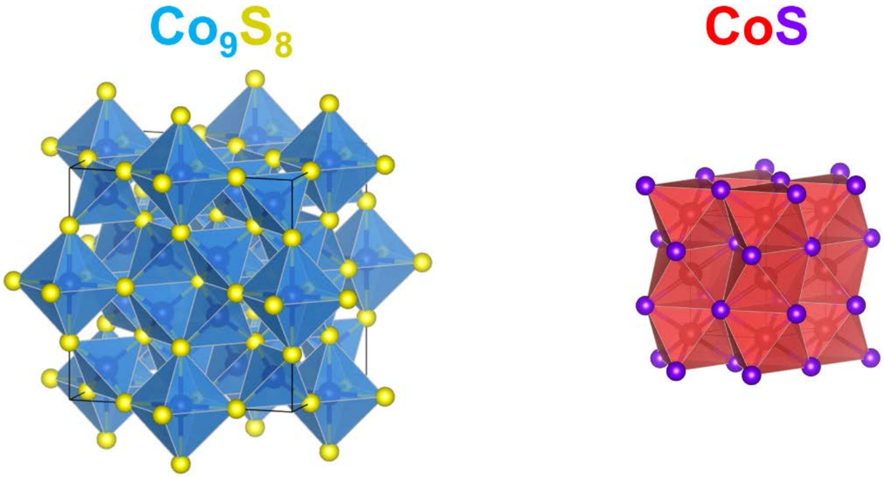

Figure 7.3 Schematic illustration for crystal structures of Co_9S_8 and CoS.

The CoS_x NF@GF composite can be transformed into pure Co_9S_8 phase (Co_9S_8 NF@GF) through a reduction reaction, while pure CoS phase (CoS NF@GF) can be obtained by further sulfurizing the CoS_x NF@GF. As originating from the same source of CoS_x NF@GF, both Co_9S_8 NF@GF and CoS NF@GF will maintain the morphology of nanoflakes to eliminate the impact of morphology on Na-storage performance. After preparation, the electrochemical properties of the above samples as anodes for SIBs will be elaborately investigated and compared to uncover how the crystal phases of cobalt sulfides affect Na-storage properties.

Additionally, potassium-ion batteries (PIBs) have emerged in recent years as a low-cost energy-storage technique, which starts to compete with SIBs.[1-3] As K ions have a larger size than Na ions, it is expected that the K-storage performance of anode materials will be poorer, compared with their Na-storage performance. Indeed, many anode materials exhibited poorer electrochemical properties for PIBs. However, some appealing results also appeared in PIBs.[4] For example, Gao et al. reported CoS nanoclusters of quantum dots anchored on graphene sheets, which exhibited better rate performance for KIBs than that for SIBs, shown in Figure 7.4.[5] Therefore, it is also worthwhile to explore the K-ion storage performance of Co_9S_8 NF@GF and CoS NF@GF.

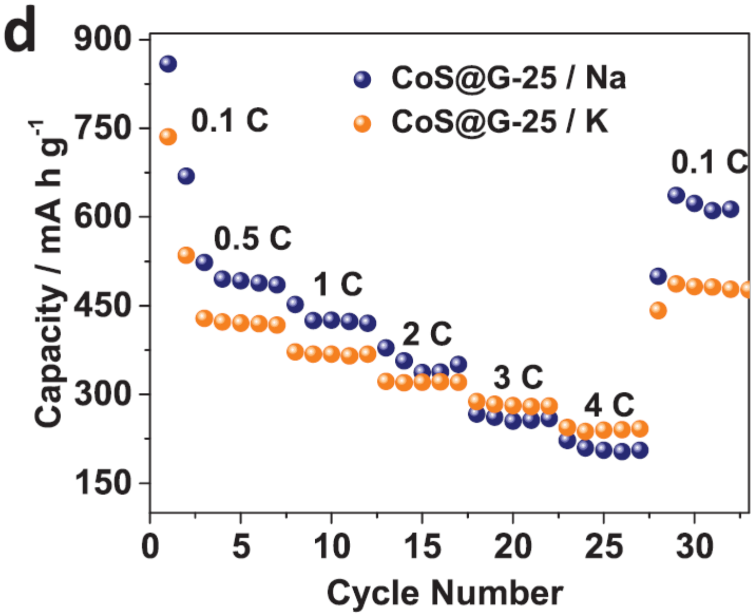

Figure 7.4 Rate capability of CoS@G-25 in KIBs versus that in SIBs.[5]

7.2.2 Hollow Co_3O_4 for Na-Ion Storage

Compared with Co_9S_8 and CoS, cobalt oxides Co_3O_4 own a larger theoretical specific capacity of 890 mAh g^{-1} and a lower working potential of ~0.5 V (Figure 7.5) for SIBs, which attract more and more research attention.[6] However, Co_3O_4 suffer from more sluggish reaction kinetics than cobalt sulfides, because Na_2O produced in the conversion reactions of Co_3O_4 has stronger Na-O bonds than Na-S bonds in Na_2S formed during the conversion reactions of cobalt sulfides, which means that it is harder to break Na-O bonds in the reverse conversion reactions. Therefore, more elaborate structural design should be proposed to enhance the electrode kinetics of Co_3O_4.

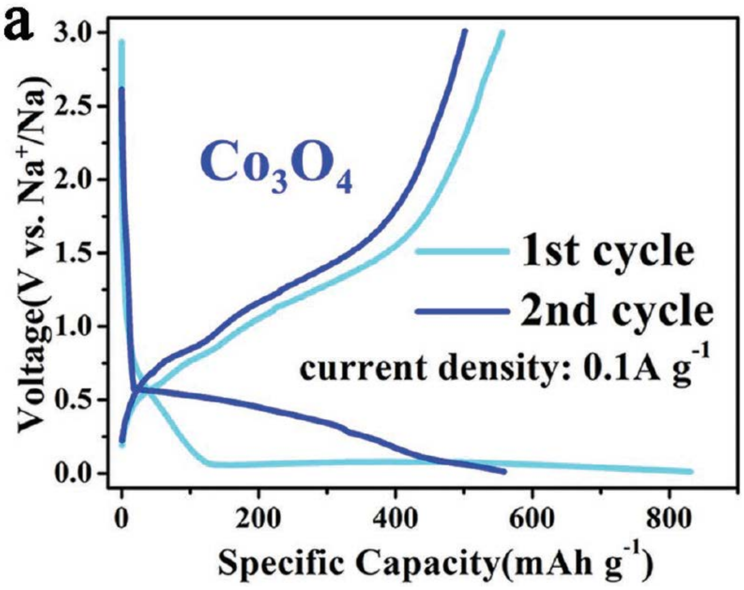

Figure 7.5 Discharge-charge profiles of Co_3O_4 for SIBs.[6]

In the chapter 6, Co-MOFs nanosheets were first grown on the GF substrate. After carbonization, carbon nanosheet arrays embedding Co nanoparticles were anchored on GF substrate. Instead of sulfurization, oxidation of Co nanoparticles at suitable temperature in air can evolve into hollow Co_3O_4 nanoparticles due to the Kirkendall effect, illustrated in Figure 7.6.[7] The hollow structure can further shorten the distance of Na-ion transport, which is very promising to enhance the electrode kinetics of Co_3O_4.

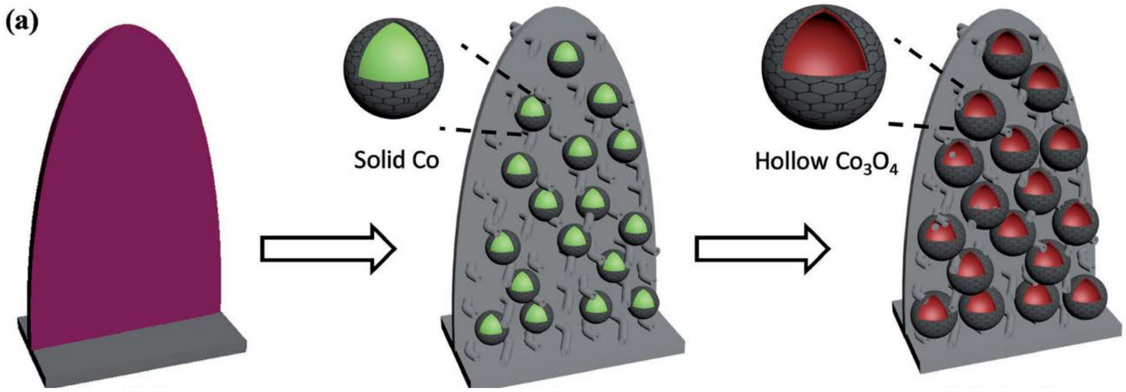

Figure 7.6 Schematic illustration for synthesis of hollow Co_3O_4.[7]

References

[1] J. Y. Hwang, S. T. Myung, Y. K. Sun, *Adv. Funct. Mater.* **2018**, 28, 1802938.

[2] X. Wu, Y. L. Chen, Z. Xing, C. W. K. Lam, S. S. Pang, W. Zhang, Z. C. Ju, *Adv. Energy Mater.* **2019**, 9, 1900343.

[3] Z. H. Wang, S. M. Selbach, T. Grande, *RSC Adv.* **2014**, 4, 4069-4079.

[4] D. S. Bin, X. J. Lin, Y. G. Sun, Y. S. Xu, K. Zhang, A. M. Cao, L. J. Wan, *J. Am. Chem. Soc.* **2018**, 140, 7127-7134.

[5] H. Gao, T. F. Zhou, Y. Zheng, Q. Zhang, Y. Q. Liu, J. Chen, H. K. Liu, Z. P. Guo, *Adv. Funct. Mater.* **2017**, 27, 1702634.

[6] M. Xu, Q. T. Xia, J. L. Yue, X. H. Zhu, Q. B. Guo, J. W. Zhu, H. Xia, *Adv. Funct. Mater.* **2019**, 29, 1807377.

[7] C. Guan, A. Sumboja, H. J. Wu, W. N. Ren, X. M. Liu, H. Zhang, Z. L. Liu, C. W. Cheng, S. J. Pennycook, J. Wang, *Adv. Mater.* **2017**, 29, 1704117.